Ph.D. Thesis, Towards Fully 3-Dimensional Simulations of Heavy Ion Collisions in the IP-Glasma Initial State Framework

Scott McDonald
Supervisor: Sangyong Jeon
Department of Physics
McGill University
Montréal, Québec
Canada
June 2020

A Thesis submitted to McGill University in partial fulfillment
of the requirements for the degree of Doctorate of Philosophy (PhD)

Contents

Figures and Tables

Figures

TABLES

Abstract

Heavy ion collisions conducted at the Relativistic Heavy Ion Collider (RHIC) and the Large Hadron Collider (LHC) are sufficiently energetic to create a deconfined state of quarks and and gluons known as Quark Gluon Plasma (QGP). In the infinite momentum limit, there is a longitudinal symmetry, known as boost invariance, that reduces the dynamics to 2+1-dimensions, simplifying simulations and allowing for detailed study of the transverse dynamics of heavy ion collisions. Boost invariance is only an approximation, however, and a complete understanding must come from the full 3+1D dynamics of heavy ion collisions. In this thesis, the phenomenologically successful IP-Glasma model [1, 2] for the initial state of heavy ion collisions is generalized to 3+1D using JIMWLK rapidity evolution [3, 4] of the pre-collision Wilson lines. The initial gauge fields for the individual nuclei are modified to be pure gauge outside of the source terms in all three spatial directions in order to avoid energy deposition outside of the interaction region between the two nuclei. Additionally, Gauss' law is no longer trivially satisfied in 3+1D, and must be satisfied locally. An ansatz and iterative solution to Gauss' law is introduced. The effect of these modifications is explored on the evolution of the chromo-electric and chromo-magnetic fields, as well as the pressure in the IP-Glasma phase. Most importantly, these modifications allow for self-consistent temporal evolution of the Classical Yang Mills equation of motion on a 3D lattice and thus for phenomenological application. The 3+1D IP-Glasma initial state is coupled to 3+1D relativistic viscous hydrodynamics using the MUSIC numerical software [5], which is in turn matched to the hadronic cascade model UrQMD [6]. This hybrid model is used to study the initialization and evolution of Pb-Pb collisions at $\sqrt{s} = 2.76\,\text{TeV}$ in 3+1D, providing the first opportunity to study the phenomenological consequences of the JIMWLK renormalization group equation on the longitudinal dynamics of heavy ion collisions and the resulting particle spectra.

Résumé

Les collisions d'ions lourds menées au collisionneur d'ions lourds relativistes (RHIC) et au grand collisionneur de hadrons (LHC) sont suffisamment énergétiques pour créer un état de quarks et de gluons déconfinés, soit le Plasma Quarks-Gluons (QGP). Si l'on fait tendre la quantité de mouvement (momentum) vers l'infini, une symétrie longitudinale se manifeste, communément appelée "boost invariance", qui réduit le problème de 3+1 à 2+1 dimensions, simplifiant ainsi les simulations et offrant la possibilité d'étudier propriétés et la dynamique transversales de collisions d'ions lourds à moindre coût numerique. La "boost invariance" n'est toutefois qu'une approximation; une étude complète des collisions d'ions lourds doit inclure les 3 dimensions spatiales. Cette thèse doctorale a pour but d'éntendre le modèle IP-Glasma [1, 2], qui décrit l'état initial de collisions d'ions lourds, à 3+1 dimensions en appliquant aux lignes de Wilson initiales l'évolution de rapidité JIMWLK [3, 4]. Pour éviter la déposition d'énergie à l'extérieur de la région d'interaction, les champs de jauges initiaux des deux noyaux sont modifiés individuellement. Ainsi, la configuration en est une de jauge pure, à l'exception des sources, et ce, dans les 3 dimensions spatiales. De plus, en 3+1 dimensions, le théorème de Gauss ne peut être satisfait de façon triviale, créant donc un ensemble de nouvelles conditions qui doivent être respectées localement. Pour répondre à ces conditions, nous proposons une solution itérative au théorème. La quantification des effets de ces modifications sur les champs chromoélectrique et chromomagnétique, ainsi que sur la pression lors de la phase IP-Glasma, est donc centrale à cette thèse. Ces modifications permettent aussi une évolution temporelle cohérente de l'équation du mouvement classique de Yang-Mills, qui rend à son tour possible une application phénoménologique. L'état initial en 3+1 dimensions IP-Glasma est ensuite jumelé à la simulation hydrodynamique visqueuse MUSIC [5], qui est finalement jointe à UrQMD, un modèle de cascade hadronique [6]. Ce modèle hybride est utilisé pour étudier l'initialisation et l'évolution de collisions Pb-Pb, à $\sqrt{s} = 2.76\,\text{TeV}$, en 3+1 dimensions. Il s'agit donc de la première opportunité d'étudier les conséquences phénoménologiques de l'équation de renormalisation JIMWLK sur la dynamique longitudinale de collisions d'ions lourds et des spectres de particules en résultant.

Acknowledgments

First and foremost, I would like to thank Sangyong Jeon, my supervisor, for his guidance, tutelage, and unwavering support during my graduate studies. I have learned a great deal from his direct supervision, as well as from watching his approach to problem solving. Sangyong also is the initial author of the numerical software that forms the basis for my PhD, and I am grateful for the foundation that this provided for my work, as well as the clarity and precision with which it was coded.

I would like to thank Charles Gale for the supervision and guidance that he has provided. He has served as a second supervisor and I have benefited greatly from his questions, suggestions, and guidance.

In addition, I would like to thank all of the post-docs and my fellow graduate students in the high energy nuclear theory group at McGill during my graduate studies. They have taught me a great deal, and made the process of obtaining a PhD much more enjoyable.

Regarding funding, I would like to thank Compute Canada and Calcul Québec for the computational resources provided to our research group. Finally, I would like to thank the Fonds de recherche du Québec – Nature et technologies (FRQNT) for providing funding through the Bourses d'excellence pour étudiants étrangers (PBEEE).

Author's Contribution

The research done for this thesis utilizes a numerical software that was initially developed by Sangyong Jeon, and transferred to me in an untested state and partially finished state. I tested and verified all aspects of the code, and modified and added components when necessary, in order to produce the correct physical results. In addition to the general testing and verifying of the code, the following specific contributions can be noted on a chapter by chapter basis:

Chapter 1 - This is the introduction and does not directly correspond to the software.
Chapter 2 & 3 - The initial code for the physics described in these chapters was preliminary and untested. I ran multiple tests and checks on these components. I performed the analysis on the conservation of energy in Chapter 3.
Chapter 4 - I implemented and tested the JIMWLK evolution equations, and performed tests and checks for the implementation of Gauss' Law and the alterations done to the initial longitudinal gauge fields. I performed the analysis of the chromo-electric and chromo-magnetic fields, as well as the pressure in 3+1D and their comparison to the 2+1D implementation.
Chapter 5 - I implemented the decomposition of the stress-energy tensor into hydrodynamic fields and the interfacing of the IP-Glasma software with MUSIC.
Chapter 6 - I ran all simulations of IP-Glasma, MUSIC, and UrQMD, including the parameter determination and centrality selection. I did all of the analysis regarding observables and comparison to experimental data.
Chapter 7 - This is the conclusion and does not directly correspond to the software.
Chapter 8 - I implemented the numerical solution to the JIMWLK equations.

Towards Fully 3-Dimensional Simulations of Heavy Ion Collisions in the IP-Glasma Initial State Framework

1

Introduction

1.1 The Proposal and Later Discovery of Quarks

By the 1960's, there was a proliferation in experimentally discovered particle species. In 1964 Murray Gell-Mann [7] and George Zweig [8] independently posited that many of these particles were not fundamental in nature, but composite particles made up of quarks, a set of yet-to-be discovered particles that carry fractional electric charge. It was believed for some time that these particles were mathematical constructs, necessary to make sense of the physics in theoretical terms, but not necessarily real particles that could be observed experimentally.

A series of experiments at Stanford Linear Accelerator Center (SLAC), conducted in the later 1960's and early 1970's (1967-73 for Deep Inelastic Scattering (DIS)) set out to explore the sub-structure of nucleonic matter. Just as Rutherford had bombarded gold foil with alpha particles and discovered the nucleus, these SLAC experiments consisted of bombarding neutrons and protons, known collectively as nucleons, with electrons. Earlier experiments of elastic scattering between electrons and protons suggested that the electric charge of the proton may be relatively evenly distributed, a notion that recalls Thomson's plum pudding model of the atom. If this were the case, one would expect little scattering at high energies and large angles due to the assumed diffuseness of the proton charge. This was not observed [9] for the inelastic cross-section, however, indicating that there are hard scattering centers within the proton, similar to what Rutherford had found in probing atoms with α-particles. Shown in Fig. (1.1) is the ratio of DIS scattering and elastic electron-proton scattering to that of Mott Scattering, or electron-electron scattering. Electrons were understand to behave

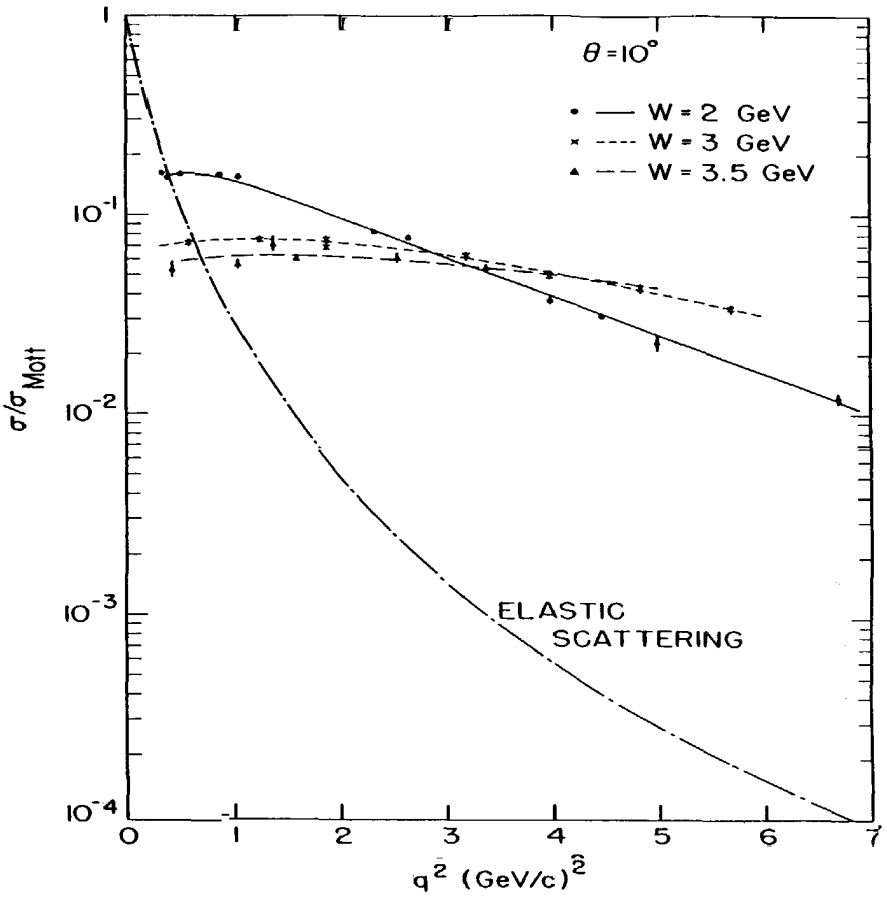

Figure 1.1: Elastic and DIS scattering data at 10 degrees, in ratio to Mott Scattering, as a function of q^2. This plot was taken from [9].

as point particles, so the $\sigma_{DIS}/\sigma_{Mott} \approx 1$ indicated that there were also point-like scattering centers with the proton.

To understand this behavior, consider the deep inelastic scattering (DIS) diagram below, where an electron interacts with a quark inside the proton via a virtual photon and breaks the proton into other hadrons. Assuming elastic scattering between the quark and electron, the outgoing quark has

$$0 \approx (p_q')^2 = (p_q + q)^2 = 2p_q \cdot q + q^2 = 2xP \cdot q - Q^2 \tag{1.1}$$

where the mass of the quark is considered negligible, Q^2 is the virtuality of the photon, and x is the fraction of the proton carried by the parton,

$$p_q = xP. \tag{1.2}$$

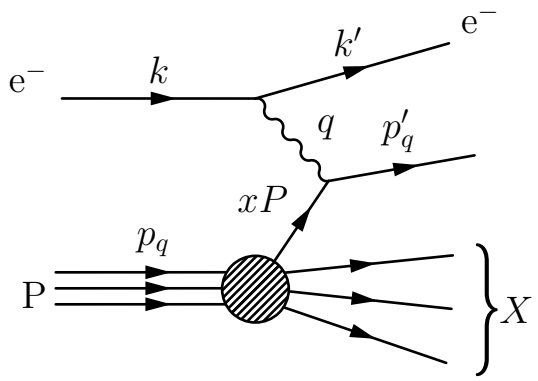

Rearranging, the momentum fraction can be written,

$$x = \frac{Q^2}{2P \cdot q} = \frac{Q^2}{2M_p \nu} \tag{1.3}$$

where $\nu = \frac{P \cdot q}{M_p} = E_e - E'_e$ and Q^2 can be measured from the scattered electron. In this way, experiments can determine the fraction of the hadron momentum of the parton that participates in the collision.

Bjorken proposed a notion of scaling, which argued that hadronic matter behaves as a collection of point-like particles at high energies. Bjorken scaling applies if experimental results are not sensitive to the absolute energy scale of the experiment, but rather are sensitive to certain dimensionless kinematic quantities such as Bjorken x, defined in Eq. (1.3). As can be seen in Fig. (1.1), the value of σ/σ_{Mott} for the DIS data is nearly independent of the momentum transfer. This suggests that the particles that constitute protons are point-like, because, if they weren't, higher momentum transfer would suggest finer spatial resolution, and thus yield some dependence on the momentum transfer.

In addition to finding evidence for discrete scattering centers within the proton, which are understood to be quarks, the DIS experiments compared DIS from protons and neutrons [10]. They found that at high energies, the neutron and proton cross sections were very similar, yielding a ratio near unity, as seen in Fig. (1.2). At lower energies, however, the cross sections differed substantially. This was significant for two reasons: 1) it supported the idea that neutrons and protons were composed of different valence quarks, the neutron of *ddu* and the proton of *uud* and 2) it gave evidence to the idea that nucleons were made of valences quarks, but also a "sea" of quarks that could be probed at higher energies. In the

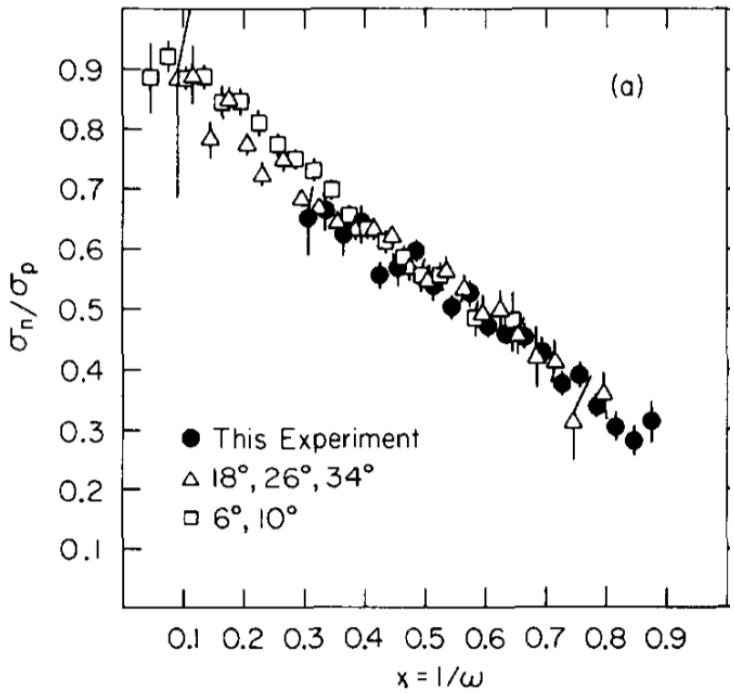

Figure 1.2: The ratio of the DIS cross section of neutrons to that of protons as a function of momentum fraction, x. Plot originally from [10].

high energy limit the valence quarks were less dominant and the sea quarks dominated both the neutron and proton, making them appear much more similar to the incoming electron.

DIS lead to the discovery of quarks and continues to form the basis for understanding the fine structure within hadrons. It will resurface in Chapter 2 in the discussion regarding the wave function of high energy nuclei and the process of gluon saturation.

1.2 Quantum Chromodynamics (QCD)

With experimental verification of the existence of quarks, hadronic matter, or matter that is bound by the strong nuclear force, was beginning to be understood through the quark model. There remained issues however. For example, among the discovered hadrons there existed particles such as the Δ^{++} baryon which was composed of three up quarks with aligned spin and vanishing orbital angular momentum. The Δ^{++} wave function appeared symmetric under the exchange of any two quarks, which were understood to be fermions, in apparent violation of the Pauli exclusion principle. This led the Bardeen, Fritzsch, and Gell-Mann

[11] to propose a new quantum number, known as colour, and that all hadrons were colour singlet states. Colour charge could take one of three values, typically called green, blue, and red. The existence of colour charge resolved the statistics problem for Δ^{++} as well as other discrepancies between theory and experiment, such as the decay rate of a neutral pion into two photons and the cross-section for electron-positron annihilation at high energies into hadrons. Colour charge came to be widely accepted as an exact SU(3) symmetry obeyed by quarks.

The question remained, however, as to why free quarks had not been observed in nature, but only observed in bound states, known as hadrons. Certain non-abelian gauge theories exhibit a property known as confinement [12, 13], and such a theory, Quantum Chromodynamics (QCD), was put forth to describe the strong nuclear force. The action of QCD is given by,

$$S_{QCD} = \int d^4x \left(-\frac{1}{4} F^a_{\mu\nu} F^{\mu\nu a} + \sum_f \bar{\psi}_f \left(i \not{D} - m_f \right) \psi_f \right) \tag{1.4}$$

where f is an index that runs over the number of quark flavors, and a is a color index that runs from 1 to 8. Feynman's slash notation $\not{D} = \gamma^\mu \partial_\mu$ is used, where γ^μ are Dirac matrices. Here the field strength tensor $F^a_{\mu\nu}$ and the covariant derivative are defined, respectively, as

$$F^a_{\mu\nu} = \partial_\mu A^a_\nu - \partial_\nu A^a_\mu - g f^{abc} A^b_\mu A^c_\nu \tag{1.5}$$

and,

$$D_\mu = \partial_\mu + i g A^a_\mu t^a. \tag{1.6}$$

Here f^{abc} is a structure constant particular to the Lie algebra of the group.

QCD is a specific instance of broader class of theories known as Yang-Mills theories, and is the fundamental field theory governing quarks and gluons. Unlike Quantum Electodynamics (QED), it is a non-abelian gauge theory, and obeys the SU(3) charge symmetry. A critically important implication of this fact is that the coupling constant, which characterizes the strength of the interaction between elementary particles of the theory and is denoted as g in Eq. (1.6), actually increases with distance or equivalently decreases with increasing energy, the opposite behavior from QED.

This means that at short distances, quarks are relatively free, but as one tries to separate two quarks, the force becomes constant, until eventually it becomes energetically favorable to produce two new quarks out of vacuum, leaving two colourless bound states where there was originally one. This is the notion of *color confinement* that prevents the observation of free quarks.

There is an intuitive physical picture that is useful in thinking about this important difference between QED and QCD based on the microscopic physics. In Quantum Field Theory (QFT), where the vacuum can be polarized much like a dielectric, an electric charge does just that. Probed at higher and higher energies, the spatial resolution increases and one is able to resolve the electric charge. At larger distances, however, the electric charged is screened

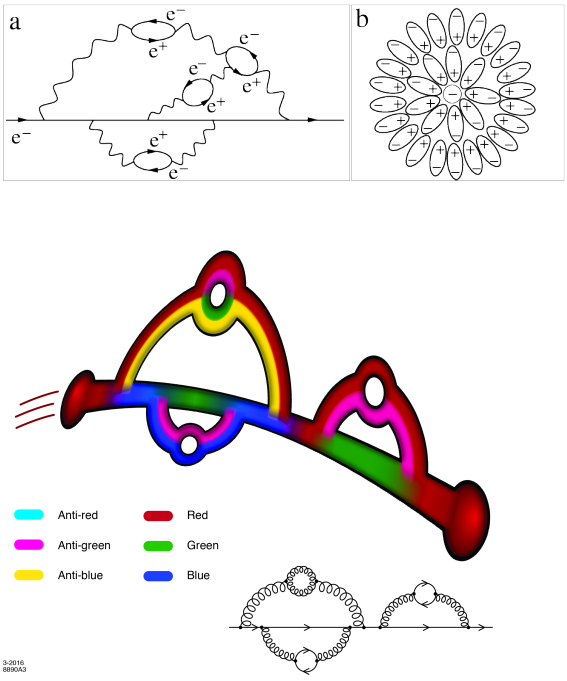

Figure 1.3: Top: schematic illustration of QED screening phenomenon. Bottom: schematic illustration showing gluons carrying away some of the quark colour charge, leading to the QCD anti-screening phenomenon. Figures from [14].

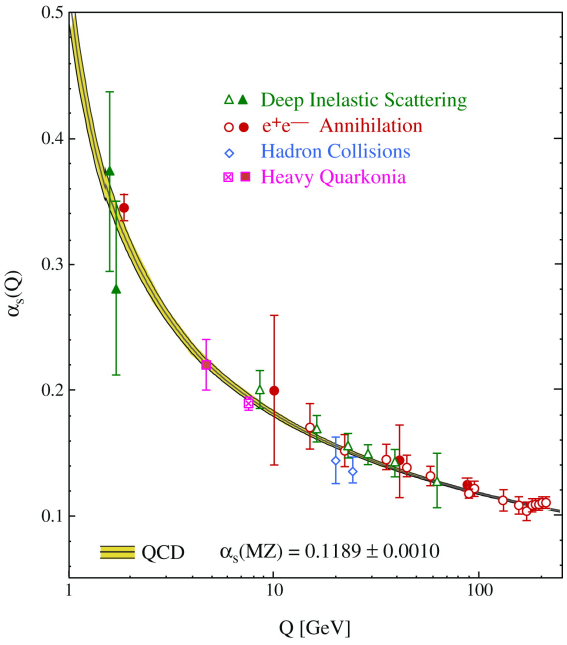

Figure 1.4: Figure showing the running of the coupling in QCD, and the asymptotic freedom at large energy scales, as taken from [15].

by the surrounding charge anti-charge pairs that arise out of the vacuum polarization, shown in the top left of Fig. (1.3). Due to electric attraction, the vacuum charge that is oppositely charged tends to be to the original charge. Drawing a Gaussian surface then will enclose less charge, meaning the strength of the field at a distance r is less than that due to the original charge. This is the idea of screening and is one way of understanding the running of the QED coupling getting larger at higher energies, or smaller length scales. A more technical way to do so would be to say that the QED beta-function, which quantifies how the coupling changes as a function of energy scale, is positive, and at the one-loop level is given by

$$\beta_{QED}(r) = \frac{\partial g}{\partial \log \mu} = \frac{2\alpha^2}{3\pi} > 0. \tag{1.7}$$

In QCD, however, the force carrying gauge bosons, the gluons, are themselves charged under QCD. Just as in QED, a QCD test charge will induce a vacuum polarization. However, the gluons that mediate the force between the test charge and the induced charge anti-charge pairs will themselves carry away some of the charge of the original test charge. In effect, the gluons will spread out the charge, leading to the opposite behavior of QED, known as anti-screening. This is schematically depicted in the bottom left panel of Fig. (1.3), in which the red color charge of the initial quark is dispersed away due to the color charge carrying gluons. In terms of the coupling, anti-screening means that the coupling increases with increasing distance (decreasing energy), as shown in Fig. (1.4), both in various experiments and in terms of the theory of QCD. This idea, that the coupling, usually denoted as α_s, goes to zero, as the energy scale goes to infinity, is known as *asymptotic freedom*. At leading order, the strong coupling constant at a scale Q^2 is usually written,

$$\alpha_s(Q^2) = \frac{1}{\beta_0 \ln Q^2/\Lambda^2} \tag{1.8}$$

where $\Lambda \approx 200\,\text{MeV}$ is a scale parameter and $\beta_0 = \frac{11N_c - 2n_f}{12\pi}$, where N_C is the number of colors, and n_f is the number of quark flavors. The form of Eq. (1.8) clearly decreases with increasing energy.

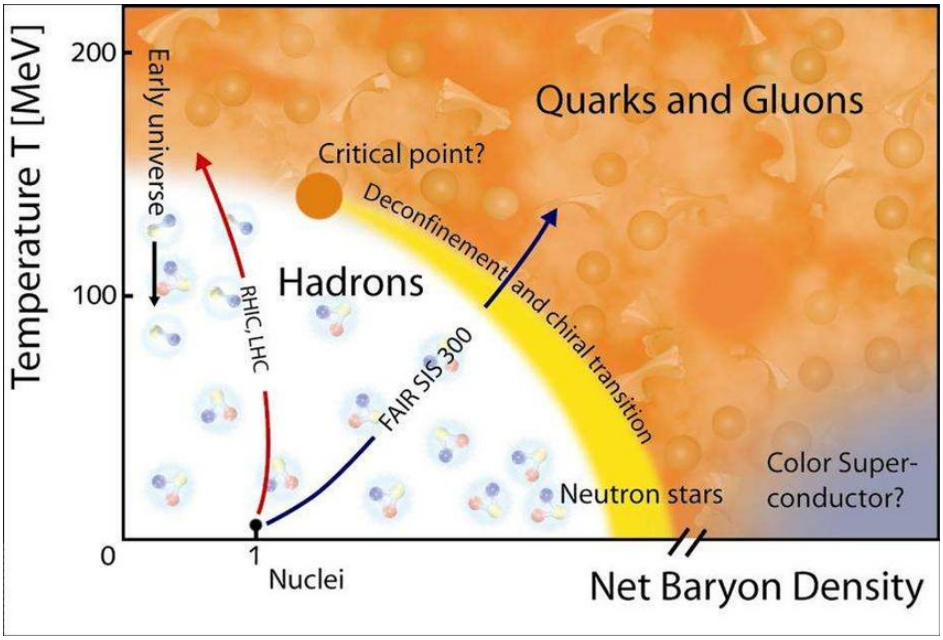

Figure 1.5: Possible phase diagram of QCD. This figure was taken from [16].

1.3 Quark Gluon Plasma and Heavy Ion Collisions

Asymptotic freedom means that at sufficiently high temperatures, where the strong coupling becomes small, it is possible to liberate quarks and gluons. This idea can be represented in a phase diagram of QCD, as done in Fig. (1.5), where quarks and gluons become free above certain temperatures and baryon densities. Indeed, lattice QCD simulations indicate a liberation of colour degrees of freedom at around 155 MeV [17], as shown in Fig. (1.6).

To see why this suggests the liberation of quarks and gluons, consider the Stefan-Boltzmann law, which says that the ratio ϵ/T^4, where T is temperature and ϵ is the energy density, should be proportional to the number of degrees of freedom in the system. For a gas of light mesons, say pions, $N_\pi^{dof} = 3$, whereas for a system made up of the free quarks and gluons that compose pions,

$$\begin{aligned} N_{\text{quarks}} &= \Big[(spin) \times (colors) \times (flavours) \times (q \, or \, \bar{q})\Big] = 2 \times 3 \times 2 \times 2 = 24 \\ N_{\text{gluons}} &= \Big[(colors) \times (spin)\Big] = 8 \times 2 \end{aligned} \tag{1.9}$$

so for 2 flavours,

$$N_{dof} = N_{gluons} + N_{quark} = 16 + 24 = 40 \tag{1.10}$$

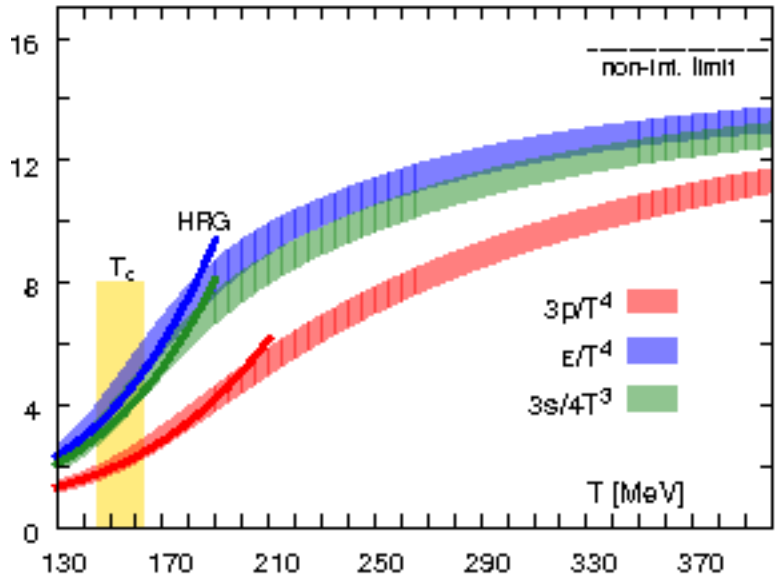

Figure 1.6: The rapid increase in these quantities indicates a liberation of degrees of freedom. The lack of a peak or divergence indicates that there is no phase transiton but rather a smooth crossover from hadron gas to quark gluon plasma. Plot taken from the hotQCD collaboration [17].

This rapid increase in the degrees of freedom can be seen in the lattice QCD calculation shown in Fig. (1.6).

Experimentally, heavy ion collisions conducted at the Large Hadron Collider (LHC) and the Relativistic Heavy Ion Collider (RHIC) reach sufficiently high energies to create Quark Gluon Plasma (QGP), a deconfined state of quarks and gluons, in the laboratory. These experiments accelerate heavy ions, such as lead or gold nuclei, to nearly the speed of light. These highly Lorentz contracted pancake-like nuclei, collide and rapidly create a hot, dense state of deconfined quarks and gluons. The QGP behaves like a near-perfect fluid with an extremely low shear viscosity to entropy density ratio. As the QGP expands and cools it reaches temperatures below the QCD confinement temperatures and turns back into hadrons, a process that is often referred to as "hadronization."

Outside of the laboratory, it is believed that the early universe was comprised of Quark Gluon Plasma (QGP) microseconds after the Big Bang [18], and could be present in the interior of neutron stars [19].

1.4 Evidence of Quark Gluon Plasma

Heavy Ion Collisons are incredibly violent and short lived, creating a QGP fireball that only survives for on the order of 10 fm/c or about 10^{-23} seconds and can create tens of thousands of particles. In order to study QGP, one must infer the behavior indirectly from the particle spectra that are detected at the particle detectors. Nonetheless, there is convincing experimental evidence that a deconfined state of quarks and gluons is formed.

There are two prominent signatures of the formation of QGP, one in the high p_T part of the spectrum, and the other in the low p_T, where p_T is simply the momentum of the final states particles that is transverse to the beam axis. In the low p_T, or "soft", part of the the spectrum the particles exhibit a collective behavior or "flow," that can be measured by the two particle correlation, as seen in Fig. (1.7). In particular, notice that the two particle correlation has a "ridge" at $\Delta\phi = 0$ indicating that the angle of the particles' momentum in the transverse plane is correlated in the longitudinal direction. This long-range rapidity correlation indicates that there is a collective behavior among the particles.

Hydrodynamics provides a natural explanation of this phenomenon, and indeed has been incredibly successful in describing experimental results. If one considers the collision of two nuclei, where the two nuclei are offset by some distance perpendicular to the collision axis, known as the impact parameter and usually denoted "b", then as the impact parameter increases from zero, the overlap region of the colliding nuclei will become almond-shaped. In terms of hydrodynamics, the almond-shaped, or elliptical, spatial energy deposition leads to differences in pressure gradients along the major and minor axes of this elliptical shape. The difference in pressure gradients will lead to an anisotropy in the momentum distribution of the final state particles, which is typically characterized by v_2, the second Fourier coefficient obtained by a Fourier decomposition of the azimuthal angle of the particle spectrum,

$$\frac{dN}{p_T dp_T dy d\phi} = \frac{dN}{2\pi p_T dp_T dy}\left(1 + \sum_{n=1} 2v_n(y, p_T)\cos\left[n(\phi - \psi_n)\right]\right). \tag{1.11}$$

In general, a spatial anisotropy of the nth order, often characterized by

$$\epsilon_{\mathbf{n}} = \frac{\int d^2x r^n \varepsilon(\mathbf{x}) e^{in\phi}}{\int d^2x r^n \varepsilon(\mathbf{x})}. \tag{1.12}$$

where $\varepsilon(\mathbf{x})$ is the local energy density at position $\mathbf{x}$ in the transverse plane, will be translated by hydrodynamic pressure gradients to a momentum anisotropy of the same order which can be quantified by the v_n Fourier coefficient [21, 22]. These include ellipticity ($n = 2$), triangularity ($n = 3$) as first proposed in [23], quadrangularity ($n = 4$), and so on. This can be seen clearly in Fig. (1.8). In panel (a), the position of nucleons from two colliding nuclei, offset by a finite impact parameter, are shown in purple and green, respectively. In panel (b), the resulting deposition of energy using simple geometric cross-sections for nucleon-nucleon interactions shows a globally elliptical shape, with additional fluctuations. The red arrows

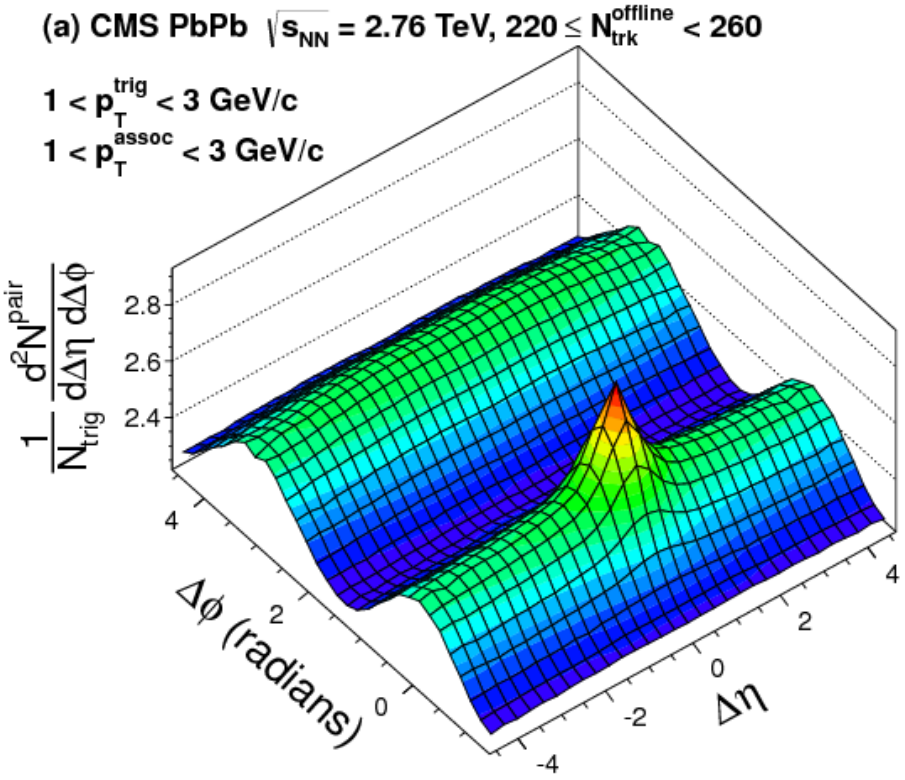

Figure 1.7: The so-called "ridge" phenomenon in HIC's. Plotted is the two particle correlation as a function of $\Delta\phi$, or azimuthal angle separation of the particles, and the $\Delta\eta$ separation. One can see that there is a ridge at $\Delta\phi = 0$ radians that is long-range in $\Delta\eta$. This shows the flow, or collective behavior of particles responding to the initial geometry. Fig. from [20]

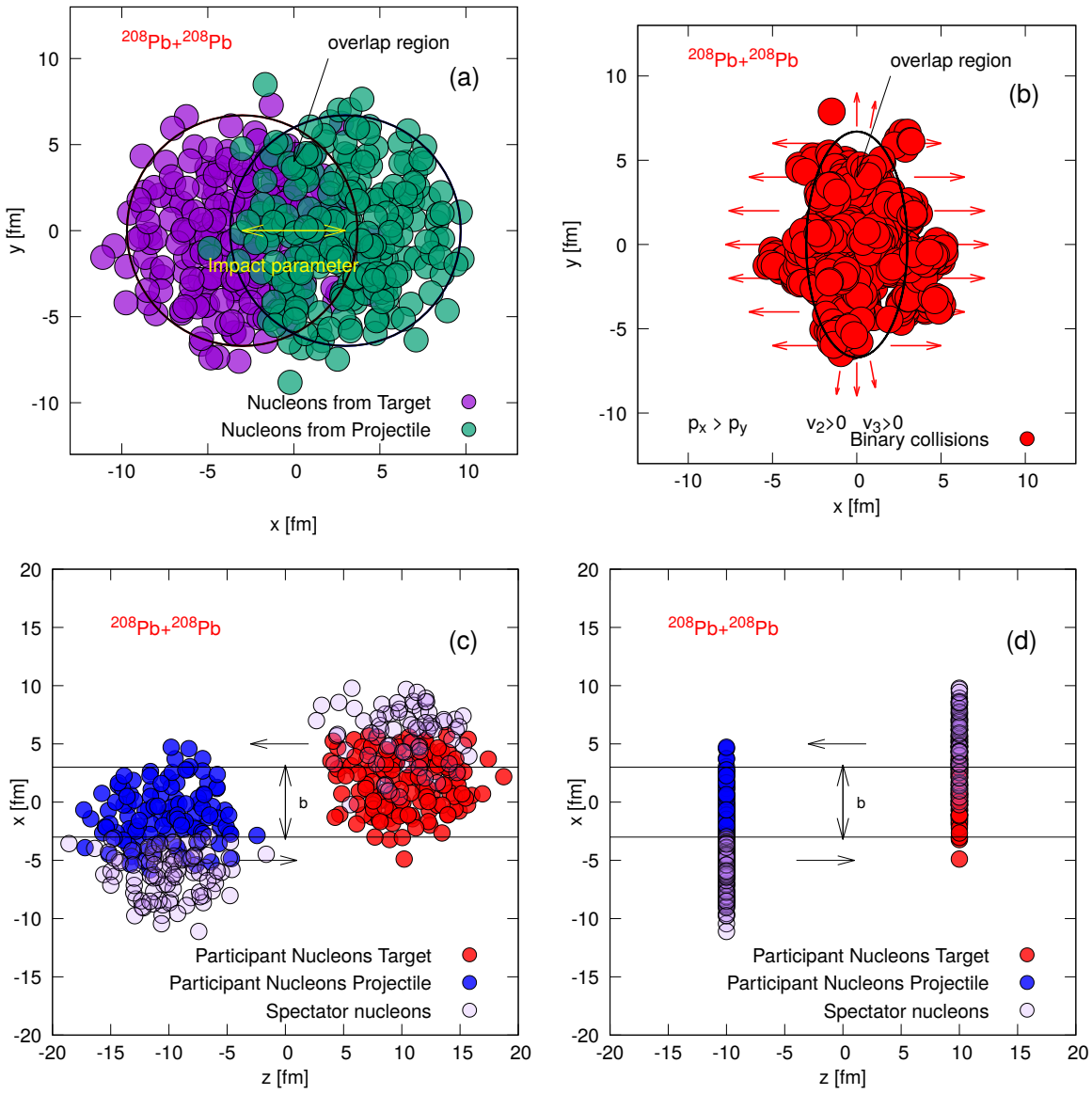

Figure 1.8: (a) Two colliding Pb nuclei for which the positions of the nucleons were sampled from a Wood-Saxon distribution. The non-zero impact parameter leads to an elliptical overlap region, which the sampled nucleon positions giving rise to fluctuations around this shape. (b) The locations of binary nucleon-nucleon collisions from the collision in panel (a). The arrows are a schematic representation of the momentum generated from the difference in pressure gradients between the x and y directions. (c) A cross section along the beam axis and impact parameter axis showing two incoming nuclei with fluctuating nucleon positions. This figure does not show the Lorentz contraction of the nuclei. (d) Same as (c) but showing Lorentz contraction of nucleus (not showing Lorentz contraction in nucleons).

are a schematic representation of the different pressure gradients at play. This collision will lead to non-zero momentum space anisotropies v_2 and v_3.

The high p_T signature for QGP involves the hard scattering of two partons that form a collimated beam of hadrons, known as a jet. Jets are created in proton-proton (p-p) collisions, where the presence of QGP is assumed absent, as well as in nucleus-nucleus (A-A) collisions, where it is believed to form. One can compare the detected particle spectrum from these jets in the two cases mentioned. Typically one considers a quantity known as R_{AA}, which is simply the ratio of the particle spectra in A-A collisions over the spectra in p-p collisions, normalized by the number of binary nucleon-nucleon collisions in the A-A collision. In the case of nucleus-nucleus collisions, R_{AA} is well below unity, indicating that the jet loses energy, a process known as jet quenching. This suggests that a bulk medium, namely QGP, is formed, with which the jet interacts and to which it loses energy.

This thesis will focus primarily on the soft part of the spectrum and the flow signature of QGP, but its contents also have implications for high-p_T that will not be explored here.

1.5 Stages of Heavy Ion Collisions

Experimentally, we are unable to directly observe the initial state or the dynamical evolution of the collision, but only the final state particles. This means we can only study the dynamics of the Quark Gluon Plasma indirectly by building phenomenological models and comparing simulations to data from the final state particle spectra in order to make inferences about the formation and evolution of QGP.

Heavy ion collisions explore high temperature, many-body QCD. Without being able to solve the fundamental QCD equations in this context, it is necessary to rely on effective field theories and models to describe these incredibly complex processes. As of now, no single theoretical framework can describe the entirety of these collisions, so HIC's are typically modelled in three stages: the initial condition, a relativistic hydrodynamic phase, and finally a hadron gas phase. A brief description of HIC's is included below, along with Table 1.1 outlining the different phases and the accompanying numerical softwares used.

Before the collision, the heavy ions are accelerated to nearly the speed of light, resulting

in highly Lorentz contracted nuclei in the lab frame. This is shown schematically in panels (c) and (d) of Fig. (1.8). These highly boosted, pancake-like nuclei collide and form a gluon dominated state that can be described by strong classical fields. The system is believed to reach the necessary conditions for the applicability of relativistic hydrodynamics on an incredibly short time scale on the order of 0.1-1.0 fm/c. The exact criteria for the applicability of hydrodynamics and the mechanism by which it reaches this criteria is still very much debated in the field [24]. For the purposes of this thesis, in which only Pb-Pb collisions are studied, the theoretical applicability of hydrodynamics is widely accepted, and the phenomenological success of the hydrodynamic framework is considered as evidence of the formation of QGP. The controversy regarding the applicability of hydrodynamics arises in so-called "small" systems, such as proton-nucleus collisions.

At this point the system is comprised of quarks and gluons and is described well by relativistic hydrodynamics with an extremely small shear viscosity to entropy density ratio, sometimes described as a "near perfect fluid." As the system expands and cools, it drops below the deconfinement temperature, and the quarks and gluons hadronize, forming a gas of hadrons that includes resonances as well as stable particles. These hadrons undergo decays and scatterings until they reach kinetic freezeout and no longer interact. At this point the particles can be analyzed and compared to experimental data, which is collected when the particles reach the particle detectors.

Table 1.1: Table showing the complexity of heavy ion collisions along with the variety of models and numerical simulations used to study them in this thesis (adapted from [25]).

Description	**Time**	**Prevailing Theory**	**Simulation Used**
Before the collision	$\tau < \tau_0$	Color Glass Condensate/JIMWLK	3+1D IP-Glasma
Immediately after the collision	$\tau_0 < \tau < \frac{1}{Q_s}$	Strong Classical Fields - Glasma	3+1D IP-Glasma
Thermalization/Isotropization/ Hydrodynamization	$\frac{1}{Q_s} < \tau < \tau_{equilibrium}$	Glasma/Kinetic Theory/Hydro	3+1D IP-Glasma
QGP (Hydrodynamics)	$\tau_{equilibrium} < \tau < \tau_{freezeout}$	Relativistic Viscous Hydrodynamics	3+1D MUSIC
Hadron Gas	$\tau_{freezeout} < \tau < \tau_{freestream}$	Hadron Gas	UrQMD
Free Streaming	$\tau_{freestream} < \tau$	Particles free stream to detectors	UrQMD

1.6 Goal of this thesis

The dominant assumption made in Heavy Ion Collisions is that of boost invariance, or infinite momentum. Boost invariance means that a Lorentz boost along the direction parallel to the beam axis will leave the physics unchanged. In this limit, the system becomes effectively 2+1D and many problems become greatly simplified. Notationally speaking, "boost invariant", "2D", "2+1D" to include the temporal dimension, and "the infinite momentum limit" will be used interchangeably to describe this idea throughout this thesis.

This assumption has allowed for great progress and understanding of the transverse dynamics of heavy ion collisions but has limited our understanding of the longitudinal dynamics of HIC's. In reality, HIC's evolve in 3+1D and thus one must relax this assumption in order to study HIC's in their entirety.

To be fair, the collision energies at the LHC reach γ-factors in the 1000's, meaning, classically, a Pb nucleus that is usually about 13 fm/c in diameter, becomes Lorentz contracted to less than 0.01 fm/c along the beam axis in the lab frame. Experimental evidence of the post collision results also suggests that deviations from boost invariance are relatively small within a kinematic range. At the same time, experiments have yielded data that suggests that, despite the approximate validity of boost invariance, there is critical physics to be explored and understood in the longitudinal dynamics of HIC's [26, 27]. Such data can help constrain models and yield additional insight into the physics of HIC's, particularly in the initial state, which sources long range rapidity correlations. Furthermore asymmetric collisions such as those between a proton and a nucleus (pA collisions) are clearly not boost invariant. This can be seen clearly in Fig. (1.9) which shows that for central collisions the multiplicity is consistently higher on the Pb going side of a p-Pb collision. These systems are often approximated as boost invariant, but should not be. In order to adequately study asymmetric collision systems, it is crucial to have fully 3-dimensional simulations that do not assume the boost invariant longitudinal symmetry. As stated in one of the early papers formulating the boost invariant Colour Glass Condensate effective theory [29],

> "the solution is up to trivial factors rapidity independent. This has *amusing* phenomenological consequences for the collisions of asymmetric nuclei. The dis-

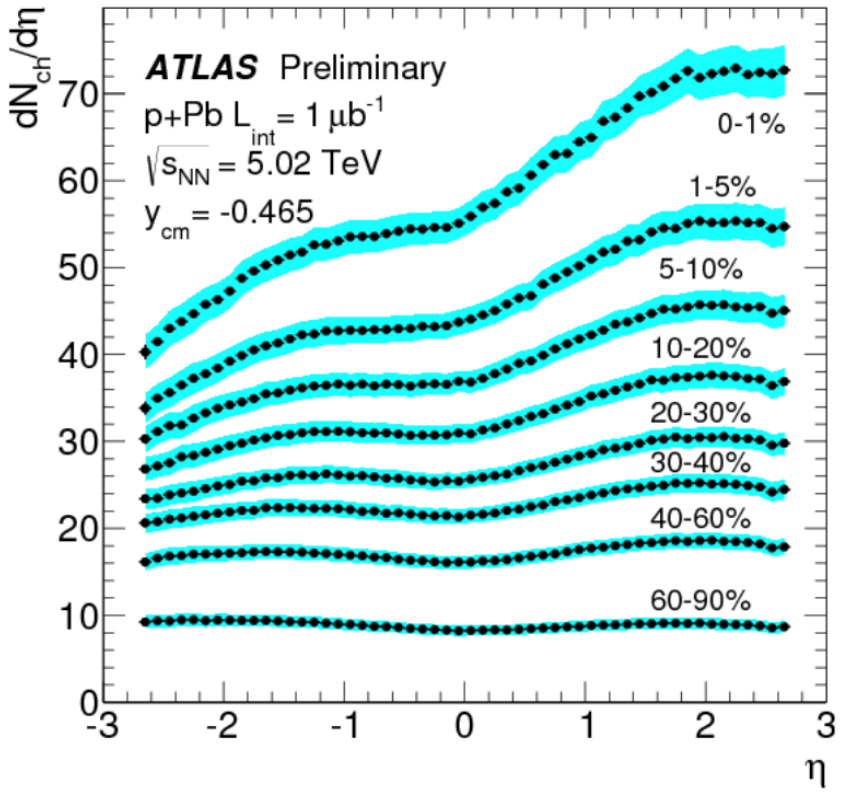

Figure 1.9: ATLAS data [28] showing the asymmetry in $dN_{ch}/d\eta$ for p+Pb collisions.

tribution should be flat in rapidity." (emphasis added)

The second and third stages of the standard model of HIC's, namely the hydrodynamics [30] and hadronic gas phases [6, 31], have been generalized to 3+1D. The initial state, however, has lagged and realistic first-principles based initial conditions that are phenomenologically applicable remain scarce in the field. This poses a problem because the rest of the evolution of the QGP, i.e. the subsequent hydrodynamic and hadronic gas simulations, rely on and are sensitive to the initial condition. The high energy nuclear wave functions of the colliding nuclei imprint themselves on the collision, seeding long range rapidity correlations within the evolving QGP. Thus, without constraining the initial condition, it is difficult to pin down important physical parameters of QGP, such as its transport coefficients, including the shear and bulk viscosities.

In particular, the dominant physical framework for the initial stage is that of the Color

Glass Condensate (CGC), an effective field theory and novel state of matter that is believed to describe high density ultra-relativistic nuclei. CGC based models and calculations have had impressive agreement with experimental results, and the electron-ion collider [32] will soon search for conclusive evidence of the formation of CGC.

The Color Glass Condensate, to be discussed in detail in Chapter 2, argues that the gluon density of high energy nuclei saturates and forms a condensate of gluons. It has yielded a large amount of scholarship on the initial conditions of heavy ion collisions, including a crucially important Monte-Carlo simulation known as IP-Glasma, which this thesis aims to generalize. IP-Glasma [1, 2] has been extremely successful phenomenologically in describing a wide range of observables in heavy ion collisions both in terms of event averages as well as event by event distributions. Unlike many of the other initial conditions on the market, such as MC-Glauber, IP-Glasma is based in first principles and involves quarks and gluons.

The original formulation of IP-Glasma was 2+1D. The goal of this thesis is to extend the phenomenologically successful IP-Glasma model to 3+1D while retaining its key features. In doing so, we hope to explore the longitudinal dynamics of heavy ion collisions, and to verify to what degree the transverse dynamics of the 2+1D formulation hold for a 3+1D generalization.

1.7 Claims of Originality

There have been a variety of approaches to developing 3+1D initial conditions for the initial state of heavy ion collisions [4, 33, 34, 35, 36, 37]. These works implemented a rapidity dependence in a number of different ways including by JIMWLK evolution of the pre-collision Wilson lines [4], as is done in this thesis, through rapidity fluctuations [33, 34], by including color sources [36], or by dynamically initializing hydrodynamics with source terms [37].

In this thesis, the rapidity dependence of the model comes from the JIMWLK renormalization equations, as was done in [4]. The novel part of this thesis is the adaption of the initial condition for the gauge fields and electric fields to allow the system to be evolved on a 3-dimensional lattice and, most importantly, to make the simulation phenomenologically applicable. In particular, the solution for the initial gauge fields from the Color Glass

Condensate (CGC) are altered to be pure gauge in all three spatial directions, rather than just the transverse directions. This prevents non-physical energy deposition outside of the interaction region between the two nuclei. Additionally, an ansatz is proposed such that Gauss' law can be enforced locally through the iterative Jacobi method, without needing to include dynamical color sources.

The 3+1D simulation is used in conjunction with MUSIC [38] and UrQMD [6] to compute and analyze the hadronic spectrum. The effects of JIMWLK rapidity fluctuations on longitudinal hadronic observables is explored for the first time.

1.8 Putting IP-Glasma in the Context of the Initial State of Heavy Ion Collisions

In introducing the main focus of this thesis, the IP-Glasma model, it is useful to to do so in the context of the most commonly used model, at least historically, for the initial condition of heavy ion collisions, the Glauber model. The aim is to both acknowledge the usefulness of the Glauber model, and to motivate the need to go beyond it.

Due to Lorentz contraction, the nuclei involved in high-energy heavy ion collisions are essentially 2-dimensional in the lab frame, reaching γ-factors in the 1000's at the LHC. When the two nuclei collide, there is an overlap region, where the interaction takes place and where energy is deposited in the plane transverse to the beam axis.

Nuclei are extended objects, and thus a natural place to begin understanding and modelling nuclear collisions is with the shape of nuclei themselves. Elastic electron scattering experiments are able to measure the charge radius of nuclei [39], which are usually parametrized by a Woods-Saxon distribution,

$$\rho(r) = \rho_0 \frac{1 + \omega(r/R)^2}{1 + \exp\left(\frac{r-R}{a}\right)} \tag{1.13}$$

where ρ_0 is the density at the center of the nucleus, $\omega(r/R)$ deforms the nucleus away from the regular Woods-Saxon shape, R is the nuclear radius, and a is the nuclear skin thickness. Given this information, the simplest way to model the nucleus is by a smoothly varying density function that takes the form of Eq. (1.13). This is what is done in the Glauber

model, a useful review of which can be found here [40].

In the Glauber model, one can define the nuclear thickness function

$$T_{A(B)}(\mathbf{s}) = \int_{-\infty}^{\infty} \rho_{A(B)}(\mathbf{s}, z_{A(B)}) dz_{A(B)} \tag{1.14}$$

where $A(B)$ correspond to the projectile (target), $\mathbf{s}$ is the position in the transverse plane, and $z_{A,B}$ is the position along the beam axis. The normalization condition is usually taken to be $\int d^2 s T_{A(B)}(s) = 1$. The overlap region, and thus the geometry of the collision at a given impact parameter b, is given by

$$T_{AB} = \int T_A(\mathbf{s}) T_B(\mathbf{s} - \mathbf{b}) d^2\mathbf{s} \tag{1.15}$$

This model, often called "smooth" or "optical" Glauber, treats the nuclei as continuous charge distributions and is already able to produce energy deposition that, when coupled to relativistic hydrodynamics, can produce reasonable values for the elliptical flow coefficients v_2. However, this model yields a triangular flow coefficient, v_3, that is identically zero, a feature that is inconsistent with data. In [23], a non-negligible value of v_3 was measured at RHIC for Au-Au collisions, and fluctuations were proposed as an important feature in the initial state of heavy ion collisions. The success of smooth Glauber in describing v_2 data can be taken as confirmation that v_2 is primarily driven by the global geometry of the collision as determined by the impact parameter.

One way to include initial state fluctuations is to allow the position of nucleons to fluctuate within the nuclei. Rather than model the entire nucleus with the Wood-Saxon charge distribution, one can sample the position of the nucleons according to that distribution. This will lead to event to event fluctuations in geometry and more complex geometric configurations for the energy deposition, as can be seen in panel (a) of Fig. (1.8).

This model, known as Monte Carlo Glauber, or MC-Glauber, relies on the measured cross-section for inelastic nucleon-nucleon collisions, σ_{inel}^{NN}, as an input. One implementation of the model treats the nucleons as hard disks, meaning if a nucleon from the target is less than a distance

$$d \leq \sqrt{\sigma_{inel}^{NN}/\pi} \tag{1.16}$$

from a nucleon in the projectile nucleus, then a *binary collision* is deemed to have taken place and these two nucleons deposit energy. Then the collision is treated as a collection of independent nucleon-nucleon collisions. Nucleons that undergo at least one binary collision are said to be *participants* and those that do not are *spectators*.

MC-Glauber is modelled entirely based on geometric considerations of nuclear collisions, and takes input parameters from experiment to determine the Wood-Saxon parameters (R, a) and the nucleon-nucleon inelastic cross section (σ_{inel}^{NN}). It is able to produce non-zero values for higher order, fluctuation driven flow harmonics, such as v_3 [41].

The Glauber models (smooth and MC) are extremely useful in both their simplicity and effectiveness in describing general geometric features of nuclei in nuclear collision. However, they do not consider QCD or quarks and gluons. Furthermore, they are not dynamical models, and thus cannot describe the system's evolution towards hydrodynamic applicability. Instead, they typically initialize hydrodynamic simulations at a non-zero proper time τ_0 without any evolution and are only able to initialize one of the hydrodynamic fields, ε, the local energy density.

Furthermore, it is important to note that v_2 and v_3 are quite sensitive to hydrodynamic parameters, primarily the shear viscosity to entropy density ratio η/s, which can be tuned to improve agreement. As one of the primary goals of the field is to determine the transport coefficients of QGP, such as η/s, it is crucial to have as realistic an initial state model as possible in order to be able to reliably extract information about the QGP. The Glauber models are important in that they illustrate that the p_T-integrated v_2 is primarily impact parameter driven, as was suspected, and thus any model that implements energy deposition as an effective overlap of the colliding nuclei will roughly exhibit this behavior, if evolved hydrodynamically. Similarly, MC-Glauber showed that fluctuations are indeed important to reproduce experimental p_T-integrated v_3, and that the relevant length scales for this observable are at the order of the size of a nucleon, ≈ 1 fm. Finally, while MC-Glauber can obtain agreement with event averaged quantities such as v_2 and v_3, it is not able to describe the distributions of these quantities in as broad of a range of centrality classes as IP-Glasma [42]. While event averaged v_n's are important observables, the flexibility of hydrodynamic

parameters allow for a wide range of initial state models to describe these observables. The v_n distributions, however, capture the event-by-event fluctuations which are largely independent of hydrodynamic variables, and thus more able to discriminate between initial state models. IP-Glasma was able to describe the v_n distributions quite well [42], and other models have since been able to do so [43]. The common feature between IP-Glasma and Trento that is likely responsible for this is the energy deposition between the nuclei goes as the product of the thickness functions of the two nuclei raised to some power.

IP-Glasma is a model that incorporates the important features of MC-Glauber in terms of modelling the nucleus as a Woods-Saxon with fluctuating nucleon positions. In addition, IP-Glasma includes sub-nucleonic fluctuations that arise from color charge fluctuations in hadronic matter at small momentum fraction. The scale of the color charge fluctuations are related to the gluon saturation scale, which is determined via the IP-Sat model [44] and constrained using DIS data. Gluon saturation is a phenomenom, to be discussed in the next chapter, of high energy hadrons in which the gluon density saturates. The color charge is used to solve for the gauge fields, and the gluon are evolved dynamically using the Classical Yang-Mills equations of motion. Thus, IP-Glasma incorporates the fine scale partonic structure of nuclei as determined by DIS, and evolves the gluon fields, providing a QCD based dynamical model that involves a full stress-energy tensor $T^{\mu\nu}$ for the initial state of heavy ion collisions.

Phenomenologically, IP-Glasma has had success is describing the event-by-event distributions of v_n [42, 45] and charged hadron multiplicity [1, 2, 46], as well as observables that involve higher order correlations [47]. It has been used for many collision systems including small systems [48, 49], deformed nuclei, and other asymmetric collisions [50]. Finally, an extensive Bayesian analysis [51] of the many existing models and parameters involved in heavy ion collision simulations found the IP-Glasma model to be compatible with experimental data, and among the two initial state models most preferred by data, along with EKRT [52].

1.9 A note on units and conventions

Before proceeding, a quick note on units and conventions is in order. In this thesis, so-called "natural units" will be used everywhere unless explicitly stated otherwise. Natural units in high energy physics means

$$\hbar = c = k_B = 1 \tag{1.17}$$

where

$$\begin{aligned} c &\equiv \text{speed of light} \\ \hbar = \frac{h}{2\pi} &\equiv \text{Planck's contant}/(2\pi) \\ k_B &\equiv \text{Boltzmann's constant} \end{aligned} \tag{1.18}$$

Using natural units means that it is not necessary to keep track of these constants during the calculation, but these quantities can be restored at the end using simple dimensional analysis.

In these units, energy and length are inverses. A useful combination, that is used to convert between energies and lengths, is

$$\hbar c = 0.1973\,\text{GeV fm}. \tag{1.19}$$

Regarding gauge field notation, the following convention,

$$D_\mu = \partial_\mu + igA_\mu \tag{1.20}$$

with a plus sign, corresponds to

$$\begin{aligned} F_{\mu\nu} &= \frac{-i}{g}[D_\mu . D_\nu] \\ &= \partial_\mu A_\nu - \partial_\nu A_\mu - \frac{i}{g}[igA_\mu, igA_\nu] \\ &= \partial_\mu A_\nu - \partial_\nu A_\mu + ig[A_\mu, A_\nu] \end{aligned} \tag{1.21}$$

with a plus sign in the commutator term. This in turn means that the proper form of the gauge transformation is

$$A'_\mu = V(A_u - \frac{i}{g}\partial_\mu)V^\dagger, \tag{1.22}$$

with a minus sign. Different conventions are used for these terms, so it is important to clarify at the outset, for the both the reader and the author. In order to be consistent with the literature, the following convention will be used in Chapter 2,

$$\begin{aligned} D_\mu &= \partial_\mu - igA_\mu \\ F_{\mu\nu} &= \partial_\mu A_\nu - \partial_\nu A_\mu - ig[A_\mu, A_\nu] \\ A'_\mu &= V(A_\mu + \tfrac{i}{g}\partial_\mu)V^\dagger. \end{aligned} \tag{1.23}$$

This will be noted explicitly for clarity.

2

Color Glass Condensate

2.1 CGC Overview

The Colour Glass Condensate (CGC) is an effective field theory that describes the gluon saturation regime of high energy hadrons. The CGC is based on a separation of scales in which the hard partons of high energy nuclei act as static sources for highly abundant small-x gluons. The terms "hard" and "large-x" partons will be used interchangeably, and refer to the partons, either quarks or gluons, that carry a large fraction of the longitudinal momentum of the hadron with which they are associated. Similarly, "soft" or "small-x" partons refer to those partons that carry a small fraction of the momentum of the hadron.

The CGC action is given by

$$S_{CGC} = \int d^4x \left(-\frac{1}{4} F^a_{\mu\nu} F^{\mu\nu a} + J^{\mu a} A^a_\mu \right). \tag{2.1}$$

One can see that it bears a resemblance to the QCD action, given in Eq. (1.4), except the quark term is replaced by a source. The source $J^{\mu a}$ represents the hard partons that source soft gluons, denoted by A^a_μ. In this section we aim to justify this action, and to comment on its implications.

First, to motivate the separation of scales, it is convenient to introduce light-cone coordinates,

$$x^\pm = x_\mp = \frac{x^0 \pm x^3}{\sqrt{2}} \tag{2.2}$$

where the metric is given by

$$g_{\mu\nu}(x^+, x^-, x, y) = \begin{pmatrix} 0 & 1 & 0 & 0 \\ 1 & 0 & 0 & 0 \\ 0 & 0 & -1 & 0 \\ 0 & 0 & 0 & -1 \end{pmatrix} \tag{2.3}$$

The CGC assumes infinite momentum, or equivalently, that the nuclei are travelling at the speed of light. For a particle moving at the speed of light in the positive z-direction $x^+ = \frac{ct+z}{\sqrt{2}} = \frac{ct+v_z t}{\sqrt{2}} = \frac{ct+ct}{\sqrt{2}} = \sqrt{2}ct$, and thus x^+ acts like the time variable in this coordinate system and scenario. Note that the factor of c is included for clarity.

The conjugate momenta to $x^\pm$ is $p^\mp$ and thus one can apply the uncertainty principle to a high energy nucleus using these conjugate variables. Doing so for x^-, and p^+, the longitudinal extent of a constituent parton with momentum $p^+_{parton} = xP^+_N$, is

$$\Delta x^- \sim \frac{1}{p^+_{parton}} = \frac{1}{xP^+_N} \tag{2.4}$$

where x is the parton momentum fraction and P_N is the momentum of a nucleon. Compare this to the longitudinal extent of the nucleus itself

$$\Delta x^-_A \sim \frac{2R_A}{\gamma} \sim \frac{2R_A m_N}{P^+_N} \tag{2.5}$$

where A labels a nucleus of mass number A, and the γ-factor for the nucleus is approximated by that of one of the nucleons of which it is comprised. It is clear that there is a separation of scales between the hard valence partons that carry most of the momentum, $x \sim 1$, and source the soft gluons for which $x \ll 1$,

$$x^-_{soft} \gg x^-_A \gg x^-_{hard} \tag{2.6}$$

This means that soft gluons are delocalized over a large longitudinal extent, while the valence partons are highly localized on the x^- axis. A similar analysis using x^+ and p^- shows that the valence partons are time-dilated compared to the small x partons,

$$\Delta x^+ \sim \frac{1}{p^-_{parton}} = \frac{2p^+_{parton}}{p^{\perp 2}_{parton}} = \frac{2xP^+_N}{p^{\perp 2}_{parton}} \tag{2.7}$$

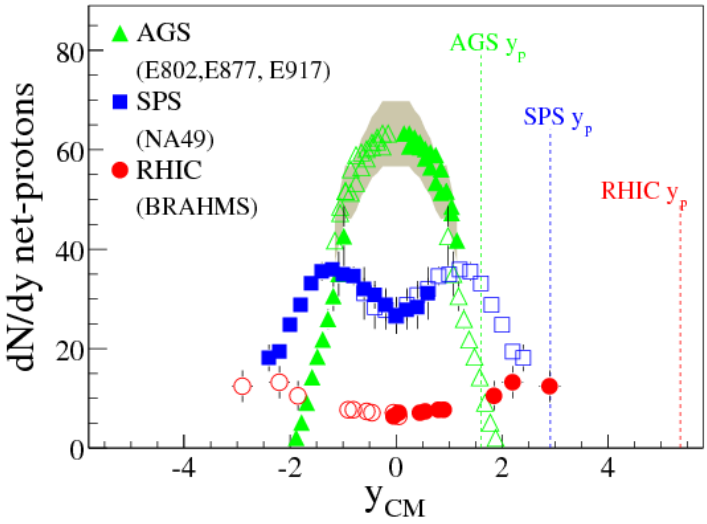

Figure 2.1: Net-proton multiplicity plotted as a function of the center of matter rapidity y_{CM} for different experiments. Plot taken from [14].

To see this, recall $p^+p^- = \frac{E^2-(p^z)^2}{2} = \frac{m^2+p_\perp^2}{2} \approx \frac{p_\perp^2}{2}$, in the high energy limit where it is reasonable to neglect the mass. The important feature of Eq. (2.7) is that $\Delta x^+ \propto x$, clearly indicating that the large x partons are more time dilated. In this sense, the large x partons appear frozen, and thus can be treated as static source terms on the light-cone.

To summarize, the hard partons which carry a large fraction of the overall momentum of the hadron with which they associated, are highly localized on the x^+ axis, and are effectively "frozen" due to time dilation. Furthermore, the fact that the hard partons have far higher momentum than the soft partons means that the radiation of soft gluons can be assumed not to affect the momentum of the hard partons, i.e. that they are recoil-less after radiation. These features will justify the treatment of the hard partons in the next section as δ-function source terms on the light-cone

$$J_a^\nu = \rho_a(\mathbf{x}_\perp)\delta^{\nu+}\delta(x^-) \tag{2.8}$$

where $\rho_a(\mathbf{x}_\perp)$ is a random, static surface charge density. This is effectively a line charge in light-cone coordinates that is coincident with x^+-axis, a fact that will lead to simplifications in the resulting gauge fields.

Treating the valence quarks as recoil-less source terms that propagate on the light-cone

axes removes them from the dynamics of the forward light-cone, where the post collision evolution takes place. For finite momentum nuclei, this will not be strictly true, but the hard partons will still be more likely to end up at higher rapidities, meaning that they can be assumed absent near mid-rapidity. This is supported by Fig. (2.1), which shows that the net baryon number, which is carried entirely by the valence quarks of the nuclei, is measured at increasingly high rapidities as the beam rapidity increases.

Outside of the source term, the CGC action does not have any quarks, either valence or sea, meaning that the high energy hadrons are purely gluonic in this theory. How can this be justified?

One returns again to DIS data. DIS, as mentioned, probes the fine structure of hardons, and it is possible to fit DIS data to construct parton distribution functions (PDFs). PDFs typically plot $xf_i(x)$ where x is the momentum fraction and $f_i(x)$ is the probability of finding parton species i at momentum fraction x, when the hadron is probed at some fixed scale Q^2. Thus, the product $xf_i(x)$ can be interpreted as the momentum density of species i. The function $f_i(x)$ must be true to the quantum numbers of the hadron. To make this concrete [53], a proton is composed of uud quarks, meaning that the total number of up and down quarks must conform to

$$\int_0^1 dx[f_u(x) - f_{\bar{u}}(x)] = 2 \qquad \int_0^1 dx[f_d(x) - f_{\bar{d}}(x)] = 1. \tag{2.9}$$

Similarly the sum of momentum fractions of all of the parton species in the proton must equal one,

$$\int_0^1 dx x[f_u(x) + f_{\bar{u}}(x) + f_d(x) + f_{\bar{d}}(x) + f_g(x)] = 1, \tag{2.10}$$

in order to satisfy momentum conservation. Now, consider Fig. (2.2), a proton PDF. At small momentum fraction, the proton is overwhelmingly dominated by gluons. In fact, even Fig. (2.2) has scaled the gluon distribution, denoted as xg down by a factor of 20 compared to those of the up and down quarks. Recall from the introduction, that the ratio of the electron-neutron to the electron-proton cross section below $x \approx 0.1$ was unity, meaning that protons and neutrons "look" the same for these values of x and can thus both be described by the same PDF, as is done in this thesis. To estimate the value of x probed at the LHC

at 2.76 TeV,

$$x \sim \frac{\langle p_T \rangle}{\sqrt{s}/2} \sim \left. \frac{(0.413 - 0.0171 \ln(s) + 0.00143(\ln(s))^2)\ \text{GeV}}{\sqrt{s}/2\,\text{GeV}} \right|_{\sqrt{s}=2760\,\text{GeV}} \approx 10^{-4} \qquad (2.11)$$

where we have used the fit for $\langle p_T \rangle$ from [55]. Using this as the typical momentum fraction probed at 2.76 TeV, it is clear from the PDF in Fig. (2.2) that the system can be safely approximated as purely gluonic.

The increasing gluon density at small-x can be understood in terms of gluon radiation via brehmsstralung. The hard partons will radiate gluons which will in turn radiate more gluons. This process will lead to a cascade of gluons and an increase in the gluon density. This is shown schematically in Fig. (2.3), with one gluon recombination process circled in red.

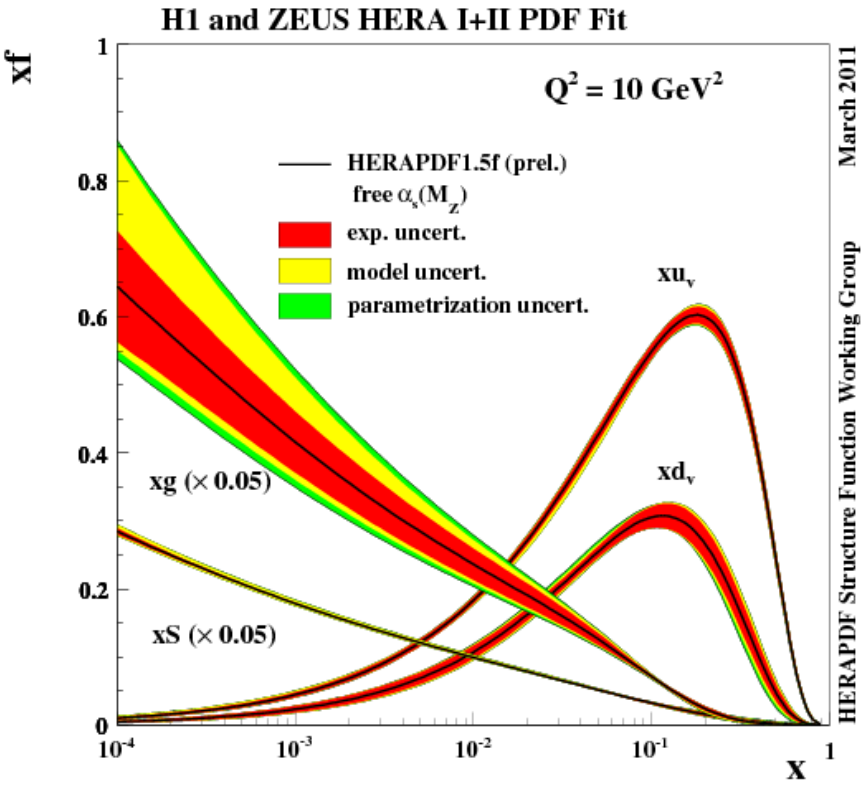

Figure 2.2: Parton distribution function (PDF) for $Q^2 = 10\,\text{GeV}^2$ from [54]. Note that the gluon PDF, labeled xg, is multiplied by 0.05 in this figure, and dominates at low x. This justifies the treatment of the early time dynamics of HIC's as purely gluonic.

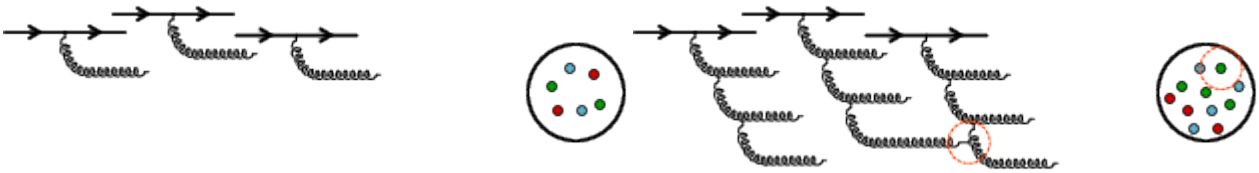

Figure 2.3: Left: A schematic drawing of gluon radiation in the dilute regime. Right: Gluon cascade and recombination. Figs. taken from [56].

As the gluon density grows, gluon recombination will become increasing likely, simply due to the increased packing of gluons in phase space, and will eventually compete with gluon radiation. When gluon recombination balances gluon radiation, the gluon density ceases growing. This proposed phenomenon is known as *gluon saturation* and the energy-scale at which it occurs is known as the *saturation scale*. Gluon saturation has not been observed directly, but saturation inspired calculations have been highly successful. Direct evidence of gluon saturation is a key goal of future measurements at the Electron-Ion Collider [32], which is set to be developed at Brookhaven National Lab (BNL).

Saturation effects should become important when the product of the gluon surface density and the probability for gluon recombination is comparable to one,

$$\frac{(\#\text{ of gluons})}{\text{transverse size of nucleus}} \times \sigma_{gg\to g} \approx \frac{xg(x,Q^2)}{\pi R^2} \times \frac{\alpha_S}{Q^2} \approx 1 \tag{2.12}$$

where $xg(x,Q^2)$ is the gluon density of the hadron at a given x when probed at the scale Q^2. The gluon-gluon recombination cross section is taken to be $\sigma_{gg\to g} = \frac{\alpha_s}{Q^2}$. This can be rearranged for the scale,

$$Q_s^2 \approx \frac{\alpha_s xg(x,Q)}{\pi R^2}. \tag{2.13}$$

For nuclei, one can use the radius of the nucleus R_A, and consider the gluon contribution from the A nucleons,

$$Q_s^2 \approx \frac{A(\alpha_s xg(x,Q))}{\pi R_A^2} \approx A^{1/3}\alpha_s xg(x,Q) \sim A^{1/3}x^{-\lambda} \tag{2.14}$$

where the relationship $R_A \propto A^{1/3}$ was used. One can think about the A dependence arising from the superposition of small-x gluon fields of the individual nucleons.

At the LHC, the saturation scale is believed to be around 2 GeV. In the IP-Glasma model, the saturation scale is determined via the IP-SAT model [44], to be discussed further in chapter 2.2.

Now that the CGC has been outlined, it is worth taking a moment to consider the name of the theory, which is itself indicative of the physics, and can serve as a brief summary. *Colour* refers to the QCD colour charge. Regular glass is a liquid on long time scales and a solid on short time scales and the molecules are disordered. *Glass*, in this instance, refers to the stochastic nature of the colour charge representing the disorder and the scale separation between slow and fast partons that lead to the hard parton sources appearing static to the soft partons. *Condensate* refers to the high density of gluons that act coherently, like a Bose condensate.

2.2 IP-Sat

IP-Sat [44] is a model for determining the saturation scale in the dipole picture of Deep Inelastic Scattering, in which a virtual photon fluctuates into a quark anti-quark pair, and scatters elastically off of a proton, before finally recombining into a virtual photon. The IP-Sat model is designed to model this interaction including the proposed saturation effects that are believed to occur in hadrons at sufficiently high energies. It uses DIS data to constrain the small-x gluonic structure of the nucleons involved in heavy-ion collisions. By independently constraining the parameters of the model with DIS data, the model has very few parameters than can be tuned to heavy ion data.

As discussed in the previous section, the saturation scale can be estimated as the scale at which the product of the gluon density and the gluon recombination cross section exceed unity. The IP-Sat model makes a more detailed, and impact parameter dependent, estimation by considering a $q\bar{q}$ dipole passing through a dense cloud of gluons, where the density cloud of gluons represents the high-energy hadron. The cross section for a $q\bar{q}$ pair to interact with a cloud of gluons is proportional to the area of the dipole (πr^2), the strong coupling constant ($\alpha_s(\mu^2)$), and the gluon momentum density in the cloud ($\frac{xg(x,\mu^2)}{N_c}$). Here μ is the energy scale of the interaction and $xg(x,\mu^2)$ is the density of gluons at this scale, the

quantity shown in Fig. (2.2). This results in the following cross section,

$$\sigma_{q\hat{q}} = \frac{\pi^2}{N_C} r^2 \alpha_s(\mu^2) x g(x, \mu^2). \tag{2.15}$$

If the $q\hat{q}$ pair passes through a dense cloud of gluons that extends in the z-direction, the probability that the dipole does not undergo an inelastic scattering at a given impact parameter within an interval dz is given by,

$$P(b, z) = 1 - \sigma_{q\bar{q}} \rho(b, z) dz \tag{2.16}$$

where the density is normalized via $\int d^2b dz \rho(b, z) dz = 1$. The probability for no inelastic scattering in the entire longitudinal extent in z is given by the product of probabilities for individual dz intervals, and can be identified as the squared magnitude of the scattering matrix $S(b)$,

$$\begin{aligned} |S(b)|^2 &= \prod (1 - \sigma_{q\bar{q}} \rho(b, z) dz) = (1 - \sigma_{q\bar{q}} \rho_1 dz_1)(1 - \sigma_{q\bar{q}} \rho_2 dz_2)(1 - \sigma_{q\bar{q}} \rho_3 dz_3)... \\ &= 1 - \sigma_{q\bar{q}} (\rho_1 dz_1 + \rho_2 dz_2 + ...) + \sigma_{q\bar{q}}^2 (\rho_1 dz_1 \rho_2 dz_2 + ...) - ... \\ &= 1 - \sigma_{q\bar{q}} \int \rho(b, z) dz + \frac{1}{2!} \sigma_{q\bar{q}}^2 \Big(\int \rho(b, z) dz \Big)^2 + ... \\ &= \exp\Big(- \sigma_{q\bar{q}} \int \rho(b, z) dz \Big) \\ &= \exp\Big(- \sigma_{q\bar{q}} T(b) \Big) \end{aligned} \tag{2.17}$$

where the last equality is simply due to the definition of $T(b)$ in terms of ρ. The thickness function $T(b)$ is taken to be gaussian in b

$$T(b) = \frac{1}{2\pi B_G} e^{-b^2/2B_G} \tag{2.18}$$

where $B_G = 4\,\mathrm{GeV}^2$ is one of the parameters fit to DIS data. The cross-section for inelastic scattering as a function of impact parameter b, is given by the Glauber-Mueller dipole cross-section,

$$\begin{aligned} \frac{d\sigma_{q\bar{q}}}{d^2b} &= 2[1 - \mathrm{Re}(S(b))] = 2[1 - \exp(-\sigma_{q\bar{q}} T(b)/2)] \\ &= 2\Big[1 - \exp\Big(\frac{-\pi^2}{2N_C} r^2 \alpha_s(\mu^2) x g(x, \mu^2) T(b)\Big)\Big]. \end{aligned} \tag{2.19}$$

For low gluon densities, the argument of the exponent and thus the interaction probability will tend to be small, meaning the differential cross section will be small. As the gluon

density increases, so too does the interaction probability. The differential cross section does not increase without bound, however, but rather plateaus, when the argument of the exponent becomes large.

To define a saturation scale, it is useful to rewrite Eq. (2.19) slightly, in terms of a density profile,

$$D(b,x,r^2) = \frac{2\pi^2}{N_c}\alpha_s(\mu^2(r^2))xg(x,\mu^2(r^2))T(b) \tag{2.20}$$

The saturation scale is then defined as the dipole size r_s, for which the proton size is one interaction length,

$$S^2 = \exp\left(\frac{-D(b,x,r^2)r_s^2}{2}\right) = e^{-1} \tag{2.21}$$

or equivalently,

$$Q_s^2(b,x) = D(b,x,r_s^2) = \frac{2}{r_s^2}. \tag{2.22}$$

This is the definition of the saturation scale in the IP-Sat model. To find $Q_s^2(b,x)$, typically one solves for r_s^2 via,

$$\frac{\pi^2}{N_c}\alpha_s(\mu^2(r_s^2))xg(x,\mu^2(r_s^2))T(b)r_s^2 = 1 \tag{2.23}$$

In this calculation the leading order expression for the strong coupling is used,

$$\alpha_s(\mu^2) = \frac{12\pi}{(33-2N_f)\ln\left(\frac{\mu^2}{\Lambda_{QCD}^2}\right)} \tag{2.24}$$

where N_f is the number of quark flavors. In the boost invariant case, the momentum fraction x is taken to be

$$x = \frac{Q_s}{\sqrt{s}/2} \tag{2.25}$$

This means that x depends on Q_s and Q_s depends on x, so the system must be solved iteratively until convergence is reached. The iterative procedure is initialized with $x = \frac{\langle p_T(\sqrt{s})\rangle}{\sqrt{s}/2}$, where the numerator is usually taken from an experimental fit, such as the one in Eq. (2.11).

Remember that this is a model for saturation in the $q\bar{q}$ dipole interaction with a a proton. In order to get the saturation scale for the nucleus one needs to sum the contributions from the nucleons. Here, we do so by summing the individual nucleonic thickness functions to

create a nuclear thickness function,

$$T_{(\text{nucleus})}(\mathbf{x}) = \sum_{i=1}^{A} \frac{1}{2\pi B_G} e^{((\mathbf{x}-\mathbf{x_i})^2/2B_G)} \tag{2.26}$$

where x_i represents the positions of the center of the i^{th} nucleon in the transverse plane. Thus, if nucleons are stacked on top of each other, at similar values of x^i, the nuclear thickness function will tend to be denser, and the saturation scale will be higher.

Once Q_s^2 is determined, the color charge is sample from a gaussian whose width is proportional to Q_s^2,

$$\langle \rho^a_{A(B)}(\mathbf{x}_\perp)\rho^b_{A(B)}(\mathbf{y}_\perp)\rangle = g^2\mu^2_{A(B)}(x,\mathbf{x}_\perp)\delta^{ab}\delta^2(\mathbf{x}_\perp - \mathbf{y}_\perp) \tag{2.27}$$

where $Q_s = Cg^2\mu$, and C is a constant. This constant of proportionality is used phenomenologically to control the energy normalization of the system. It is typically taken in 2D to be in the range $C \approx 0.5 - 0.75$. In 3D, due to the extra energy content of the initial transverse fields, it is necessary to change this factor to adjust the energy such that the final state hadronic multiplicity agrees with data. The value used here is $C = 1.42$.

2.3 Gluon Density

The gluon density is needed in order to determine the saturation scale. The gluon density is initialized at an initial scale μ_0^2 according to the following parametrization,

$$xg(x,\mu_0^2) = A_g x^{\lambda_g}(1-x)^{5.6} \tag{2.28}$$

where the scale μ^2 is related to the dipole size via

$$\mu^2 = \frac{C}{r^2} + \mu_0^2. \tag{2.29}$$

The parameters that appear in these equations ($N_f = 4$, $C = 4$, $\mu_0^2 = 1.51\,\text{GeV}^2$, $A_g = 2.308$, $\lambda_g = 0.058$) [57] are fit to DIS scattering data. This is important because for the purposes of the heavy ion calculations done in this thesis, they are fixed.

Once $xg(x,\mu_0^2)$ is initialized with Eq. (2.28), it is evolved to all other values μ^2 via the leading order DGLAP (Dokshitzer-Gribov-Lipatov-Altarelli-Parisi) [58, 59, 60] evolution

equation without quarks as done in the original IP-Glasma papers [1],

$$\frac{\partial x g(x,\mu^2)}{\partial \log(\mu^2)} = \frac{\alpha_s(\mu^2)}{2\pi}\int_x^1 dz P_{gg}(z)\frac{x}{z}g\left(\frac{x}{z},\mu^2\right) \tag{2.30}$$

where the gluon splitting function is given by,

$$P_{gg}(z) = 6\left[\frac{z}{(1-z)^+} + \frac{1-z}{z} + z(1-z)\right] + \left(\frac{11}{2} - \frac{N_f}{3}\right)\delta(1-z). \tag{2.31}$$

Practically speaking, a table of values for $xg(x,\mu^2)$, x, and μ^2 is generated that can be accessed and interpolated by the numerical software as needed.

2.4 One Nucleus (Gauge Fields)

In this section, we discuss the pre-collision gauge fields of nuclei travelling at the speed of light in the CGC framework. This was originally done in [29, 61] but we follow the discussions of [62, 63] more closely. The equations that arise from the CGC action, Eq. (2.1) are the Classical Yang-Mills (CYM) equations

$$[D_\mu, F^{\mu\nu}] = J^\nu = \rho(\mathbf{x}_\perp)\delta^{\nu+}\delta(x^-). \tag{2.32}$$

where the nucleus has been chosen to be right-moving.

Choosing axial gauge, $\tilde{A}^- = \tilde{A}_+ = 0$, where all quantities in this gauge will be written with a tilde, is convenient because in this gauge the charge density is static. To see why, take the covariant continuity equation,

$$\begin{aligned}[\tilde{D}_\mu, \tilde{J}^\mu] &= \partial_\mu \tilde{J}^\mu - ig[\tilde{A}_\mu, \tilde{J}^\mu] = \partial_+ \tilde{J}^+ - ig[\tilde{A}_+, \tilde{J}^+] \\ &= \partial_+ \tilde{\rho} = 0\end{aligned} \tag{2.33}$$

where the commutator term vanishes due to the gauge choice. Recall that we are using the $D_\mu = \partial_\mu - igA_\mu$ convention in this chapter in order to be consistent with the literature. The charge density is static (independent of x^+), and so it is natural to look for a solution that is also static, $\tilde{A}^\mu(x^-, \mathbf{x}_\perp)$. Doing so, the field strength component $\tilde{F}_{+\mu} = 0$ because our gauge choice sets $\tilde{A}_+ = 0$ and the derivatives in ∂_+ vanish due to our choice of a static ansatz.

The only non-vanishing components of the field strength tensor are $\tilde{F}_{i-} = -\tilde{F}^{i+}$ and $\tilde{F}^{ij}$. The equation $[\tilde{D}_i, \tilde{F}^{i-}] + [\tilde{D}_+, \tilde{F}^{+-}] = 0$ is trivial. The transverse equations,

$$[\tilde{D}_i, \tilde{F}^{ij}] = 0 \tag{2.34}$$

are solved by $\tilde{F}^{ij} = 0$ which means that the transverse gauge fields are pure gauge, and can be set to zero. The last remaining YM equation is the only non-trivial one,

$$[\tilde{D}_i, \tilde{F}^{i+}] = [\tilde{D}_i, (\partial^i \tilde{A}^+ - \partial^+ \tilde{A}^i - ig[\tilde{A}^i, \tilde{A}^+])] = \partial_i \partial^i \tilde{A}^+ = -\nabla_\perp^2 \tilde{A}^+ = -\nabla_\perp^2 \tilde{A}_- = \tilde{\rho}(\mathbf{x}_\perp)\delta(x^-). \tag{2.35}$$

This is simply the 2-dimensional Poisson equation. Numerical details for the solution to the Poisson equation can be found in Section 8.1.

Light-cone gauge ($A^+ = 0$) is the most physical gauge for a system with the source term in the x^+ direction. To transform to light-cone gauge, recall the general form of the gauge transform

$$A_\mu = \frac{i}{g} V \partial_\mu V^\dagger + V \tilde{A}_\mu V^\dagger. \tag{2.36}$$

which only has one non-trivial component

$$A_- = \frac{i}{g} V \partial_- V^\dagger + V \tilde{A}_- V^\dagger. \tag{2.37}$$

Setting this to zero to impose the light-cone gauge ($A^+ = A_- = 0$) results in a solution of the form

$$V^\dagger(x^-, \mathbf{x}_\perp) = P \exp\left\{ ig \int_{-\infty}^{x^-} dy^- \tilde{A}_-(y^-, \mathbf{x}_\perp) \right\}. \tag{2.38}$$

Combining Eqs. (2.38) and (2.35), the Wilson line can be written in terms of the covariant charge density, as follows.

$$V^\dagger(x^-, \mathbf{x}_\perp) = P \exp\left\{ ig \int_{-\infty}^{x^-} dy^- \tilde{A}_-(y^-, \mathbf{x}_\perp) \right\} = P \exp\left\{ ig \int_{-\infty}^{x^-} dy^- \frac{\tilde{\rho}(y^-, \mathbf{x}_\perp)}{\nabla_\perp^2} \right\} \tag{2.39}$$

This last gauge transformation leaves $A^- = 0$

$$A^- = A_+ = \frac{i}{g} V \partial_+ V^\dagger + V \tilde{A}_+ V^\dagger = 0 \tag{2.40}$$

because $\tilde{A^-} = \tilde{A}_+ = 0$ and $V^\dagger$ is independent of x^+. Only the transverse gauge fields are non-zero, and they are pure gauge

$$A_i = \frac{i}{g} V \partial_i V^\dagger \tag{2.41}$$

where $V^\dagger$ has been specified above. What remains to be determined for the individual nuclei is the color charge ρ. The color charge cannot be known on an event-by-event basis but

rather is taken to be a stochastic variable that fluctuates event to event as well as locally in the transverse plane within a given nucleus. The fluctuations are taken to be Gaussian, according to the McLerran-Venugopalan (MV) [64, 61, 65] model,

$$W[\tilde{\rho}] = \exp\Big\{ -\int dx^- d^2\mathbf{x}_\perp \frac{\tilde{\rho}_a(x^-,\mathbf{x}_\perp)\tilde{\rho}^a(x^-,\mathbf{x}_\perp)}{2\mu^2(x^-)} \Big\}. \tag{2.42}$$

where μ^2 is the squared surface color charge density carried by the hard partons. From this, ensemble averages of observables can be computed via,

$$\langle \mathcal{O} \rangle = \int [\delta\tilde{\rho}] W[\tilde{\rho}] \mathcal{O}[\tilde{\rho}]. \tag{2.43}$$

2.4.1 Putting one nucleus on the Lattice

The equations outlined in the previous section, namely the 2D pure gauge fields in Eq. (2.41), will need to be put on a lattice for numerical implementation. In practice, the equation for the Wilson line, Eq. (2.39), is constructed numerically as [66]

$$V(\mathbf{x}) = \prod_{i=1}^{N_y} \exp\left(-ig \frac{\rho_k^a(\mathbf{x}) t^a}{\nabla^2 - m^2} \right). \tag{2.44}$$

The stochastic surface charge density $\rho_k^a(\mathbf{x})$ is sampled according to

$$\langle \rho_k^a(\mathbf{x}_\perp) \rho_l^b(\mathbf{y}_\perp) \rangle = \delta^{ab}\delta^{kl}\delta^2(\mathbf{x}_\perp - \mathbf{y}_\perp) \frac{g^2\mu^2(\mathbf{x}_\perp)}{N_y} \tag{2.45}$$

where $k, l = 1, ..., N_y$ label the discretized longitudinal coordinate. In the continuum limit, where $N_y \to \infty$, this becomes the path ordered Wilson line.

The degrees of freedom on the lattice are the gauge links, defined at position x in the i-direction as,

$$U_i(x) = e^{-igaA_i(x)} \tag{2.46}$$

where a is an infinitesimal length element in the i direction, representing the lattice spacing. The gauge links will be discussed in more detail in Section 8.3. One can construct the pure gauge fields on the lattice by plugging Eq. (2.41) into Eq. (2.46). Doing so, and expanding

the exponential to first order yields,

$$\begin{aligned} U_i(x) = e^{-igaA_i(x)} &= e^{-iga(\frac{i}{g}V\partial_i V^\dagger)} \\ &\approx 1 + aV(x)\partial_i V^\dagger(x) \\ &\approx 1 + aV(x)\Big(\frac{V^\dagger(x+a) - V^\dagger(x)}{a}\Big) \\ &\approx V(x)V^\dagger(x+a), \end{aligned} \tag{2.47}$$

a relatively simple numerical formula. This quantity is constructed at each spatial position for both nuclei, A and B. In the next section, the procedure for combining the two pre-collision gauge fields to form the post collision field will be outlined.

2.5 Two Nuclei

In the case of two colliding nuclei, the single nucleus solution is still valid for the individual nuclei in regions (I) and (II) of Fig. (2.4), outside of causal contact with the collision. It remains to determine the form of the gauge fields in the forward light-cone.

To summarize the situation, the source terms are

$$J^\mu = \delta^{\mu+}\delta(x^-)\rho_A(\mathbf{x}_\perp) + \delta^{\mu-}\delta(x^+)\rho_B(\mathbf{x}_\perp). \tag{2.48}$$

and the solution from the previous section for regions (I) and (II) is [29],

$$\begin{aligned} A^+ &= 0 \\ A^- &= 0 \\ A^i &= \Theta(x^-)\Theta(-x^+)\alpha_1^i(\mathbf{x}_\perp) + \Theta(x^+)\Theta(-x^-)\alpha_2^i(\mathbf{x}_\perp) \end{aligned} \tag{2.49}$$

where the subscripts $1, 2$ label the regions of Fig. (2.4) for consistently with the literature. Eq. (2.49) is a static solution to the initial gauge fields for the two pre-collision nuclei. As described in [29], this can be understood physically as two nuclei approaching each other with zero gauge field in front of them, and pure gauge behind them. Since the nuclei have different charge densities, the pure gauge fields that follows them will be different. Also note that the solutions in these regions are time independent, meaning that the fields are frozen and only the center of mass of the nuclei propagates.

The source terms are confined to the light-cone which means that the fields satisfy the sourceless Yang-Mills equations everywhere else, including the forward light-cone,

$$[D_\mu, F^{\mu\nu}] = 0 \tag{2.50}$$

We take the ansatz

$$\begin{aligned} A^+ &= x^+\alpha(\tau, x_\perp) \\ A^- &= x^-\beta(\tau, x_\perp) \\ A^i &= \alpha_3^i(\tau, x_\perp) \end{aligned} \tag{2.51}$$

which is explicitly independent of the spacetime rapidity η. The forms of A^+ and A^- are taken to ensure that the gauge fields transform properly under longitudinal boosts. Making the gauge choice $x^+A^- + x^-A^+ = 0$ fixes $\beta(\tau, x_\perp) = -\alpha(\tau, x_\perp)$. Converting to $\tau - \eta$ coordinates with this ansatz gives the following form for the field strength tensor,

$$\begin{aligned} F^{+-} &= -\frac{1}{\tau}\partial_\tau\tau^2\alpha \\ F^{ij} &= \partial^i\alpha_3^j - \partial^j\alpha_3^i - ig[\alpha_3^i, \alpha_3^j] \\ F^{i\pm} &= -x^\pm\left(\frac{1}{\tau}\partial_\tau\alpha_3^i \mp [D^i, \alpha]\right) \end{aligned} \tag{2.52}$$

where i and j refer only to the transverse directions here and in the following discussion. Plugging these expressions into the equations of motion yields the boost invariant equations,

$$\begin{aligned} \frac{1}{\tau^3}\partial_\tau\tau^3\partial_\tau\alpha - \Big[D^i, [D^i, \alpha]\Big] &= 0 \\ \frac{1}{\tau}\Big[D^i, \partial_\tau\alpha_3^i\Big] + ig\tau[\alpha, \partial_\tau\alpha] &= 0 \\ \frac{1}{\tau}\partial_\tau\tau\partial_\tau\alpha_3^i - ig\tau^2\Big[\alpha, [D^i, \alpha]\Big] - [D^j, F^{ji}] &= 0 \end{aligned} \tag{2.53}$$

These equations are satisfied in regions (I), (II), and (III), but to ensure that the fields are continous on the boundary, one must match the fields between the regions, including the δ-function source terms. After matching on the boundary, the equation $[D_\mu, F^{\mu i}] = 0$ requires

$$\alpha_3^i(\tau = 0, x_\perp) = \alpha_1^i(x_\perp) + \alpha_2^i(x_\perp) \tag{2.54}$$

which is simply the relationship between the transverse gauge field in the forward light cone, to that in the two pre-collision nuclei, A and B,

$$A^i = A^i_{(A)} + A^i_{(B)} \tag{2.55}$$

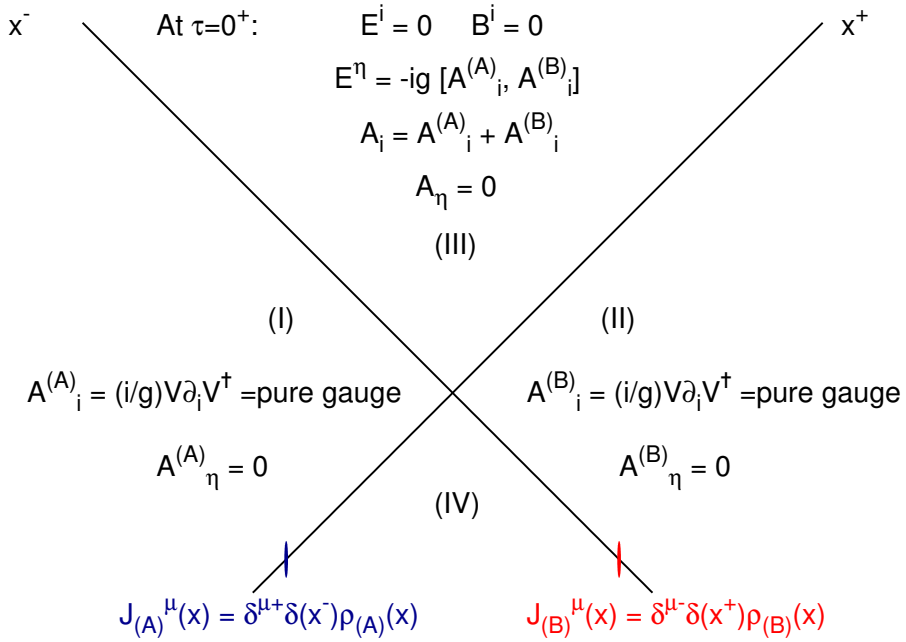

Figure 2.4: Diagram of different regions of space time, and a concise visual summary of the gauge fields in each.

The two equations, $[D_\mu, F^{\mu\pm}] = J^\pm$ both require

$$\alpha(\tau = 0, x_\perp) = \frac{ig}{2}[\alpha_1^i(x_\perp), \alpha_2^i(x_\perp)] \tag{2.56}$$

This can be written as

$$A^+ = x^+\alpha = \frac{ig}{2}x^+[\alpha_1^i, \alpha_2^i] \tag{2.57}$$

This needs to be converted to $\tau - \eta$ coordinates. Recall that

$$\begin{aligned} \tau A^\eta &= \cosh\eta A^z - \sinh\eta A^t \\ A^\tau &= \cosh\eta A^t - \sinh\eta A^z \end{aligned} \tag{2.58}$$

and

$$A^\pm = \frac{A^t \pm A^z}{\sqrt{2}} \tag{2.59}$$

Combining these expressions, one can find

$$\begin{aligned} A^\tau &= \frac{1}{\tau}\left(x^- A^+ + x^+ A^-\right) \\ A^\eta &= \frac{1}{\tau^2}\left(x^- A^+ - x^+ A^-\right) \end{aligned} \tag{2.60}$$

The current gauge means that $A^\tau = 0$ which is the same gauge condition that will be kept for the evolution in the following sections in $\tau - \eta$ coordinates. Putting the form of A^+ and A^- into A^η

$$\begin{aligned} A^\eta &= \frac{1}{\tau^2}\left(x^- A^+ - x^+ A^-\right) \\ &= \frac{1}{\tau^2}\left(x^- x^+ \alpha + x^+ x^- \alpha\right) \\ &= 2x^+ x^- \frac{1}{\tau^2}\left(\frac{ig}{2}[\alpha_1^i, \alpha_2^i]\right) \\ &= \tau^2 \frac{1}{\tau^2}\left(\frac{ig}{2}[\alpha_1^i, \alpha_2^i]\right) \\ &= \frac{ig}{2}[\alpha_1^i, \alpha_2^i] \end{aligned} \tag{2.61}$$

Note that this determines $A^\eta(\tau = 0^+)$, but that the fundamental quantity that is used to define the Wilson line is the lower index quantity,

$$A_\eta = -\tau^2 A^\eta \tag{2.62}$$

which is taken to vanish at $\tau = 0$ in the 2D formulation.

Finally, it is necessary to specify the form of the electric fields to complete the initial condition. In the gauge $A^\tau = 0$, the conjugate momentum to A_η is

$$E^\eta = \frac{1}{\tau}\partial_\tau A_\eta = -\frac{1}{\tau}\partial_\tau(\tau^2 A^\eta) = -(2A^\eta + \tau\partial_\tau A^\eta) \tag{2.63}$$

so at $\tau = 0$,

$$E^\eta = 2A^\eta = -ig[\alpha_1^i, \alpha_2^i] \tag{2.64}$$

Gauss' law can be used to determine the transverse fields,

$$[D_i, E^i] + [D_\eta, E^\eta] = 0. \tag{2.65}$$

In the boost invariant case, all quantities are independent of rapidity, so the second term on the left hand side vanishes, and the equation can be solved simply by $E^i = 0$. A visual summary of the initial condition can be found in Fig. (2.4).

2.5.1 Initial conditions on the lattice

The initial condition for the transverse gauge field in the forward light cone is

$$A^i = A^i_{(A)} + A^i_{(B)} \tag{2.66}$$

This equation needs to be recast in terms of the the gauge link U_i which is the degree of freedom that is evolved on the lattice. Doing so gives [67],

$$\mathrm{Im}\Big[\mathrm{Tr}\, t_a\Big((1+U)(U_A^\dagger + U_B^\dagger)\Big)\Big] = 0 \tag{2.67}$$

where the index representing which transverse component of the gauge field has been suppressed. It is easy to show that this satisfies Eq. (2.66) by expanding the gauge link to first order,

$$\begin{aligned}
&\mathrm{Im}\Big[\mathrm{Tr}\, t_a\Big((1+U)(U_A^\dagger + U_B^\dagger)\Big)\Big] = 0 \\
&\mathrm{Im}\Big[\mathrm{Tr}\, t_a\Big((1+1-igaA)(1+igaA_A+1+igaA_B\Big)\Big] = 0 \\
&\mathrm{Tr}\, t_a\Big(-2A+2A_A+2A_B\Big) = 0 \\
&\tilde{A} - \tilde{A}_{(A)} - \tilde{A}_{(B)} = 0.
\end{aligned} \tag{2.68}$$

This is not a simple equation to solve numerically, and, in fact, corresponds to $N_c^2 - 1 = 8$ equations. The solution that will be outlined below originally comes from [68].To start, we call the functions that need to be zeroed $F_a(\mathbf{x})$

$$F_a(\mathbf{x}) = \ \mathrm{Im}\Big[\mathrm{Tr}\, t_a\Big((1+U)(U_A^\dagger + U_B^\dagger)\Big)\Big] \tag{2.69}$$

and expand each of the 8 functions in a Taylor series around $\mathbf{x}$,

$$F_a(\mathbf{x}+\delta\mathbf{x}) = F_a(\mathbf{x}) + \sum_{b=1}^{N_c^2-1} \frac{\partial F_a}{\partial x_b}\delta x_b + \mathcal{O}(\delta\alpha^2). \tag{2.70}$$

Keeping only up to linear term in $\delta\mathbf{x}$ and setting $F_a(\mathbf{x}+\delta\mathbf{x}) = 0$, one finds a simple relationship

$$F_a(\mathbf{x}) = -\sum_{b=1}^{N_c^2-1} \frac{\partial F_a}{\partial x_b}\delta x_b = -J_{ab}\delta x_b \tag{2.71}$$

Taking the ansatz,

$$U = e^{-ix_b t_b} U_0 \tag{2.72}$$

the Jacobian matrix can be written,

$$\begin{aligned}
J_{ab} &= \frac{\partial}{\partial_{x_b}}\ \mathrm{Im}\Big[\mathrm{Tr}\, t_a\Big((1+U)(U_A^\dagger + U_B^\dagger)\Big)\Big]\Big|_{x_b=0} \\
&= \ \mathrm{Im}\Big[\mathrm{Tr}\, t_a\Big((-it_b e^{-ix_b t_b}U_0)(U_A^\dagger + U_B^\dagger)\Big)\Big]\Big|_{x_b=0} \\
&= \ \mathrm{Re}\Big[\mathrm{Tr}\, t_a t_b\Big(U_0(U_A^\dagger + U_B^\dagger)\Big)\Big]
\end{aligned} \tag{2.73}$$

where we have taken x_b to be zero as an initial guess. Then Eq. (2.71) becomes,

$$\mathrm{Im}\Big[\mathrm{Tr}\, t_a\Big((1+U_0)(U_A^\dagger+U_B^\dagger)\Big)\Big] = -\,\mathrm{Re}\Big[\mathrm{Tr}\, t_a t_b\Big(U_0(U_A^\dagger+U_B^\dagger)\Big)\Big]x_b \tag{2.74}$$

As indicated, x_b is taken to be zero initially, and then this equation is updated by $x_b^{new} = x_b^{prev} + \delta x_b$ and iterated until the equation converges.

2.5.2 Initial E^η on the lattice

Similarly to the initial condition for the transverse gauge fields, it is necessary to formulate the initial condition for $\tilde{E}^\eta$ in terms of lattice quantities. Here, $\tilde{E}^\eta = ga^2E^\eta$ relates the physical quantity (E^η) to the lattice quantity ($\tilde{E}^\eta$). Lattice quantities will be discussed in more detail in the next chapter. Eq. (2.64) takes the form [67] ,

$$\begin{aligned}\tilde{E}^\eta(\mathbf{x}_\perp) = \frac{-i}{4}\sum_{i=1}^{2}\Big[&\Big(U_i(\mathbf{x}_\perp)-1\Big)\Big(U_i^B(\mathbf{x}_\perp)-U_i^A(\mathbf{x}_\perp)\Big)^\dagger \\ &+\Big(U_i(\mathbf{x}_\perp-\mathbf{a_i})-1\Big)^\dagger\Big(U_i^B(\mathbf{x}_\perp-\mathbf{a_i})-U_i^A(\mathbf{x}_\perp-\mathbf{a_i})\Big)-h.c.\Big]\end{aligned} \tag{2.75}$$

where "*h.c.*" means the hermitian conjugate of the expression that is written out explicitly. To show that this indeed solves Eq. (2.64), expand the gauge links to linear order in the gauge fields,

$$\begin{aligned}\tilde{E}^\eta(\mathbf{x}_\perp) &\approx \frac{-ig^2a^2}{4}\sum_{i=1}^{2}\Big[\Big(-iA_i(\mathbf{x}_\perp)\Big)\Big(iA_i^B(\mathbf{x}_\perp)-iA_i^A(\mathbf{x}_\perp)\Big) \\ &\quad+\Big(iA_i(\mathbf{x}_\perp-\mathbf{a_i})\Big)\Big(-iA_i^B(\mathbf{x}_\perp-\mathbf{a_i})+iA_i^A(\mathbf{x}_\perp-\mathbf{a_i})\Big)-h.c.\Big] \\ &\approx \frac{-ig^2a^2}{4}\sum_{i=1}^{2}\Big[\Big(A_i(\mathbf{x}_\perp)\Big)\Big(A_i^B(\mathbf{x}_\perp)-A_i^A(\mathbf{x}_\perp)\Big) \\ &\quad+\Big(A_i(\mathbf{x}_\perp-\mathbf{a_i})\Big)\Big(A_i^B(\mathbf{x}_\perp-\mathbf{a_i})-A_i^A(\mathbf{x}_\perp-\mathbf{a_i})\Big)-h.c.\Big]\end{aligned} \tag{2.76}$$

and substitute $A_i = A_i^A + A_i^B$, to get

$$\begin{aligned}\tilde{E}^\eta(\mathbf{x}_\perp) \approx \frac{-ig^2a^2}{4}\sum_{i=1}^{2}\Big[&\Big(A_i^A(\mathbf{x}_\perp)+A_i^B(\mathbf{x}_\perp)\Big)\Big(A_i^B(\mathbf{x}_\perp)-A_i^A(\mathbf{x}_\perp)\Big) \\ &+\Big(A_i^A(\mathbf{x}_\perp-\mathbf{a_i})+A_i^B(\mathbf{x}_\perp-\mathbf{a_i})\Big)\Big(A_i^B(\mathbf{x}_\perp-\mathbf{a_i})-A_i^A(\mathbf{x}_\perp-\mathbf{a_i})\Big)-h.c.\Big]\end{aligned} \tag{2.77}$$

.

Finally, writing the hermitian conjugate terms explicitly,

$$\begin{aligned}
\tilde{E}^{\eta}(\mathbf{x}_\perp) \approx \frac{-ig^2a^2}{4}\sum_{i=1}^{2}\Big[&\Big(A_i^A(\mathbf{x}_\perp)+A_i^B(\mathbf{x}_\perp)\Big)\Big(A_i^B(\mathbf{x}_\perp)-A_i^A(\mathbf{x}_\perp)\Big)\\
&-\Big(A_i^B(\mathbf{x}_\perp)-A_i^A(\mathbf{x}_\perp)\Big)\Big(A_i^A(\mathbf{x}_\perp)+A_i^B(\mathbf{x}_\perp)\Big)\\
&+\Big(A_i^A(\mathbf{x}_\perp-\mathbf{a_i})+A_i^B(\mathbf{x}_\perp-\mathbf{a_i})\Big)\Big(A_i^B(\mathbf{x}_\perp-\mathbf{a_i})-A_i^A(\mathbf{x}_\perp-\mathbf{a_i})\Big)\\
&-\Big(A_i^B(\mathbf{x}_\perp-\mathbf{a_i})-A_i^A(\mathbf{x}_\perp-\mathbf{a_i})\Big)\Big(A_i^A(\mathbf{x}_\perp-\mathbf{a_i})+A_i^A(\mathbf{x}_\perp-\mathbf{a_i})\Big)\Big]\\
\approx \frac{-iga^2}{4}\sum_{i=1}^{2}\Big[&2A_i^A(\mathbf{x}_\perp)A_i^B(\mathbf{x}_\perp)-2A_i^B(\mathbf{x}_\perp)A_i^A(\mathbf{x}_\perp)\\
&+2A_i^A(\mathbf{x}_\perp-\mathbf{a_i})A_i^B(\mathbf{x}_\perp-\mathbf{a_i})-2A_i^B(\mathbf{x}_\perp-\mathbf{a_i})A_i^A(\mathbf{x}_\perp-\mathbf{a_i})\Big]\\
\approx -ig^2a^2\sum_{i=1}^{2}&[A_i^A,A_i^B]
\end{aligned} \tag{2.78}$$

Recalling the relationship between the lattice quantity and the physical quantity ($\tilde{E}^{\eta} = ga^2E^{\eta}$), this is the equation we wanted to reproduce.

3

Equations of Motion: Classical Yang Mills

3.1 Coordinate System

With the initial conditions for the gauge fields determined, as outlined in section (2.5), it is necessary to formulate the equations of motion in order to determine how the system evolves after the initial collision. First, it is useful to switch coordinates. The derivation of the initial condition is done in light-cone coordinates, but the evolution is carried out in $\tau - \eta$ coordinates, also known as Milne coordinates. First, the definitions are given by,

$$\begin{aligned} \eta &= \frac{1}{2}\ln\left(\frac{t+z}{t-z}\right) = \tanh^{-1}\left(\frac{z}{t}\right) \\ \tau &= \sqrt{t^2 - z^2} \end{aligned} \tag{3.1}$$

and the the metric is $g_{\mu\nu} = \mathrm{diag}(1, -1, -1, -\frac{1}{\tau^2})$. To see why this is the natural coordinate

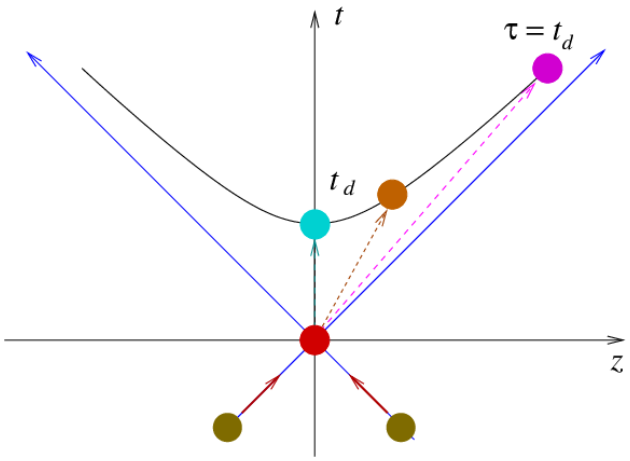

Figure 3.1: Figure from [69].

system, first notice that the forward light-cone, which confines the causal future of the

collision coincides with $\tau = 0$. Similarly, the rapidity, η, is $\pm\infty$ on the light-cone axes and is ill-defined outside this region. Most importantly, τ is the time in the local rest frame of any particle or cell. For a highly relativistic system, like heavy ion collisions at the LHC, two particles with very different longitudinal velocities, such as those pictured in Fig. (3.1), can be at very different points in their respective evolution, but share the same lab time t_d. By using the proper time, τ, the coordinate system tracks every point or particle in their respective rest frames, relative to the collision time. Finally, the longitudinal length element is $\tau d\eta$, meaning the coordinate system expands with time. This better accommodates rapidly expanding physical systems such as those created by heavy ion collisions.

The relevant equations of motion are the classical Yang-Mills (CYM) equations. For a system of strong fields, such as the early stages of heavy ion collisions, quantum corrections are small and can be neglected. This is analogous to electrodynamics, in which Maxwell's equations are adequate in describing systems of strong electromagnetic fields, and QED corrections can be neglected. Although the gauge fields will be treated classically here, quantum corrections have been studied [34] and were found to be important for pressure isotropization.

3.2 Derivation of Equations of Motion

In order to derive the equations of motion, it is useful to begin with the action [33],

$$\begin{aligned} S &= \int d^3x \left(-\frac{1}{4} g^{\alpha\beta} g^{\sigma\rho} F_{\alpha\sigma} F_{\beta\rho} + J_\mu g^{\mu\nu} A_\nu \right) = \int d^3x \left(-\frac{1}{4} F^{\beta\rho} F_{\beta\rho} + J_\mu A^\mu \right) \\ &= -\frac{1}{2} \int \tau d\eta dx dy \Big(F^{\tau\eta} F_{\tau\eta} + F^{\tau i} F_{\tau i} + F^{i\eta} F_{i\eta} + \frac{1}{2} F^{ij} F_{ij} \Big) \\ &= -\frac{1}{2} \int \tau d\eta dx dy \Big(- \frac{F_{\tau\eta}^2}{\tau^2} - F_{\tau i}^2 + \frac{F_{i\eta}^2}{\tau^2} + F_{xy}^2 \Big) \\ &= \int d\eta dx dy \Big\{ \frac{\tau}{2} \Big(\frac{F_{\tau\eta}^2}{\tau^2} + F_{\tau i}^2 - \frac{F_{i\eta}^2}{\tau^2} - F_{xy}^2 \Big) \Big\} \\ &= \int dx dy d\eta \mathcal{L} \end{aligned} \tag{3.2}$$

where we are using the metric $g_{\mu\nu} = \mathrm{diag}(1, -1, -1, -\frac{1}{\tau^2})$. As in 2D, the source terms in the Lagrangian are assumed to be eikonal and propagate along the light-cone axes, meaning that the gluon fields evolve according to the sourceless CYM equations in the forward light

cone, and we can neglect the source term in the Lagrangian in the forward light-cone. The effect of the source term is implemented through the initial gauge fields, as they are derived using δ-function source terms on the light-cone and the JIMWLK evolution, as discussed in sections 2.5 and 4.3, respectively.

In general, in a non-boost invariant system the current is not strictly on the light cone, but has some finite extent within the forward light-cone. This is for two reasons: 1) the nuclei are no-longer infinitely length contracted to δ-functions, and 2) $v_z < c$ which actually means the propagation of the source is no longer parallel to the light-cone axis. If one considers a slightly shifted $\tau - \eta$ coordinate system where τ_0 corresponds to the last instant of contact between the two nuclei, as we do here, then the first issue is no longer a problem. This is because the new coordinate system excludes the region that includes finite extent of the nucleus. To do this, we start the evolution of the fields once the two nuclei have completely passed through one another, at approximately $\tau_0 = 2R/\gamma$, where R is the nuclear radius and γ is the Lorentz factor. For Pb-Pb collisions at the LHC at $\sqrt{s} = 2.76$ TeV , this is roughly

$$\begin{aligned} \gamma &= \frac{\sqrt{s}/2}{m_N} = \frac{2760/2\,\text{GeV}}{0.940\,\text{GeV}} \approx 1500 \\ \tau_0 &= \frac{2R}{\gamma} \approx \frac{13\,\text{fm}}{1500} \approx 0.01\,\text{fm}. \end{aligned} \tag{3.3}$$

The issue of sub-luminal velocity of the source terms is dealt with to some extent by the rapidity dependent source term that is generated by the JIMWLK evolution. As will be discussed in section 4.3, the CGC employs a separation of scales that integrates out high momentum modes and incorporates them into a source term, and the JIMWLK evolution implements this in a rapidity dependent way. This should mean that the color sources in the rapidity range $y_{max}^{IPG} < y < y_{beam}$ should be incorporated in the effective charge density for the gauge fields at y_{max}^{IPG}, where this is the maximum rapidity extent of the IP-Glasma simulation. Any effects from source terms in the forward light-cone beyond this can be assumed to be neglected by this treatment.

Given these clarifications, we will now proceed with the derivation for the classical, source-less Yang-Mills equations of motion in the Hamiltonian formalism in 3+1D. In the typical 2+1D derivation, the longitudinal gauge field is treated as an adjoint scalar ϕ with conjugate momentum π that couples to the 2+1D transverse Yang-Mills fields [70]. This is useful when

evolving a boost invariant system on a 2+1D lattice. However, since the goal here is to evolve in 3+1D dimensions, we will derive the 3+1D Hamiltonian equations of motion here. The essential dynamical features are the same as the 2+1D formulation, given the same initial conditions, but to save time, we only derive the EOM's only once.

In general, the Hamiltonian can be written in terms of the Lagrangian as,

$$\mathcal{H} = \sum_i \dot{q}_i \frac{\partial \mathcal{L}}{\partial \dot{q}_i} - \mathcal{L} = \sum_i \dot{q}_i p_i - \mathcal{L} \tag{3.4}$$

where q_i are the generalized coordinates, which are the gauge fields A_μ in our case. Having chosen the gauge $A^\tau = 0$, it is easy to see that the conjugate momenta are,

$$\frac{\partial \mathcal{L}}{\partial(\partial_\tau A_i)} = \tau \partial_\tau A_i = E^i \tag{3.5}$$

and

$$\frac{\partial \mathcal{L}}{\partial(\partial_\tau A_\eta)} = \frac{1}{\tau}\partial_\tau A_\eta = E^\eta. \tag{3.6}$$

The extra factors of τ that deviate from the Maxwell Equations inspired intuition for these types of equations is due to the $\tau - \eta$ coordinate system. Putting the momentum terms into the Hamiltonian gives,

$$\begin{aligned}
\mathcal{H} &= (\partial_\tau A_i)E^i + (\partial_\tau A_\eta)E^\eta - \mathcal{L} = \frac{(E^i)^2}{\tau} + \tau(E^\eta)^2 - \mathcal{L} \\
&= \frac{(E^i)^2}{\tau} + \tau(E^\eta)^2 - \frac{1}{2}\tau\Big[\frac{F_{\tau\eta}^2}{\tau^2} + F_{\tau i}^2 - \frac{F_{i\eta}^2}{\tau^2} - \frac{F_{ij}^2}{2}\Big] \\
&= \frac{(E^i)^2}{\tau} + \tau(E^\eta)^2 - \frac{1}{2}\tau\Big[\frac{(E^\eta\tau)^2}{\tau^2} + \frac{(E^i)^2}{\tau^2} - \frac{F_{i\eta}^2}{\tau^2} - \frac{F_{ij}^2}{2}\Big] \\
&= \frac{1}{2}\Big[\frac{(E^i)^2}{\tau} + \tau(E^\eta)^2 + \frac{F_{i\eta}^2}{\tau} + \tau F_{xy}^2\Big].
\end{aligned} \tag{3.7}$$

Now that we have the Hamiltonian density, it is possible to write the Hamiltonian equations of motion, which are typically written

$$\frac{\partial \mathcal{H}}{\partial p_i} = \frac{\partial q_i}{\partial \tau}, \qquad \frac{\partial \mathcal{H}}{\partial q_i} = -\frac{\partial p_i}{\partial \tau}. \tag{3.8}$$

In our case,

$$\frac{\partial \mathcal{H}}{\partial E^\mu} = \frac{\partial A_\mu}{\partial \tau}, \qquad \frac{\partial \mathcal{H}}{\partial A_\mu} = -\frac{\partial E^\mu}{\partial \tau} \tag{3.9}$$

where $\mu = x, y, \eta$ for a total of 6 EOM's. The evolution equations for the gauge fields are given by,

$$\frac{\partial A_i}{\partial \tau} = \frac{\partial}{\partial E^i}\Big[\frac{1}{2}\Big(\frac{(E^i)^2}{\tau} + \tau(E^\eta)^2 + \frac{F_{i\eta}^2}{\tau} + \tau F_{xy}^2\Big)\Big] = \frac{1}{\tau}E^i \tag{3.10}$$

and

$$\frac{\partial A_\eta}{\partial \tau} = \frac{\partial}{\partial E^\eta}\Big[\frac{1}{2}\Big(\frac{(E^i)^2}{\tau} + \tau(E^\eta)^2 + \frac{F_{i\eta}^2}{\tau} + \tau F_{xy}^2\Big)\Big] = \tau E^\eta \tag{3.11}$$

The equations for the electric fields are,

$$\begin{aligned} -\frac{\partial E^i}{\partial \tau} &= \frac{\partial \mathcal{H}}{\partial A_i} \\ -\partial_\tau E^i &= \frac{\partial}{\partial A_i}\Big[\frac{1}{2}\Big(\frac{(E^i)^2}{\tau} + \tau(E^\eta)^2 + \frac{F_{i\eta}^2}{\tau} + \tau F_{ij}^2\Big)\Big] \\ &= \frac{1}{2}\frac{\partial}{\partial A_i}\Big[\frac{F_{i\eta}^2}{\tau} + \tau F_{ij}^2\Big] \\ &= \frac{1}{\tau}[D_\eta, F_{i\eta}] + \tau[D_j, F_{ij}] \end{aligned} \tag{3.12}$$

Similarly,

$$\begin{aligned} -\frac{\partial E^\eta}{\partial \tau} &= \frac{\partial \mathcal{H}}{\partial A_\eta} \\ -\partial_\tau E^\eta &= \frac{\partial}{\partial A_\eta}\Big[\frac{1}{2}\Big(\frac{(E^i)^2}{\tau} + \tau(E^\eta)^2 + \frac{F_{i\eta}^2}{\tau} + \tau F_{ij}^2\Big)\Big] \\ &= \frac{1}{2}\frac{\partial}{\partial A_\eta}\Big[\frac{F_{i\eta}^2}{\tau} + \tau F_{ij}^2\Big] \\ &= -\frac{1}{\tau}[D_i, F_{i\eta}] \end{aligned} \tag{3.13}$$

The final form of the EOM's for the electric field is,

$$\begin{aligned} \partial_\tau E^i &= \frac{1}{\tau}[D_\eta, F_{\eta i}] + \tau[D_j, F_{ji}] \\ \partial_\tau E^\eta &= \frac{1}{\tau}[D_i, F_{i\eta}]. \end{aligned} \tag{3.14}$$

where i, j are transverse directions. Finally, the Gauss constraint is given by

$$[D_i, E^i] + [D_\eta, E^\eta] = 0 \tag{3.15}$$

Due to gauge freedom, the equations of motion are not sufficient to determine the gauge fields. Gauss' law does not arise out of the Hamiltonian formulation without adding constraints to the Hamiltonian. For details on this procedure, see chapter (3.2) of [71].

To summarize, the Hamiltonian EOM's, along with Gauss' law, are

$$\begin{aligned}
\partial_\tau E^i &= \frac{1}{\tau}[D_\eta, F_{\eta i}] + \tau[D_j, F_{ji}] \\
\partial_\tau E^\eta &= \frac{1}{\tau}[D_i, F_{i\eta}] \\
\frac{\partial A_i}{\partial \tau} &= \frac{1}{\tau}E^i \\
\frac{\partial A_\eta}{\partial \tau} &= \tau E^\eta \\
0 &= [D_i, E^i] + [D_\eta, E^\eta]
\end{aligned} \tag{3.16}$$

The evolution equations are coupled, so that the gauge fields depend on the electric fields at a given time, and vice versa. In order to solve these equations, a leap-frog algorithm is employed so that the electric field is evaluated at $E(\tau)$ and the gauge fields are evaluated at $A(\tau + d\tau/2)$. In this sense, the fields "leap-frog" over one another in time. At the end of the evolution the electric fields are evolved by an additional $d\tau/2$ to bring them to the same time as the gauge fields.

3.3 Putting it on the Lattice - Preliminaries

In the next section, we will cast the Hamiltonian in terms of lattice quantities and derive the equations of motion that are implemented numerically. Before doing so, it is useful to address some preliminary considerations. First, it is useful for the numerical calculation to re-scale everything with the lattice spacing $a_\perp$ and the coupling constant so that it is not necessary to keep track of these terms in the numerical simulation. Of course, they will be restored at at end of the calculation in order to compute physically relevant quantities. All rescaled quantities will be denoted with a tilde. Rescaling the transverse length scale and the time by the lattice spacing makes them dimensionless, or puts them in what we will call "lattice units",

$$\begin{aligned}
\tilde{\tau} &= \tau/a_\perp \\
\tilde{x^i} &= x^i/a_\perp.
\end{aligned} \tag{3.17}$$

Recall that η is a dimensionless quantity, which means that we cannot determine where factors of a_η belong strictly from dimensional analysis, so we need to keep track of the

factors of a_η. Rescaling the fields themselves gives,

$$\begin{aligned}
\tilde{A}_i &= g a_\perp A_i \\
\tilde{A}_\eta &= g A_\eta \\
\tilde{E}^i &= \tilde{\tau}\tilde{\partial}_\tau \tilde{A}_i = g a_\perp E^i \\
\tilde{E}^\eta &= \frac{1}{\tilde{\tau}}\tilde{\partial}_\tau \tilde{A}_\eta = (g a_\perp^2) E^\eta
\end{aligned} \tag{3.18}$$

The degrees of freedom that are evolved explicitly in time are the electric field and the gauge links, defined as

$$U_i(x_N^i, x_0^i) = \mathcal{P} \exp\Big(- ig \int_{x_0^i}^{x_N^i} dz^i A_i(z^i)\Big) \tag{3.19}$$

with a minus sign in the exponent because we are using the convention $D_\mu = \partial_\mu + igA_\mu$. On the lattice, the gauge link that connects neighboring vertices in the transverse plane at x_i and x_{i+i}, respectively, can be written, for sufficiently small lattice spacing, as

$$U_i(x_k, x_{k+1}) = \mathcal{P} \exp\Big(- ig \int_{x_{k+1}}^{x_k} dz^i A_i(z^i)\Big) \approx \exp\Big(iga_\perp A_i(x_k)\Big) \tag{3.20}$$

where $A(x_k)$ is the gauge field associated with the link that points from vertex x_k to x_{k+1}. The change in sign in the exponent is because the direction of the limits of integration. In this thesis, the gauge link for the x^i direction on the lattice will be defined as going in the positive x^i direction. After rescaling, we have

$$U_i(\tilde{x}_k, \tilde{x}_{k+1}) = \exp\Big(i\tilde{A}_i(x_k)\Big) \tag{3.21}$$

where $i = x, y$ because one needs to keep track of factors of a_η for $\tilde{U}_\eta$,

$$U_\eta(\eta_k, \eta_{k+1}) = \exp\Big(ia_\eta \tilde{A}_\eta(\eta_k)\Big). \tag{3.22}$$

From these last two equations, it is apparent why the rescaling done in Eq. (3.18) is so useful: the factors of $a_\perp$ and g no longer need to be tracked explicitly. One can define the plaquette (see section (8.3)) which is a closed loop of gauge links,

$$U_{ij}(x) = U_i(x) U_J(x + \hat{i}) U_i^\dagger(x + \hat{i} + \hat{j}) U_j^\dagger(x + \hat{j}) \approx \exp\Big(i\tilde{F}ij\Big) \tag{3.23}$$

For numerical precision, the quantities

$$\begin{aligned} DU_i &= U_i - 1 \\ DU_{ij} &= U_{ij} - 1 \end{aligned} \tag{3.24}$$

are used in place of the gauge link and plaquette, respectively. It is easy to construct the squared field strength component F_{ij}^2, which appears in the Hamiltonian, by taking the real part of DU_{ij}

$$\begin{aligned} DU_{ij} &= \Big(\exp\left(i\tilde{F}_{ij}\right) - 1 \Big) \\ &= \Big(1 + i\tilde{F}_{ij}^a t_a - \frac{1}{2}\tilde{F}_{ij}^a \tilde{F}_{ij}^b t_a t_b + \mathcal{O}(a^6) \Big) - 1. \end{aligned} \tag{3.25}$$

Taking the real part of the trace over colors and using $\mathrm{Tr}(t_a t_b) = \frac{1}{2}\delta_{ab}$,

$$\mathcal{R}[\mathrm{Tr}(DU_{ij})] = -\frac{1}{4}\tilde{F}_{ij}^a \tilde{F}_{ij}^a + \mathcal{O}(a^8). \tag{3.26}$$

This means, for sufficiently small lattice spacing, one can take,

$$\tilde{F}_{ij}^2 = -4\mathcal{R}[\mathrm{Tr}(DU_{ij})] \tag{3.27}$$

Without the tilde, this can be written,

$$F_{ij}^2 = \frac{-4}{g^2 a_i^2 a_j^2}\mathcal{R}[\mathrm{Tr}(DU_{ij})]. \tag{3.28}$$

Finally, for the equations of motion, it will be necessary to take derivatives of the gauge links in the Hamiltonian with respect to the gauge fields, which is non-trivial due to the matrix structure of the exponent. We can re-write the gauge link, that goes from lattice site x to site $x + a^i$, at fixed time, as

$$U_i(x) = \exp\left(igA_i(x)h\right) ... \exp\left(igA_i(x + a^i)h\right) \tag{3.29}$$

where h is an infinitesimal length element, and the second line shows the explicit path-ordering. Taking the derivative with respect to the gauge field,

$$\frac{\partial}{\partial A_i^a(\mathbf{x})} U_j(\mathbf{x}) = \frac{\partial}{\partial A_i^a(\mathbf{x})} e^{iga_j t_a A_j^a} = iga_j t_a U_j(\mathbf{x})\delta_{ij} \tag{3.30}$$

yields a color matrix t_a on the left hand side, due to the path ordering. Here a_j is the lattice spacing in the j-direction. More details about lattice gauge theory and numerical details can be found in Section 8.3.

3.4 Lattice Equations of Motion Derivation

Now it is possible to re-write the action, Eq. (3.2), in terms of lattice quantities. First, discretizing the differential volume element that is being integrated over,

$$\begin{aligned} S &= -\frac{1}{2}\int \tau d\eta dx dy \mathrm{Tr}\Big(F^{\tau\eta}F_{\tau\eta} + F^{\tau i}F_{\tau i} + F^{i\eta}F_{i\eta} + \frac{1}{2}F^{ij}F_{ij}\Big) \\ &= \frac{1}{2}\sum \tau a_\eta a_\perp^2 \mathrm{Tr}\Big\{\Big(\frac{F_{\tau\eta}^2}{\tau^2} + F_{\tau i}^2 - \frac{F_{i\eta}^2}{\tau^2} - F_{xy}^2\Big)\Big\} \end{aligned} \tag{3.31}$$

.

Next, replacing the field strength components with the electric field using Eq.'s (3.5), (3.6) and gauge links using Eq. (3.28),

$$\begin{aligned} S &= \frac{1}{2}\sum \tau a_\eta a_\perp^2 \Big\{\Big(\frac{\mathrm{Tr}(\tau E^\eta)^2}{\tau^2} + \frac{\mathrm{Tr}(E^x)^2}{\tau^2} + \frac{\mathrm{Tr}(E^y)^2}{\tau^2} + \frac{4}{g^2 a_x^2 a_\eta^2 \tau^2}\mathcal{R}[\mathrm{Tr}(DU_{x\eta})] \\ &+ \frac{4}{g^2 a_y^2 a_\eta^2 \tau^2}\mathcal{R}[\mathrm{Tr}(DU_{y\eta})] + \frac{4}{g^2 a_x a_y^2}\mathcal{R}[\mathrm{Tr}(DU_{xy})]\Big)\Big\} \\ &= \frac{1}{2}\sum a_\eta a_\perp^2 \Big\{\Big(\mathrm{Tr}\tau(E^\eta)^2 + \frac{\mathrm{Tr}(E^x)^2}{\tau} + \frac{\mathrm{Tr}(E^y)^2}{\tau} + \frac{4}{g^2 a_x^2 a_\eta^2 \tau}\mathcal{R}[\mathrm{Tr}(DU_{x\eta})] \\ &+ \frac{4}{g^2 a_y^2 a_\eta^2 \tau}\mathcal{R}[\mathrm{Tr}(DU_{y\eta})] + \frac{4\tau}{g^2 a_x^2 a_y^2}\mathcal{R}[\mathrm{Tr}(DU_{xy})]\Big)\Big\} \end{aligned} \tag{3.32}$$

We can write this in term of the lattice quantities (with tildes),

$$\begin{aligned} S &= \frac{1}{2}\sum a_\eta a_\perp^2 \Big\{\Big(\mathrm{Tr}\tau(E^\eta)^2 + \frac{\mathrm{Tr}(E^x)^2}{\tau} + \frac{\mathrm{Tr}(E^y)^2}{\tau} + \frac{4}{g^2 a_x^2 a_\eta^2 \tau}\mathcal{R}[\mathrm{Tr}(DU_{x\eta})] \\ &+ \frac{4}{g^2 a_y^2 a_\eta^2 \tau}\mathcal{R}[\mathrm{Tr}(DU_{y\eta})] + \frac{4\tau}{g^2 a_x^2 a_y^2}\mathcal{R}[\mathrm{Tr}(DU_{xy})]\Big)\Big\} \\ &= \frac{1}{2}\sum a_\eta a_\perp^2 \Big\{\Big((\tilde{\tau}a_\perp)\mathrm{Tr}(\frac{\tilde{E}^\eta}{g a_\perp^2})^2 + \mathrm{Tr}(\frac{\tilde{E}^x}{g a_\perp})^2 \frac{1}{a_\perp \tilde{\tau}} + \mathrm{Tr}(\frac{\tilde{E}^y}{g a_\perp})^2 \frac{1}{a_\perp \tilde{\tau}} + \frac{4}{g^2 a_x^2 a_\eta^2 (\tilde{\tau}a_\perp)}\mathcal{R}[\mathrm{Tr}(DU_{x\eta})] \\ &+ \frac{4}{g^2 a_y^2 a_\eta^2 (\tilde{\tau}a_\perp)}\mathcal{R}[\mathrm{Tr}(DU_{y\eta})] + \frac{4(\tilde{\tau}a_\perp)}{g^2 a_x^2 a_y^2}\mathcal{R}[\mathrm{Tr}(DU_{xy})]\Big)\Big\} \\ &= \frac{1}{2}\frac{a_\eta}{a_\perp g^2}\sum \Big\{\Big(\tilde{\tau}\mathrm{Tr}(\tilde{E}^\eta)^2 + \mathrm{Tr}(\tilde{E}^x)^2 \frac{1}{\tilde{\tau}} + \mathrm{Tr}(\tilde{E}^y)^2 \frac{1}{\tilde{\tau}} + \frac{4}{a_\eta^2(\tilde{\tau})}\mathcal{R}[\mathrm{Tr}(DU_{x\eta})] \\ &+ \frac{4}{a_\eta^2(\tilde{\tau})}\mathcal{R}[\mathrm{Tr}(DU_{y\eta})] + 4(\tilde{\tau})\mathcal{R}[\mathrm{Tr}(DU_{xy})]\Big)\Big\}. \end{aligned} \tag{3.33}$$

The lattice action can be written,

$$\tilde{S} = \frac{1}{2}\sum\Big\{\Big(\tilde{\tau}\mathrm{Tr}(\tilde{E}^{\eta})^2 + \mathrm{Tr}(\tilde{E}^{x})^2\frac{1}{\tilde{\tau}} + \mathrm{Tr}(\tilde{E}^{y})^2\frac{1}{\tilde{\tau}} + \frac{4}{a_{\eta}^2(\tilde{\tau})}\mathcal{R}[\mathrm{Tr}(DU_{x\eta})] + \frac{4}{a_{\eta}^2(\tilde{\tau})}\mathcal{R}[\mathrm{Tr}(DU_{y\eta})] + 4(\tilde{\tau})\mathcal{R}[\mathrm{Tr}(DU_{xy})]\Big)\Big\}. \tag{3.34}$$

One can follow a similar procedure as done in the previous section to derive the lattice equations of motion. Going back to the Hamiltonian again and casting in terms of the lattice quantities,

$$\tilde{\mathcal{H}} = \frac{1}{2}\Big[\mathrm{Tr}\frac{(\tilde{E}^{x})^2}{\tilde{\tau}} + \mathrm{Tr}\frac{(\tilde{E}^{y})^2}{\tilde{\tau}} + \tilde{\tau}\mathrm{Tr}(\tilde{E}^{\eta})^2 + \frac{4}{a_{\eta}^2(\tilde{\tau})}\mathcal{R}[\mathrm{Tr}(1-U_{x\eta})] + \frac{4}{a_{\eta}^2(\tilde{\tau})}\mathcal{R}[\mathrm{Tr}(1-U_{y\eta})] + 4(\tilde{\tau})\mathcal{R}[\mathrm{Tr}(1-U_{xy})\Big] \tag{3.35}$$

As before, the Hamiltonian EOM's are

$$\frac{\partial\mathcal{H}}{\partial A_{\mu}} = -\frac{\partial E^{\mu}}{\partial\tau} \tag{3.36}$$

Recall from the previous section, the definition of the the derivative of the transverse gauge link, this times in terms of scaled lattice quantities,

$$\frac{\partial}{\partial\tilde{A}_i^a(\mathbf{x})}U_j(\mathbf{x}) = \frac{\partial}{\partial\tilde{A}_i^a(\mathbf{x})}e^{it_a\tilde{A}_j^a} = it_aU_j(\mathbf{x})\delta_{ij} \tag{3.37}$$

In the action, there is a sum over all the lattice sites. In this sum, there are only two plaquettes in the $x-y$ plane that include the link $A_x(\mathbf{x})$, one starting at position $\mathbf{x}$, the other starting at position $\mathbf{x}-\hat{\mathbf{e}}_{\mathbf{y}}$,

$$U_{xy}(\mathbf{x}) = U_x(\mathbf{x})U_y(\mathbf{x}+\hat{\mathbf{e}}_{\mathbf{x}})U_{-x}(\mathbf{x}+\hat{\mathbf{e}}_{\mathbf{x}}+\hat{\mathbf{e}}_{\mathbf{y}})U_{-y}(\mathbf{x}+\hat{\mathbf{e}}_{\mathbf{y}}) \tag{3.38}$$

and

$$\begin{aligned} U_{xy}(\mathbf{x}-\hat{\mathbf{e}}_{\mathbf{y}}) &= U_x(\mathbf{x}-\hat{\mathbf{e}}_{\mathbf{y}})U_y(\mathbf{x}-\hat{\mathbf{e}}_{\mathbf{y}}+\hat{\mathbf{e}}_{\mathbf{x}})U_{-x}(\mathbf{x}+\hat{\mathbf{e}}_{\mathbf{x}})U_{-y}(\mathbf{x}) \\ &= U_x(\mathbf{x}-\hat{\mathbf{e}}_{\mathbf{y}})U_y(\mathbf{x}-\hat{\mathbf{e}}_{\mathbf{y}}+\hat{\mathbf{e}}_{\mathbf{x}})U_x^{\dagger}(\mathbf{x})U_{-y}(\mathbf{x}). \end{aligned} \tag{3.39}$$

The derivative of the Hamiltonian with respect to the gauge field, then, has two terms,

$$\begin{aligned}\mathrm{Tr}\frac{\partial}{\partial\tilde{A}^a_x(\mathbf{x})}\Big(U_{xy}(\mathbf{x})+U_{xy}(\mathbf{x}-\hat{\mathbf{e}}_\mathbf{y})\Big) &= \mathrm{Tr}\Big(it_aU_x(\mathbf{x})U_y(\mathbf{x}+\hat{\mathbf{e}}_\mathbf{x})U_{-x}(\mathbf{x}+\hat{\mathbf{e}}_\mathbf{x}+\hat{\mathbf{e}}_\mathbf{y})U_{-y}(\mathbf{x}+\hat{\mathbf{e}}_\mathbf{y})\\ &\quad + U_x(\mathbf{x}-\hat{\mathbf{e}}_\mathbf{y})U_y(\mathbf{x}-\hat{\mathbf{e}}_\mathbf{y}+\hat{\mathbf{e}}_\mathbf{x})U^\dagger_x(\mathbf{x})(-it_a)U_{-y}(\mathbf{x})\Big)\\ &= i\mathrm{Tr}\left[t_a\Big(U_{xy}(\mathbf{x})-U_{xy}(\mathbf{x}-\hat{\mathbf{e}}_\mathbf{y})\Big)\right]\\ &= i\mathrm{Tr}\left[t_a\Big(U_{xy}(\mathbf{x})-U_{-yx}(\mathbf{x})\Big)\right].\end{aligned} \tag{3.40}$$

There are also two plaquettes that contains the gauge link $A_x(\mathbf{x})$ in the x-η plane. Following a similar procedure, one ultimately arrives at

$$\mathrm{Tr}\frac{\partial}{\partial\tilde{A}^a_x(\mathbf{x})}\Big(U_{x\eta}(\mathbf{x})+U_{x\eta}(\mathbf{x}-\hat{\mathbf{e}}_\eta)\Big) = i\mathrm{Tr}\left[t_a\Big(U_{x\eta}(\mathbf{x})-U_{-\eta x}(\mathbf{x})\Big)\right]. \tag{3.41}$$

.

Applying this to the relevant terms in the Hamiltonian yields,

$$\begin{aligned}\frac{\partial\tilde{\mathcal{H}}}{\partial\tilde{A}^a_x} &= \frac{\partial}{\partial\tilde{A}^a_x(\mathbf{x})}\Big(-2(\tilde{\tau})\mathcal{R}[\mathrm{Tr}(U_{xy})]-2(\frac{1}{a^2_\eta\tilde{\tau}})\mathcal{R}[\mathrm{Tr}(U_{x\eta})]\Big)\\ &= -2\mathcal{R}\left(i\mathrm{Tr}\Big[t_a[\tilde{\tau}(U_{xy}(\mathbf{x})-U_{-yx}(\mathbf{x}))+\frac{i}{\tilde{\tau}a^2_\eta}(U_{x\eta}(\mathbf{x})-U_{-\eta x}(\mathbf{x}))]\Big]\right)\\ &= 2\mathcal{I}\left(\mathrm{Tr}\Big[t_a[\tilde{\tau}(U_{xy}(\mathbf{x})-U_{-yx}(\mathbf{x}))+\frac{1}{\tilde{\tau}a^2_\eta}(U_{x\eta}(\mathbf{x})-U_{-\eta x}(\mathbf{x}))]\Big]\right).\end{aligned} \tag{3.42}$$

.

Using the fact that $\mathcal{I}(z)=-\frac{i}{2}[z-z^*]$ for a complex number z, and properties of the trace, allows this to be re-written as,

$$\begin{aligned}\frac{\partial\tilde{\mathcal{H}}}{\partial\tilde{A}^a_x} &= -i\mathrm{Tr}\Big(t_a\Big[\tilde{\tau}(U_{xy}(\mathbf{x})-U_{-yx}(\mathbf{x})-U^\dagger_{xy}(\mathbf{x})+U^\dagger_{-yx}(\mathbf{x}))\\ &\quad+\frac{1}{\tilde{\tau}a^2_\eta}(U_{x\eta}(\mathbf{x})-U_{-\eta x}(\mathbf{x})-U^\dagger_{x\eta}(\mathbf{x})+U^\dagger_{-\eta x}(\mathbf{x}))\Big]\Big)\\ &= -i\mathrm{Tr}\Big(t_a\Big[\tilde{\tau}(U_{xy}(\mathbf{x})-U_{-yx}(\mathbf{x})-U_{yx}(\mathbf{x})+U_{x-y}(\mathbf{x}))\\ &\quad+\frac{1}{\tilde{\tau}a^2_\eta}(U_{x\eta}(\mathbf{x})-U_{-\eta x}(\mathbf{x})-U_{\eta x}(\mathbf{x})+U_{x-\eta}(\mathbf{x}))\Big]\Big).\end{aligned} \tag{3.43}$$

Finally, this is equal to $-\frac{\partial \tilde{E}^x}{\partial \tilde{\tau}}$, which gives,

$$\begin{aligned}\partial_{\tilde{\tau}}\tilde{E}^x = \frac{i}{2}\Big(\Big[&\tilde{\tau}(U_{xy}(\mathbf{x}) - U_{-yx}(\mathbf{x}) - U_{yx}(\mathbf{x}) + U_{x-y}(\mathbf{x})) \\ &+ \frac{1}{\tilde{\tau}a_\eta^2}(U_{x\eta}(\mathbf{x}) - U_{-\eta x}(\mathbf{x}) - U_{\eta x}(\mathbf{x}) + U_{x-\eta}(\mathbf{x}))\Big] - \text{trace}\Big)\end{aligned} \tag{3.44}$$

where the $-$trace subtracts the part that is proportional to the trace. The y-component takes the same form,

$$\begin{aligned}\partial_{\tilde{\tau}}\tilde{E}^y = \frac{i}{2}\Big(\Big[&\tilde{\tau}(U_{yx}(\mathbf{x}) - U_{-xy}(\mathbf{x}) - U_{xy}(\mathbf{x}) + U_{y-x}(\mathbf{x})) \\ &+ \frac{1}{\tilde{\tau}a_\eta^2}(U_{y\eta}(\mathbf{x}) - U_{-\eta y}(\mathbf{x}) - U_{\eta y}(\mathbf{x}) + U_{y-\eta}(\mathbf{x}))\Big] - \text{trace}\Big).\end{aligned} \tag{3.45}$$

For the η-direction, the derivative of the gauge link changes slightly, due to the factor a_η

$$\frac{\partial}{\partial \tilde{A}^a_\eta(\mathbf{x})}U_\eta(\mathbf{x}) = \frac{\partial}{\partial \tilde{A}^a_i(\mathbf{x})}e^{it_a a_\eta \tilde{A}^a_\eta} = it_a a_\eta U_\eta(\mathbf{x}). \tag{3.46}$$

The two plaquettes that are relevant for the η-derivative have a common coefficient in the lattice Hamiltonian, and get this extra factor a_η from the η-derivative. Other than that, the EOM takes the same form as those for the transverse electric fields,

$$\begin{aligned}\partial_{\tilde{\tau}}\tilde{E}^\eta = \frac{i}{2}\frac{1}{\tilde{\tau}a_\eta}\Big(\Big[&(U_{\eta x}(\mathbf{x}) - U_{-x\eta}(\mathbf{x}) - U_{x\eta}(\mathbf{x}) + U_{\eta-x}(\mathbf{x})) \\ &+ (U_{\eta y}(\mathbf{x}) - U_{-y\eta}(\mathbf{x}) - U_{y\eta}(\mathbf{x}) + U_{-\eta y}(\mathbf{x}))\Big] - \text{trace}\Big).\end{aligned} \tag{3.47}$$

For the transverse gauge links, the Hamiltonian EOM's are

$$\frac{\partial \tilde{A}_i}{\partial \tilde{\tau}} = \frac{\partial \tilde{H}}{\partial \tilde{E}^i} = \frac{\tilde{E}^i}{\tilde{\tau}} \tag{3.48}$$

but this needs to be related to the degrees of the freedom on the lattice, namely the gauge links. Taking a time derivative of the transverse gauge link,

$$\partial_{\tilde{\tau}}U_i = \partial_{\tilde{\tau}}e^{i\tilde{A}_i} = i\partial_{\tilde{\tau}}\tilde{A}_i e^{i\tilde{A}_i} = i\partial_{\tilde{\tau}}\tilde{A}_i U_i \tag{3.49}$$

where the ordering of the matrices is taken as written above as an approximation in the small lattice spacing limit. As indicated in Eq. (3.50), U really involves an exponential path integral over the gauge field, but is approximated in the small $a_\perp$ limit as

$$U_i(x_k, x_{k+1}) \approx \exp\Big(iga_\perp A_i(x_k)\Big). \tag{3.50}$$

Having made this approximation, it is not clear which is the appropriate order for the matrices $\tilde{A}_i$ and U_i when taking the derivative, so the order taken in Eq. (3.49) can simply be regarded as a choice that introduces some numerical error. This approximation becomes better, meaning the associated numerical error should decrease, as the lattice spacing approaches the continuum limit.

Plugging Eq. (3.48) in for $\partial_\tau \tilde{A}_i$, one gets,

$$\partial_{\tilde{\tau}} U_i = i \frac{\tilde{E}^i}{\tilde{\tau}} U_i, \tag{3.51}$$

for the transverse components. For the η-component, the equation of motion,

$$\frac{\partial \tilde{A}_\eta}{\partial \tilde{\tau}} = \frac{\partial \tilde{H}}{\partial \tilde{E}^\eta} = \tilde{\tau} \tilde{E}^\eta, \tag{3.52}$$

can be related to the gauge field to the gauge link via

$$\partial_{\tilde{\tau}} U_\eta = \partial_{\tilde{\tau}} e^{i a_\eta \tilde{A}_\eta} = i a_\eta \partial_{\tilde{\tau}} \tilde{A}_\eta e^{i a_\eta \tilde{A}_\eta} = i a_\eta \partial_{\tilde{\tau}} \tilde{A}_\eta U_\eta. \tag{3.53}$$

Plugging Eq. (3.52) in,

$$\partial_{\tilde{\tau}} U_\eta = i a_\eta \tilde{\tau} \tilde{E}^\eta U_\eta \tag{3.54}$$

gives the final equation of motion. To summarize, the lattice equations of motion are,

$$\begin{aligned} \partial_{\tilde{\tau}} U_i &= i \partial_{\tilde{\tau}} \tilde{A}_i U_i = i \frac{\tilde{E}^i}{\tilde{\tau}} U_i \\ \partial_{\tilde{\tau}} U_\eta &= i a_\eta \partial_{\tilde{\tau}} \tilde{A}_\eta U_\eta = i a_\eta \tilde{\tau} \tilde{E}^\eta U_\eta \end{aligned} \tag{3.55}$$

for the gauge links and

$$\begin{aligned} \partial_{\tilde{\tau}} \tilde{E}^x = \frac{i\tilde{\tau}}{2} \Big(& U_{x,y}(\mathbf{x}) + U_{x,-y}(\mathbf{x}) - U_{y,x}(\mathbf{x}) - U_{-y,x}(\mathbf{x}) - \text{trace} \Big) \\ & + \frac{i}{2\tilde{\tau} a_\eta^2} \Big(U_{x,\eta}(\mathbf{x}) + U_{x,-\eta}(\mathbf{x}) - U_{\eta,x}(\mathbf{x}) - U_{-\eta,x}(\mathbf{x}) - \text{trace} \Big) \end{aligned} \tag{3.56}$$

$$\begin{aligned} \partial_{\tilde{\tau}} \tilde{E}^y = \frac{i\tilde{\tau}}{2} \Big(& U_{y,x}(\mathbf{x}) + U_{y,-x}(\mathbf{x}) - U_{x,y}(\mathbf{x}) - U_{-x,y}(\mathbf{x}) - \text{trace} \Big) \\ & + \frac{i}{2\tilde{\tau} a_\eta^2} \Big(U_{y,\eta}(\mathbf{x}) + U_{y,-\eta}(\mathbf{x}) - U_{\eta,y}(\mathbf{x}) - U_{-\eta,y}(\mathbf{x}) - \text{trace} \Big) \end{aligned} \tag{3.57}$$

$$\begin{aligned} \partial_{\tilde{\tau}} \tilde{E}^\eta = \frac{i}{2 a_\eta \tilde{\tau}} \Big(& U_{\eta,x}(\mathbf{x}) + U_{\eta,-x}(\mathbf{x}) - U_{-x,\eta}(\mathbf{x}) - U_{x,\eta}(\mathbf{x}) \\ & + U_{\eta,y}(\mathbf{x}) + U_{\eta,-y}(\mathbf{x}) - U_{y,\eta}(\mathbf{x}) - U_{-y,\eta}(\mathbf{x}) - \text{trace} \Big) \end{aligned} \tag{3.58}$$

for the evolution of the electric field components. Gauss' Law is an additional constraint, the lattice form of which will be discussed in Section 4.6 regarding generalizing the initial conditions to 3D.

3.5 Conservation of Energy

The advantage of the Hamiltonian formulation is that it guarantees energy conservation, which we turn to now. The statement of energy conservation in Milne-coordinates, outlined from a hydrodynamic point of view in [72], is given by,

$$\begin{aligned} \partial_\tau T^{\tau\nu} &= 0 \\ \partial_\tau T^{\tau\tau} + \partial_\perp T^{\perp\tau} + \partial_\eta T^{\eta\tau} &= -\tau T^{\eta\eta} - T^{\tau\tau}/\tau \end{aligned} \tag{3.59}$$

where the terms on the right-hand side are geometric terms coming from Christoffel symbols. Multiplying by τ and combining the two $T^{\tau\tau}$ terms gives

$$\partial_\tau(\tau T^{\tau\tau}) + \partial_\perp(\tau T^{\perp\tau}) + \partial_\eta(\tau T^{\eta\tau}) = -\tau^2 T^{\eta\eta}. \tag{3.60}$$

Integrating over the 4-dimensional volume ($dxdyd\tau\tau d\eta$) where we have already included the factor of τ,

$$\begin{aligned} \int dxdyd\eta d\tau \partial_\tau(\tau T^{\tau\tau}) + \int dxdyd\eta d\tau \partial_\perp(\tau T^{\perp\tau}) + \int dxdyd\eta d\tau \partial_\eta(\tau T^{\eta\tau}) \\ = -\int dxdyd\eta d\tau(\tau^2 T^{\eta\eta}). \end{aligned} \tag{3.61}$$

The second term becomes an integral over the transverse boundary, where the stress energy tensor is zero, so this term vanishes. The remaining terms are

$$\int dxdyd\eta(\tau T^{\tau\tau})\Big|_{\tau_{min}}^{\tau_{max}} + \left(\int dxdyd\tau(\tau T^{\eta\tau})\right)\Big|_{\eta_{min}}^{\eta_{max}} = -\int dxdyd\eta d\tau(\tau^2 T^{\eta\eta}). \tag{3.62}$$

In Fig. (3.2), the deviation of the ratio of the LHS to the RHS of Eq. (3.62) from unity is plotted. Explicitly, the quantity on the y-axis is

$$\left(1 - \frac{\int dxdyd\eta(\tau T^{\tau\tau})\Big|_{\tau_{min}}^{\tau_{max}} + \left(\int dxdyd\tau(\tau T^{\eta\tau})\right)\Big|_{\eta_{min}}^{\eta_{max}}}{-\int dxdyd\eta d\tau(\tau^2 T^{\eta\eta})}\right) \times 100\%. \tag{3.63}$$

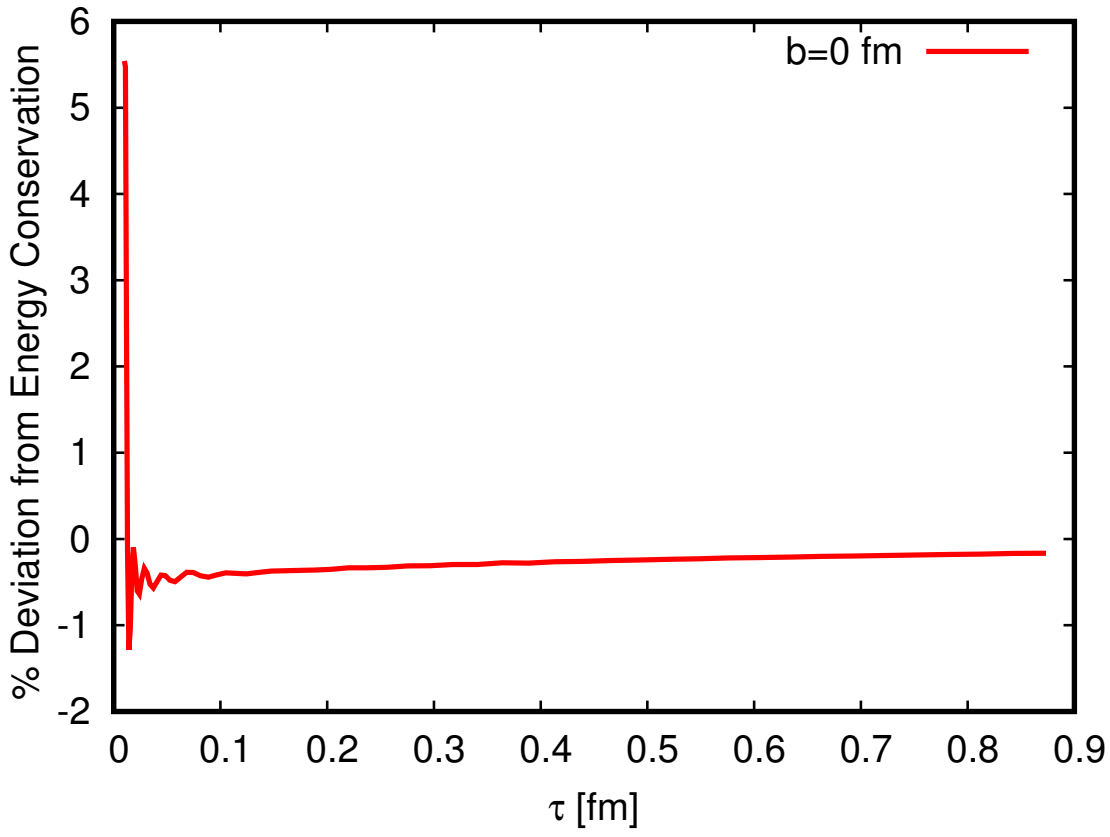

Figure 3.2: Despite fluctuations at very early times, energy is nicely conserved throughout the evolution of the system. This figure is a typical event with $b = 0\,\mathrm{fm}$.

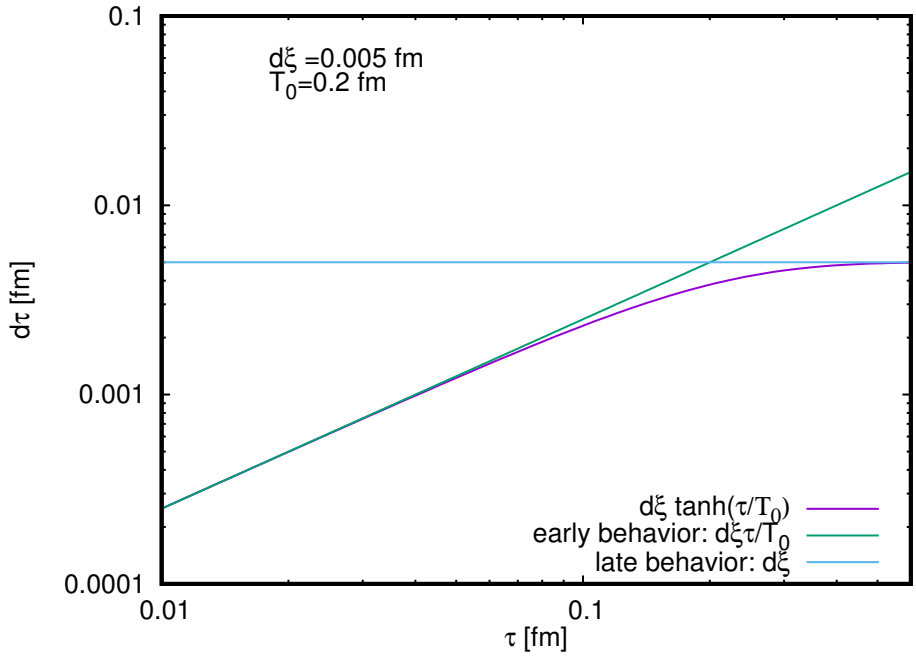

Figure 3.3: The form of the adaptive time step used as a function of time. Parameters are chosen to illustrate the limiting behavior at early times and late times. For the results in this thesis the following parameters are used: $d\xi = 0.035 a_\perp$, $T_0 = 8 a_\perp$, with $a_\perp = 0.044\,\text{fm}$.

There is deviation from energy conservation at extremely early times, likely due to lattice effects. Two such sources of numerical error are the approximations made in Eqs. (3.49) and (3.53), which both rely on small lattice spacing. The curve quickly settles down and approaches zero, indicating that energy is conserved throughout the evolution. It is worth noting that because of the time integrations in Eq. (3.62), in order to get an accurate measure, one must compute $T^{\mu\nu}$ at sufficiently fine time intervals, which can be computationally expensive.

3.6 Adaptive Time Steps

The equations of motion require very small time steps at early times, but not at later times, due to the appearance of $\frac{d\tau}{\tau}$ terms. For this reason, adaptive time steps are employed in the following form,

$$d\tau = d\xi \tanh \frac{\tau}{T_0}. \tag{3.64}$$

For $\tau << T_0$, this behaves as $d\tau \approx d\xi \frac{\tau}{T_0}$ while for $\tau > T_0$ the value plateaus at $d\tau \approx d\xi$. This achieves the goal of producing small time steps for small τ and larger time steps for later times, when they are no longer necessary. The dynamical time step is shown for values $T_0 = 0.2\,\text{fm}$ and $d\xi = 0.005\,\text{fm}$ in Figure (3.3), in order to illustrate the behavior. As can be seen, $d\xi$ governs the maximum $d\tau$, while T_0 determines how quickly $d\tau$ will grow.

4

Generalizing to 3+1D

4.1 Introduction

The equations of motion have already been outlined for fully 3+1D evolution in Chapter 3. The initial conditions, however, still need to be generalized to 3+1D in a way that is consistent with evolution on a 3-dimensional lattice. In this section, the saturation scale, as determined by IP-Sat, will be used to the determine the scale from which to sample the color charge, although in 3+1D this will be done away from mid-rapidity. Solving the Poisson equation with this color charge will allow for the initialization of the Wilson lines. The JIMWLK equations, QCD-based renormalization group equations, will then evolve this Wilson lines to all other rapidities. Next, the initial condition for the gauge fields from 2D will be altered and applied at all rapidities. Finally, Gauss' law will be solved iteratively using an ansatz proposed here. These changes, taken together, provide a non-trivial longitudinal structure that is consistent with temporal evolution of a 3D lattice.

4.2 $Q_s(\eta)$

The saturation scale that is determined from the IP-Sat model is typically used for a boost invariant system. In 3+1D, the saturation scale is rapidity dependent. Different rapidities, y, correspond to different reference frames, and the momemtum fraction x depends on this. To apply IP-Sat away from mid-rapidity, we simply determine the momentum fraction away from mid-rapidity, and use this value of x to solve for the saturation scale. To calculate x

at non-zero rapidities, recall the definition of kinematic rapidity,

$$y = \frac{1}{2}\ln\left(\frac{E+p_z}{E-p_z}\right). \tag{4.1}$$

Constructing the hyperbolic cosine function and simplifying,

$$\begin{aligned}\cosh y = \frac{e^y + e^{-y}}{2} &= \frac{1}{2}\left(\frac{\sqrt{E+p_z}}{\sqrt{E-p_z}} + \frac{\sqrt{E-p_z}}{\sqrt{E+p_z}}\right) \\ &= \frac{1}{2}\frac{E+p_z+E-p_z}{\sqrt{E^2-p_z^2}} = \frac{E}{m_N}\end{aligned} \tag{4.2}$$

one gets a relationship between energy, nucleon mass, and rapidity, allowing us to express the beam rapidity as y_{beam},

$$y_{beam} = \cosh^{-1}\left(\frac{\sqrt{s}}{2m_N}\right). \tag{4.3}$$

In addition, we can use the fact that boosts are additive in rapidity,

$$y_{obs} = y_{beam} - y_{boost} \tag{4.4}$$

To see why this relationship is true, consider a system travelling in the longitudinal direction in two frames, F and F', where they have a relative velocity in the z-direction [73]. The rapidity in frame F' is

$$y' = \frac{1}{2}\ln\left(\frac{p_0'+p_z'}{p_0'-p_z'}\right) \tag{4.5}$$

The Lorentz transformation from F to F' is

$$\begin{aligned}p_0' &= \gamma(p_0 - \beta p_z) \\ p_z' &= \gamma(p_z - \beta p_0)\end{aligned} \tag{4.6}$$

where β is the relative velocity between the frames F' and F. Putting these relationships into the equation for y',

$$\begin{aligned}y' &= \frac{1}{2}\ln\left[\frac{\gamma(p_0-\beta p_z)+\gamma(\beta p_0 - p_z)}{\gamma(p_0-\beta p_z)-\gamma(\beta p_0 - p_z)}\right] \\ &= \frac{1}{2}\ln\left[\frac{(p_0+p_z)(\gamma-\gamma\beta)}{(p_0-p_z)(\gamma+\gamma\beta)}\right] \\ &= y - \frac{1}{2}\ln\left(\frac{1+\beta}{1-\beta}\right) \\ &= y(\text{particle in frame F}) - y(\text{F}' \text{ relative to F})\end{aligned} \tag{4.7}$$

The rapidity of the particle in the two frames differs by the rapidity of the boost between the frames. This property makes rapidity very useful for describing relativistic particles. In order to change frames, one simply has to add/substract the rapidity of the boost.

Using this, one can write the momentum fraction at y' as,

$$x = \frac{Q_s}{m_N \cosh(y_{beam} - y_{boost})} \tag{4.8}$$

With the approximation that $y = \eta$, to be justified in section 4.4, this is given by

$$x = \frac{Q_s}{m_N \cosh(y_{beam} - \eta)} \tag{4.9}$$

Notice that taking $\eta = 0$, one recovers the 2D form that was used in the previous chapter,

$$x = \frac{Q_s}{m_N \cosh(y_{beam})} = \frac{Q_s}{m_N((\sqrt{s}/2)/m_N)} = \frac{Q_s}{\sqrt{s}/2} \tag{4.10}$$

Then one solves Eq. (4.9) iteratively with the equations outlined in Section 2.2. Once the value of $Q_s^2(\mathbf{x}, \eta_{min})$ is determined for each nucleus, the color charge is sampled and the gauge fields can be found using the MV model. Then the JIMWLK evolution evolves the Wilson lines to all other rapidities, as will be discussed in the following section.

4.3 JIMWLK

In a previous chapter, it was argued that the CGC relies on a separation of scale between the hard partons that remain on the light cone and act as sources, and the soft gluons. This is depicted in Fig. (4.1), where y_{cut} separates the source terms from the soft gluons. The exact scale, denoted as y_{cut} was rapidity independent in 2D because the system was boost invariant. This meant that the color charge density was a function of the transverse position and had no longitudinal structure. This is an idealization of course, because heavy-ion collisions are not boost invariant, and y_{obs} is not fixed for a 3D system. The JIMWLK (Jalilian-Marian, Iancu, McLerran, Weigert, Leonidov, Kovner) renormalization equations [74] integrate out modes at higher rapidities, effectively making the separation scale rapidity dependent. This leads to a self-similar Lagrangian to the CGC, meaning that it takes the same form but with a rapidity dependent charge density term,

$$\rho_{2D}(\mathbf{x}_\perp) \xrightarrow{\text{JIMWLK Evolution}} \rho_{3D}(\mathbf{x}_\perp, y) \approx \rho_{3D}(\mathbf{x}_\perp, \eta) \tag{4.11}$$

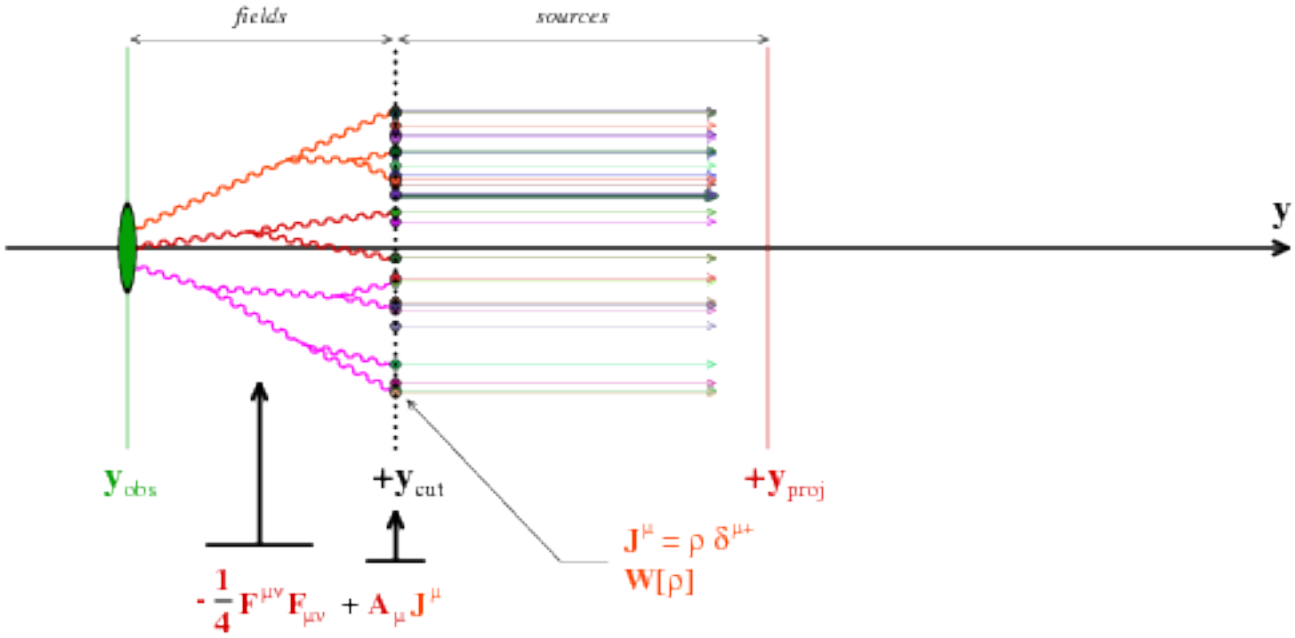

Figure 4.1: Visualization of the separation of scales made in the CGC. Figure taken from [56].

The actual renormalization procedure is outlined in [74]. To summarize, the CGC effective Lagrangian is considered at a momentum scale $k^+ \ll P^+$, where P^+ is an ultraviolet cutoff on the order of the longitudinal momentum of the nucleus under consideration. To obtain the effective Lagrangian at k^+, the quantum fluctuations modes with momentum $k^+ \leq q^+ \leq P^+$ are integrated out. The result is a new effective Lagrangian that takes the same form as that of the CGC, but it now has additional quantum fluctuations integrated out into the charge squared per unit area. Because this process produces a self-similar Lagrangian, it can be done iteratively to higher and higher rapidities, which each successive iteration increasing the charge density. The JIMWLK renormalization equations are thus equations for how $\mu^2(y, Q^2)$, the squared color charge per unit area, evolves as a function of rapidity, y, and the transverse resolution scale, Q^2. The scale of the additional charge squared per unit area at each iteration is

$$\mu^2(y, Q^2)dy = \mu^2(y, Q^2)(-\ln(x)) = \mu^2(y, Q^2)\ln(1/x). \tag{4.12}$$

As long as $\alpha_s \ln\left(\frac{x_N}{x_{N+1}}\right) \ll 1$, where N and $N+1$ label consecutive iterations, the additional

fluctuations can be treated perturbatively, and the renormalization procedure is under control.

More concretely, the JIMWLK equation can be written in Hamiltonian form, derived rigorously using the Schwinger-Keldysh formalism in [63] and [75], as

$$\frac{\partial W_Y[\alpha]}{\partial Y} = H_{JIMWLK} W_Y[\alpha] \tag{4.13}$$

where W_Y is a weight function at rapidity Y and $-\nabla_\perp^2 \alpha(\mathbf{x}_\perp, \mathbf{Y}) = \rho(\mathbf{x}_\perp, Y)$ relates the gauge field to the surface charge density. The Hamiltonian is given by

$$\mathcal{H} = \frac{1}{2\pi} \int_{\mathbf{x},\mathbf{y}} \frac{\delta}{\delta \alpha_a(\mathbf{x}_\perp)} \eta^{ab}(\mathbf{x}, \mathbf{y}) \frac{\delta}{\delta \alpha_b(\mathbf{y}_\perp)}. \tag{4.14}$$

Here, $\eta^{ab}(\mathbf{x}_\perp, \mathbf{y}_\perp) \propto \langle \delta\rho_a(\mathbf{x}_\perp) \delta\rho_b(\mathbf{y}_\perp) \rangle$ is the induced charge-charge correlator between transverse positions $\mathbf{x}_\perp$ and $\mathbf{y}_\perp$[1]. In the CGC, the expectation value of an observable $\mathcal{O}$ is given by,

$$\langle \mathcal{O} \rangle_Y = \int \mathcal{D}[\alpha] W_Y[\alpha] \mathcal{O}[\alpha] \tag{4.15}$$

where now the subscript on W_Y indicates that the rapidity dependence of the theory is in the weight function.

4.3.1 JIMWLK: Numerical Implementation

The form of the JIMWLK equation used is from [3] and given in terms of the Langevin step,

$$\begin{aligned} V_{A,B}(\mathbf{x}, Y + dY) = \exp\left(-i \frac{\sqrt{\alpha_s dY}}{\pi} \int_{\mathbf{z}} \mathbf{K}_{\mathbf{x}-\mathbf{z}} \cdot V_z \xi_z V_z^\dagger\right) \\ \times V_{A,B}(\mathbf{x}, Y) \times \exp\left(i \frac{\sqrt{\alpha_s dY}}{\pi} \int_{\mathbf{z}} \mathbf{K}_{\mathbf{x}-\mathbf{z}} \cdot \xi_z\right) \end{aligned} \tag{4.16}$$

where $\xi_{\mathbf{z}} = \{\xi_{1,a}(\mathbf{z}, Y) t^a, \xi_{2,a}(\mathbf{z}, Y) t^a\}$ and the subscripts $1, 2$ label the transverse directions. Its correlator is given by,

$$\langle \xi_i^a(\mathbf{x}, Y_1) \xi_j^b(\mathbf{y}, Y_2) \rangle = \delta^{ab} \delta^{ij} \delta^2(\mathbf{x} - \mathbf{y}) \delta^{Y_1 Y_2}. \tag{4.17}$$

To be clear, a, b are color indices, i, j label the transverse components x and y, and $\mathbf{x}, \mathbf{y}$ and Y_1, Y_2 label the transverse and longitudinal positions, respectively. Here α_s is constant and

[1] The author has found the thesis [76] to be an instructive and valuable resource for understanding the JIMWLK equation.

the noise correlator has a Kronecker delta for (Y_1, Y_2), rather than a delta function, because the $1/dY$ has already been incorporated into Eq. (4.16). The noise term represents the stochastic nature of the gluon emission, part of the quantum mechanical correction to the charge that sources boost invariant classical fields.

For a running coupling constant, Eq. (4.16) is modified [3]

$$V_{A,B}(\mathbf{x},Y+dY) = \exp\left(-i\frac{\sqrt{dY}}{\pi}\int_{\mathbf{u}}\mathbf{K}_{\mathbf{x}-\mathbf{u}}(\cdot V_u\boldsymbol{\eta}_u V_u^\dagger)\right)V_{A,B}(\mathbf{x},Y)\exp\left(i\frac{\sqrt{dY}}{\pi}\int_{\mathbf{v}}\mathbf{K}_{\mathbf{x}-\mathbf{v}}\cdot\boldsymbol{\eta}_{\mathbf{v}}\right) \tag{4.18}$$

where $\eta_{\mathbf{z}} = \{\eta_1^a(\mathbf{z},Y)t^a, \eta_2^a(\mathbf{z},Y)t^a\}$. The correlator for the noise term, η, in this case is given by,

$$\langle\eta^{a,i}(\mathbf{x},Y_1)\eta^{b,j}(\mathbf{y},Y_2)\rangle = \delta^{ab}\delta^{ij}\delta^{Y_1Y_2}\int\frac{d^2\mathbf{k}}{(2\pi)^2}e^{i\mathbf{k}\cdot(\mathbf{x}-\mathbf{y})}\alpha_s(\mathbf{k}). \tag{4.19}$$

This can be contrasted with the noise term in the constant α_s case,

$$\alpha_s\langle\xi_i^a(\mathbf{x},Y_1)\xi_j^b(\mathbf{y},Y_2)\rangle = \alpha_s\delta^{ab}\delta^{ij}\delta^{Y_1Y_2}\int\frac{d^2\mathbf{k}}{(2\pi)^2}e^{i\mathbf{k}\cdot(\mathbf{x}-\mathbf{y})} \tag{4.20}$$

where we have explicitly written out the δ-function. Notice that the coupling α_s is absorbed into the noise term in Eq. (4.19) and thus it does not appear explicitly in equation Eq. (4.18). In this thesis, the running coupling is used. For the running coupling, the noise correlator is no longer local which breaks the left-right symmetry of the fixed coupling equation (see [3] for details). The notation used in Eq. (4.18) reflects this breaking of symmetry.

The modified kernel, as used in [77], is given by,

$$K_{\mathbf{x}-\mathbf{z}} = m|\mathbf{x}-\mathbf{z}|K_1(m|\mathbf{x}-\mathbf{z}|)\frac{\mathbf{x}-\mathbf{z}}{(\mathbf{x}-\mathbf{z})^2} \tag{4.21}$$

where $K_1(x)$ is the Bessel function of the second kind, and $m = 0.4\,\text{GeV}$ is an infrared regulator . The form of the running coupling is taken to be

$$\alpha_s(\mathbf{k}) = \frac{4\pi}{\beta\ln\left[(\frac{\mu_0^2}{\Lambda_{QCD}^2})^{1/c} + (\frac{\mathbf{k}^2}{\Lambda_{QCD}^2})^{1/c}\right]^c} \tag{4.22}$$

with $\beta = 11 - 2N_f/3$, $\Lambda_{QCD} = 0.2$ GeV, $c = 0.2$, and $\mu_0 = 0.4$ GeV [3].

In principle, the scale at which the noise fluctuations occur should not exceed the saturation scale, as it is the only physical scale in the problem. However, the noise correlator is a

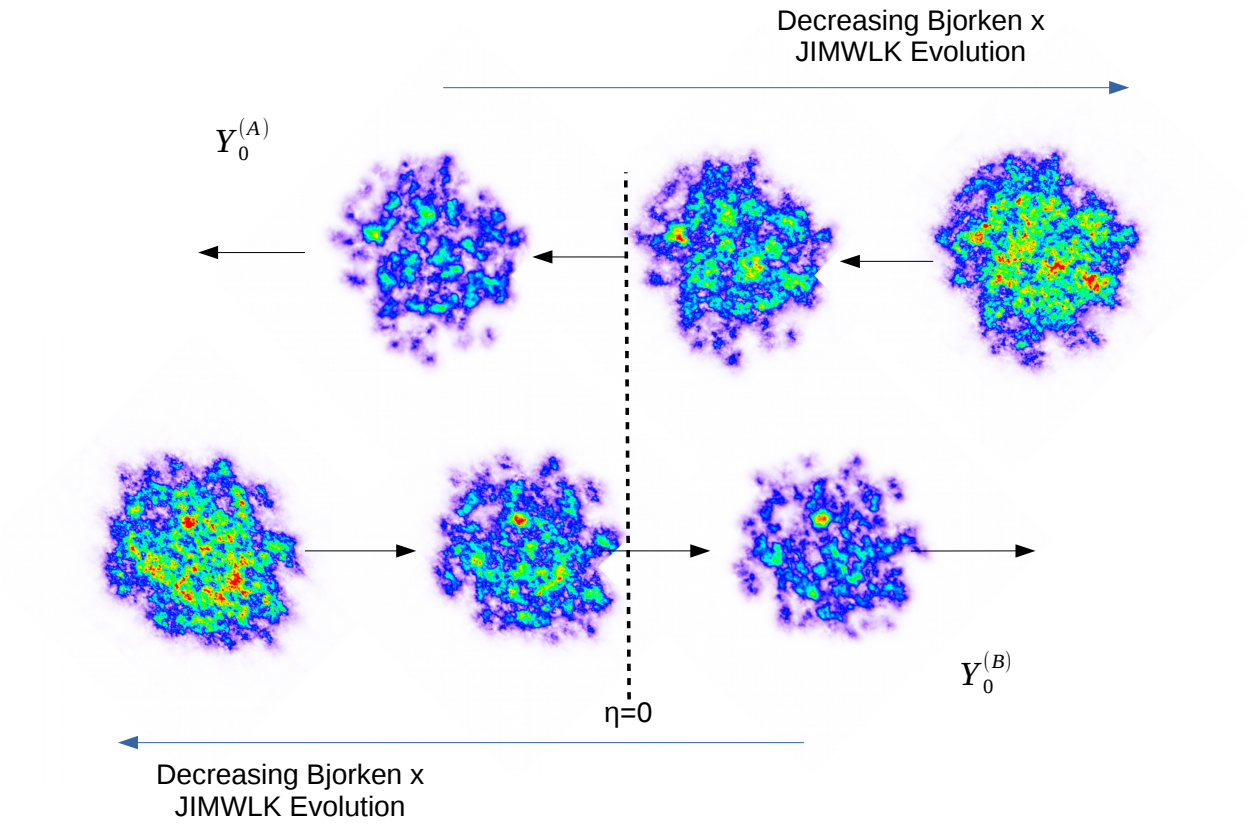

Figure 4.2: Two nuclei evolving in rapidity via the JIMWLK equations. At $Y_A^{(0)}$ and $Y_B^{(0)}$ the Wilson lines are determine as done in the 2D formulation. Then these Wilson Lines are evolved via equation (4.16). Plotted are snapshots of the quantity $\frac{1}{N_c}\mathrm{Tr}(1-V)$, a proxy for gluon density. It is possible to see as the JIMWLK evolution proceeds to smaller Bjorken-x, the gluon density increases while the large scale geometry of the nuclear structure persists.

delta-function, which means the numerical fluctuations take place at the scale of the inverse lattice spacing $\approx 1/a$. Incorporating the running coupling in the kernel acts to filter out higher energy modes. It has been checked that this reduces the lattice-spacing dependence of the initial energy content of the system. Physically, this means that the scale of the running coupling is taken to be that of the emitted gluon. As described in [3], the running coupling implementation slows down the JIMWLK evolution which means that neighboring η values will be more correlated (differ less) than in the constant α_s implementation.

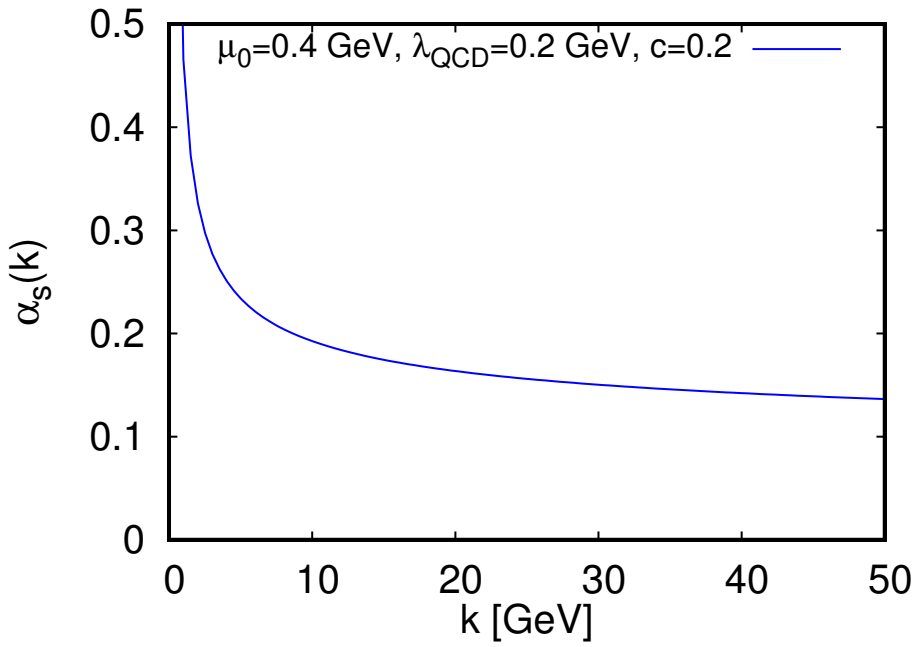

Figure 4.3: The form of $\alpha_s(k)$ used here, as taken from [3], using the parameters cited in the text here.

The expression in the exponent of Eq. (4.16) is computed by Fourier transforming the kernel and the noise terms, thus turning the 2-dimensional integration into a convolution [78]. As discussed in [78], this improves numerical speed considerably: the problem that would have scaled as N^4 is reduce to $N^2 \log(N)$ for an $N \times N$ transverse grid. The form of the integral in the JIMWLK equation takes the form of a convolution [78],

$$\int_{\mathbf{z}} \mathbf{K}_{\mathbf{x}-\mathbf{z}} \cdot \boldsymbol{\xi}(\boldsymbol{z}) = \sum_{\mathbf{x}-\mathbf{z}} \mathbf{K}(\mathbf{x}-\mathbf{z}) \cdot \boldsymbol{\xi}(\mathbf{z}) = \mathcal{F}^{-1}\left[\boldsymbol{\mathcal{F}}(\mathbf{K}) \cdot \boldsymbol{\mathcal{F}}(\boldsymbol{\xi})\right] \tag{4.23}$$

We can Fourier transform the noise term, $\boldsymbol{\xi}(\mathbf{z})$ using FFTW, and the kernel can be done explicitly. The Fourier transform is given by,

$$\boldsymbol{\mathcal{F}}(\mathbf{K}) = \int d^2x e^{-i\mathbf{k}\cdot(\mathbf{x}-\mathbf{z})} m K_1(m|x-z|) \frac{\mathbf{x}-\mathbf{z}}{|x-z|} \tag{4.24}$$

and can be cast in polar coordinates, where each component in the $\hat{x}$ and $\hat{y}$ directions take the form,

$$\mathcal{F}(K) = m \int_0^\infty r dr \int_0^{2\pi} d\theta e^{-ikr\cos\theta} K_1(m|r|)\cos(\theta). \tag{4.25}$$

After the angular integration, one finds

$$\mathcal{F}(K) = -2\pi i m \int_0^\infty r dr J_1(kr) K_1(m|r|) \tag{4.26}$$

where J_1 is a Bessel function of the first kind. Finally, the radial integration gives

$$\mathcal{F}(\mathbf{K}) = \frac{-2\pi i \mathbf{k}}{k^2 + m^2} \tag{4.27}$$

where the two components have been recombined to form the vector quantity. This can be convoluted with the Fourier transformed noise term,

$$\begin{aligned} \int_{\mathbf{z}} \mathbf{K}_{\mathbf{x}-\mathbf{z}} \cdot \boldsymbol{\xi}(\mathbf{z}) = \sum_{\mathbf{z}} \mathbf{K}(\mathbf{x}-\mathbf{z}) \cdot \boldsymbol{\xi}(\mathbf{z}) &= \mathcal{F}^{-1}\left[\boldsymbol{\mathcal{F}}(\mathbf{K}) \cdot \boldsymbol{\mathcal{F}}(\boldsymbol{\xi})\right] \\ &= \mathcal{F}^{-1}\left[\frac{-2\pi i \mathbf{k}}{k^2 + m^2} \cdot \boldsymbol{\xi}(\mathbf{k})\right] \end{aligned} \tag{4.28}$$

The numerical technique used to compute this quantity will be discussed in Section 8.2.

4.3.2 Testing JIMWLK Evolution

The most important scale in the problem is the saturation which is now rapidity dependent. One does not know the value of $Q_s(y)$ directly from the JIMWLK evolution since this equation evolves the Wilson lines. In order to calculate or "measure" the value of $Q_s(y)$, one can compute the Wilson line correlator between two points in the transverse plane, say $\mathbf{x}$ and $\mathbf{z}$, at a fixed rapidity via [79],

$$C(r = |\mathbf{x}_\perp - \mathbf{z}_\perp|) = \frac{1}{N_c}\langle \mathrm{Tr}(V_x^\dagger V_z)\rangle \tag{4.29}$$

where V_x and V_z are the Wilson lines at transverse positions $\mathbf{x}$ and $\mathbf{z}$, and the average is done over the transverse plane. The saturation scale is then typically defined [79] as $Q_s^2 = \frac{2}{r_s^2}$ where r_s is the distance between $\mathbf{x}$ and $\mathbf{z}$ for which the correlator drops to $e^{-1/2}$, meaning

$$C(r_s = \frac{\sqrt{2}}{Q_s}) = e^{-1/2}, \tag{4.30}$$

although sometimes different definitions are taken [77]. This quantity, $C(r)$, is plotted in Fig. (4.4), and three distinct rapidities are highlighted to show the direction of increasing Q_s, which coincides with the direction of the JIMWLK evolution, but opposes the direction

of propagation of the nucleus. The horizontal red line indicates the value $e^{-1/2}$, making it easy to read off the value of Q_s from the horizontal axis.

To quantify how fast the saturation scale changes via the JIMWLK evolution, the following quantity is used [3],

$$\lambda = \frac{d\ln(Q_s^2(y))}{dy}. \tag{4.31}$$

Rather than solving this equation, it is simpler to simply fit the curve of $Q_s^2(y)$ vs y with an

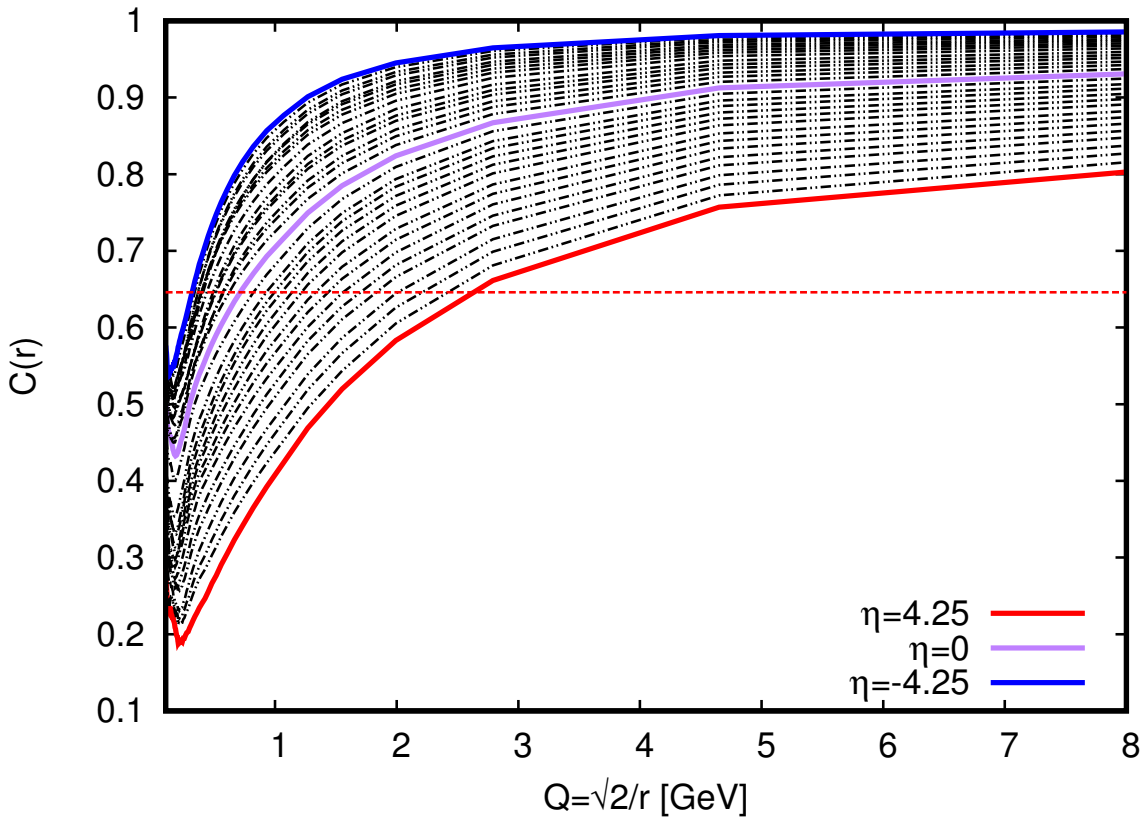

Figure 4.4: An example of the the Wilson line correlator as a function of $\frac{\sqrt{2}}{r}$ under numerical testing conditions using a running coupling. Highlighted in color are three rapidity slices, showing the direction of saturation scale growth, increasing from negative rapidity to positive rapidity. The saturation scale can be read off of the curves from where they cross the horizontal red $C(r) = e^{(-1/2)}$ line.

exponential that solves Eq. (4.31), namely

$$Q_s^2(y) = Q_s^2(y_0)e^{\lambda(y-y_0)}, \tag{4.32}$$

and extract a fit parameter for λ. Data from structure functions suggest the value should be around $\lambda = 0.2 - 0.3$ [80].

In Fig. (4.5), a sheet of coloured glass is used to measure the evolution speed of the JIMWLK implementation. In this context, a sheet of coloured glass is simply a rapidity slice for which a constant scale $g^2\mu$ that is independent of the transverse position $\mathbf{x}_\perp$, is used to sample the colour charge. Using such a setup removes the length scales associated with the nucleus and nucleons which allows for a cleaner measurement of the evolution of the saturation scale across rapidities. For sake of comparison, λ is extracted via fit in Fig. (4.5) for the case of constant coupling $\alpha_s = 0.3$ as well as for the running coupling described in the previous section $\alpha_s(\mathbf{k})$. For the running coupling, several different initial values of the saturation scale $Q_{s,0}$ are used. As one would expect, the running coupling slows down the JIMWLK evolution for higher values of $Q_{s,0}$, as indicated by smaller extracted values of λ. The values of λ extracted are consistent with those plotted in Fig (8) of [3]. For the values of Q_s probed in the Pb-Pb collisions presented in this thesis, $\lambda \approx 0.5$. The constant $\alpha_s = 0.3$ leads to a much larger value of $\lambda \approx 0.9$.

It has been argued that the energy density deposition in the transverse plane in the IP-Glasma framework, after averaging over color charge fluctuations, goes like [81]

$$\epsilon \propto (Q_s^A)^2(Q_s^B)^2. \tag{4.33}$$

Using this, along with the determination of Q_s from the Wilson line correlator, it is possible to roughly estimate how the multiplicity will behave as a function of rapidity,

$$\frac{dN}{dy}(y) \propto (Q_s^A(y))^2(Q_s^B(y))^2 \tag{4.34}$$

where $\langle ... \rangle$ is the average for a given rapidity slice. For asymmetric systems such as p-A collisions, the asymmetry in the rapidity evolution of the proton and nucleus naturally lead to asymmetry in the rapidity dependence of the energy. Thus, the JIMWLK evolution

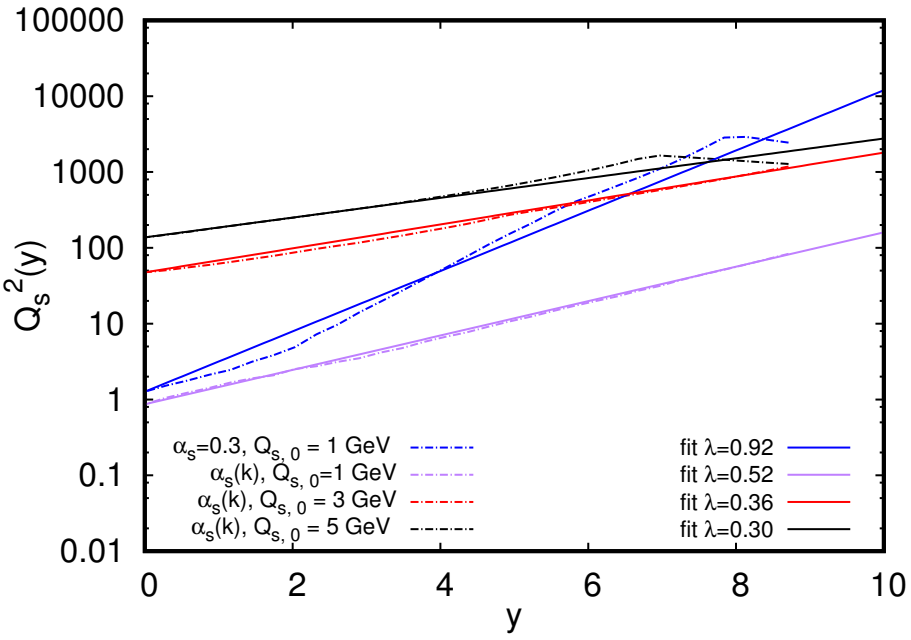

Figure 4.5: This figure shows the growth of the saturation scale due to the JIMWLK evolution for different initial values of $Q_{s,0}$. For each curve ~ 20 events are averaged for $Q_s^2(y)$ and fit with an exponential to extract λ. This is done for the running coupling, $\alpha_s(k)$, as well as for $\alpha_s = 0.3$.

should be able to naturally generate asymmetries in the rapidity dependence of the final state particles, thereby achieving at least qualitative agreement with experimental data.

Lattice effects are expected to become large when $Q_s \sim \frac{1}{L}$ or $Q_s \sim \frac{1}{a}$ where L is the linear size of the system in the transverse plane and a is the transverse lattice spacing [3]. The JIMWLK evolution leads to approximately exponential growth of the saturation scale, which puts limits on the rapidity range one can explore for a given lattice size and lattice spacing. For most of the results presented in this thesis, the rapidity range used is $|y| < 4.25$, and the value of Q_s should remain between the values

$$\frac{1}{L} = \frac{1}{22\,\mathrm{fm}} \approx 0.009\,\mathrm{GeV} \tag{4.35}$$

and

$$\frac{1}{a} = \frac{1}{22\,\mathrm{fm}/500} \approx 4.5\,\mathrm{GeV}. \tag{4.36}$$

The value of Q_s explored in this work are well within this range. Due to the presence of strong transverse fields in the 3D formulation, as will be discussed later in this chapter, the saturation scales used to initialize the JIMWLK evolution in this work are smaller than those used in 2D simulations.

Both the 2D simulation and the rapidity slice used to initialize the JIMWLK evolution at $\pm y_{max}$ use IP-Sat to determine the saturation scale (as opposed to Eqs. (4.29) and (4.30), which are used here to measure Q_s from the Wilson lines). Using IP-Sat, Q_s is related to the scale that is sampled for the color charge by a constant of proportionality $Q_s = Cg^2\mu$ where C is a constant. In 2D, C = 0.5-0.75, whereas $C = 1.42$ is used in this work. This reduces the scale that is sampled for the color charge by a factor of about 2-3 compared to what is typically done in 2D.

It is worth noting that the rapid increase of Q_s^2 for the $\alpha_s = 0.3$ curve in Fig. (4.5) restricts the rapidity range accessible to a given lattice as compared to a smaller effective value of α_s. The smaller value of λ for the running coupling, for example, means that Q_s grows more slowly and a larger rapidity interval is numerically accessible for a fixed lattice, as compared to $\alpha_s = 0.3$.

Finally, now that the JIMWLK equation as well as its numerical implementation and

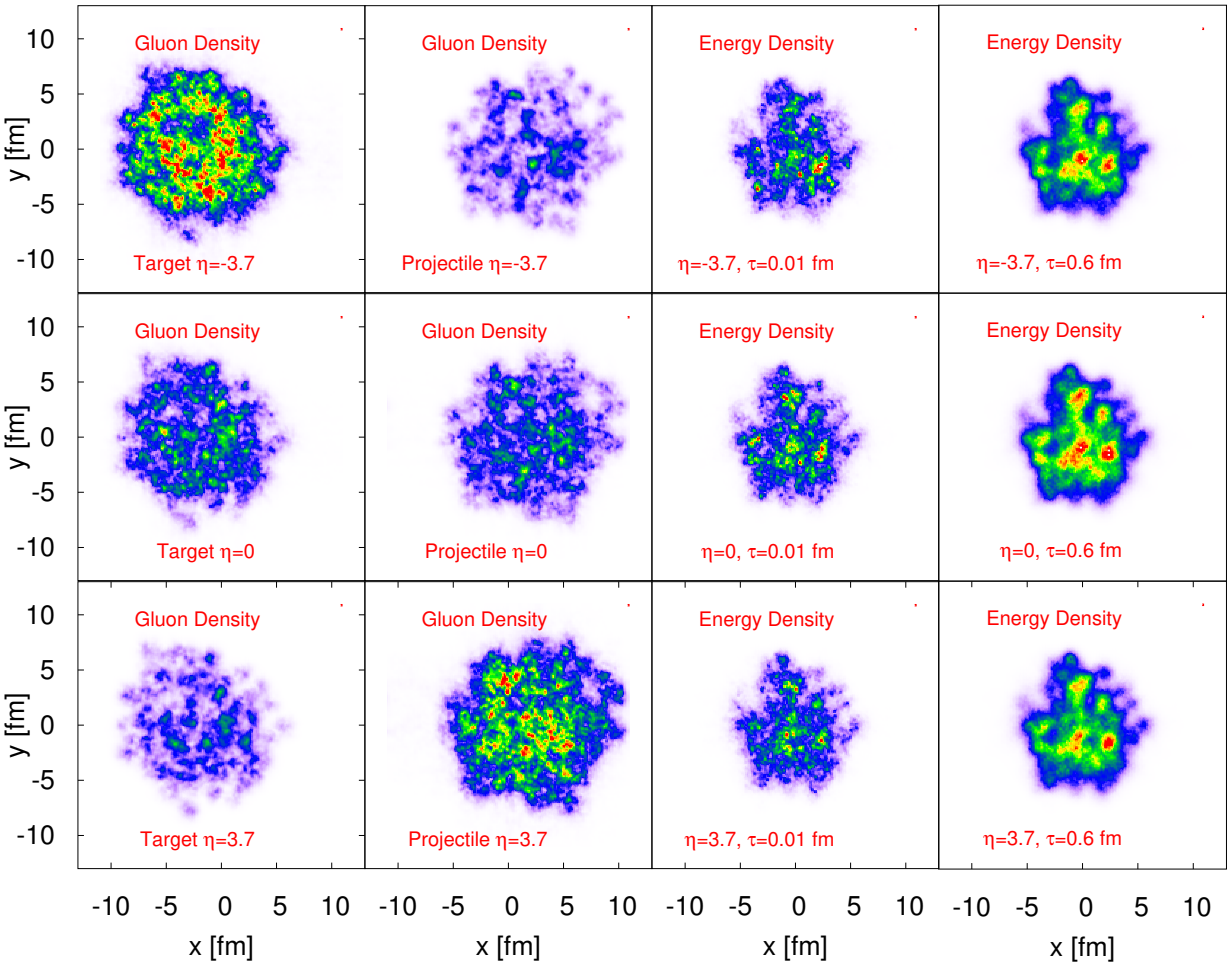

Figure 4.6: The left column is gluon density of the target at different rapidities. The second column from the left is the same quantity, but for the projectile. The third column is the initial energy density that is deposited in the transverse plane at different rapidities. The right column is the same quantity, evolved using CYM until $\tau = 0.6$ fm. The color scales are different for gluon density and energy density, but both are arbitrary.

testing have been discussed, it is worthwhile to get a qualitative phenomenological understanding of its effect. In Fig. (4.6), the first column on the left shows the gluon density of the target nucleus at three different rapidities, evolving from negative rapidity (bottom

row) to positive rapidity (top row), with increasing gluon density. The target, in the case, is propagating in the direction of positive rapidity. The easiest way to make sense of this is to consider boosting along the beam axis. Given a boost with the nucleus, i.e. in the positive rapidity direction, the nucleus will appear slower, and thus less dense. Given a boost in the opposite direction, against the direction of propagation, the nuclei will appear faster and thus more dense. In the second column, the same quantity is plotted but for the projectile nucleus, propagating in the direction of negative rapidity. It is clear that the JIMWLK evolution increases the gluon density of the nucleus through gluon radiation, but that the nuclei retain their global geometric features. The third column shows the initial energy density after the collision at $\tau_0 = 0.01\,\text{fm}$, resulting from the collison of the nuclei shown in the first two columns. Finally the fourth column is the energy density after the Classical Yang-Mills evolution at $\tau = 0.6\,\text{fm}$. The CYM time evolution smooths out the small scale structure of the initial gauge fields at τ_0.

4.4 From Kinematic Rapidity to Spacetime Rapidity

The JIMWLK evolution is in the kinematic rapidity variable y, but as discussed in the section on the equations of motion, the system is evolved in $\tau - \eta$ coordinates, meaning that the Wilson lines that are evolved in y in this chapter via the JIMWLK equations, need to be converted or connected in some way to their position in η. Consider a particle traveling in the z-direction

$$y = \frac{1}{2}\ln\left(\frac{E+p_z}{E-p_z}\right) = \frac{1}{2}\ln\left(\frac{\gamma m + \gamma m v_z}{\gamma m - \gamma m v_z}\right) \approx \frac{1}{2}\ln\left(\frac{t+z}{t-z}\right) = \eta_s \tag{4.37}$$

where the approximation $v_z \approx z/t$ was made. Because this is a good approximation in the highly relativistic limit, we convert the JIMWLK evolution which is a function of y to space-time rapidity by simply taking $y \to \eta_s$.

4.5 Initial Gauge Fields

In Chapter (2.4), the gauge fields for the pre-collision nuclei in the boost invariant case were discussed. This solution does not work in the 3+1D case. To see why, consider gauge fields

that are pure gauge outside of the source terms,

$$A_\mu = -\frac{i}{g} V \partial_\mu V^\dagger \tag{4.38}$$

A pure gauge can be gauge transformed to zero, which means Eq. (4.38) should not contribute to the physically measurable field strength tensor $F_{\mu\nu}$. To see this mathematically, plug Eq. (4.38) into the field strength,

$$\begin{aligned} F_{\mu\nu} &= \partial_\mu A_\nu - \partial_\nu A_\mu + ig[A_\mu, A_\nu] \\ &= \partial_\mu(-\frac{i}{g} V \partial_\nu V^\dagger) - \partial_\nu(-\frac{i}{g} V \partial_\mu V^\dagger) + ig[(-\frac{i}{g} V \partial_\mu V^\dagger), (-\frac{i}{g} V \partial_\nu V^\dagger)] \\ &= -\frac{i}{g} \partial_\mu V (\partial_\nu V^\dagger) + \frac{i}{g} \partial_\nu V \partial_\mu V^\dagger - \frac{i}{g} V (\partial_\mu V^\dagger) V (\partial_\nu V^\dagger) \\ &+ \frac{i}{g} V (\partial_\nu V^\dagger) V (\partial_\mu V^\dagger). \end{aligned} \tag{4.39}$$

Using the fact that $-\partial_\mu V V^\dagger = V \partial_\mu V^\dagger$, the third and fourth terms can be simplified and the whole expression is shown to vanish,

$$\begin{aligned} F_{\mu\nu} = &-\frac{i}{g} \partial_\mu V \partial_\nu V^\dagger + \frac{i}{g} \partial_\nu V \partial_\mu V^\dagger + \frac{i}{g} \partial_\mu V \partial_\nu V^\dagger \\ &- \frac{i}{g} \partial_\nu V \partial_\mu V^\dagger = 0. \end{aligned} \tag{4.40}$$

However, if one were to use the 2D initial gauge fields outlined in Section (2.5) for a non-boost invariant system, the rapidity derivatives would lead to energy deposition in the transverse plane wherever a single nucleus had non-zero gauge fields, rather than only in the overlapping interaction region between both nuclei. This is shown in the left panel of Fig. (4.7). The reason is the initial gauge field in the 2D formulation is a pure gauge field in the transverse dimensions (again, outside of the source terms), and $A_\eta = 0$. This works because the longitudinal direction is trivial in the boost invariant scenario and the problem is essentially 2D. If one plugs the initial gauge field from the 2D formulation into the field strength tensor $F_{i\eta}$, in a 3-dimensional system, one finds

$$F_{i\eta} = \partial_i A_\eta - \partial_\eta A_i + ig[A_i, A_\eta] = \partial_\eta A_i \neq 0. \tag{4.41}$$

In other words, there is no commutator term to cancel the η derivative term in the case of pure gauge. Thus, in order to preserve the necessary condition that the field strength

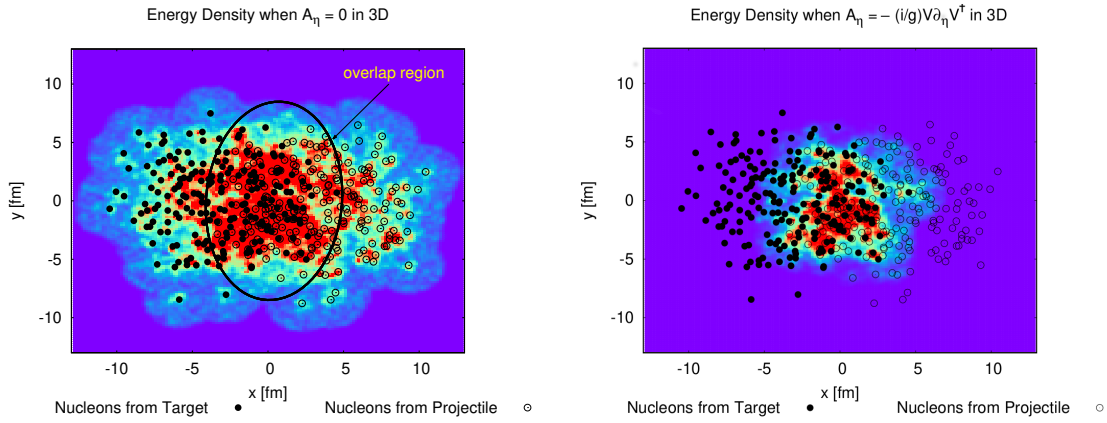

Figure 4.7: Left: The transverse energy density if the 2D initial condition for the gauge fields is applied in a system with longitudinal structure. As can be seen, energy density is deposited outside of the interaction region. Right: The resulting transverse energy density for the same nucleon positions as shown on the left but with the inclusion of the pure gauge component for the longitudinal gauge field.

vanishes outside of the interaction region of the two nuclei, the η component on the initial gauge field is altered to also be pure gauge,

$$A_\eta = -\frac{i}{g} V \partial_\eta V^\dagger. \tag{4.42}$$

This is the natural extension of the purely transverse pure gauge in the 2-dimensional boost invariant scenario. It both retains the crucial feature that the field strength vanishes for an individual nucleus, as shown in the right panel of Fig. (4.7), and reduces to the 2D initial condition in the boost invariant limit for which η derivatives vanish.

Because the two nuclei have different source terms, it is not possible to simultaneously gauge transform to vacuum for both nuclei, even outside of the source terms. This means that in the forward light-cone, the overlap region in the transverse plane will have a non-vanishing field strength, and energy will be deposited. For the forward lightcone, we adopt the analogous equation to the transverse gauge fields,

$$A_\eta = A_\eta^{(A)} + A_\eta^{(B)}. \tag{4.43}$$

The initial condition for the longitudinal electric field remains the same as it was in the 2D

formulation (up to a minus sign from the covariant derivative convention used here),

$$E^{\eta} = ig[A_i^{(A)}, A_i^{(B)}]. \tag{4.44}$$

4.6 Gauss' Law

The covariant form of Gauss' law in $\tau - \eta$ coordinates without a source term is given by

$$[D_i, E^i] + [D_\eta, E^\eta] = 0 \tag{4.45}$$

In the boost invariant system, derivatives in η vanish which leaves,

$$[D_i, E^i] = 0. \tag{4.46}$$

This is trivially solved by $E^i = 0$, making the electric field in the 2D system purely longitudinal at the initial time. This is true, however, only in the limit of infinite momentum. At finite energies, the longitudinal derivatives do not vanish and it is necessary to enforce Gauss' law locally.

The form of E^η at a given rapidity slice is fixed by the 2D initial condition, and has a rapidity dependence that comes from the JIMWLK evolution. Thus, we can take the rapidity term as fixed and treat it as a source term,

$$\begin{aligned} [D_i, E^i] + [D_\eta, E^\eta] &= 0 \\ [D_i, E^i] &= -[D_\eta, E^\eta] \\ [D_i, E^i] &= -\rho \end{aligned} \tag{4.47}$$

This is one equation with two unknowns: E^x and E^y. In order to solve this problem, we take the ansatz

$$E^i = [D^i, \phi] \tag{4.48}$$

which relates the two unknowns and converts Gauss' law into the covariant Poisson equation,

$$[D_i, [D^i, \phi]] = -\rho. \tag{4.49}$$

To discuss the numerical solution, consider first the regular Poisson equation,

$$\nabla^2 \phi = -\rho.$$

This can be solved using the Jacobi method. Discretizing, where i and j label the lattice site in the x and y directions, respectively, yields

$$\frac{\phi_{i+1,\,j}+\phi_{i-1,\,j}-2\phi_{i,\,j}}{a_{xy}^2}+\frac{\phi_{i,\,j+1}+\phi_{i,\,j-1}-2\phi_{i,\,j}}{a_{xy}^2}=-\rho_{i,\,j}. \tag{4.50}$$

This can be solved for $\phi_{i,\,j}$,

$$\phi_{i,\,j}=\frac{1}{4}(\phi_{i+1,\,j}+\phi_{i-1,\,j}+\phi_{i,\,j+1}+\phi_{i,\,j-1}+a_{xy}^2\rho_{i,\,j}). \tag{4.51}$$

Then the Jacobi iterative procedure gives the $(n+1)^{\text{th}}$ iteration in terms of the values at the n^{th} iteration via,

$$\phi_{i,\,j}^{n+1}=\frac{1}{4}(\phi_{i+1,\,j}^{n}+\phi_{i-1,\,j}^{n}+\phi_{i,\,j+1}^{n}+\phi_{i,\,j-1}^{n}+a_{xy}^2\rho_{i,\,j}^{n}). \tag{4.52}$$

For covariant derivatives, all quantities not located at the $i\,,j$ lattice site, need to be parallel transported,

$$\begin{aligned}\phi_{i,\,j}^{n+1}=\frac{1}{4}(&U_{i,\,j}\phi_{i+1,\,j}^{n}U_{i,\,j}^{\dagger}+U_{i-1,\,j}^{\dagger}\phi_{i-1,\,j}^{n}U_{i-1,\,j}+\\&U_{i,\,j}\phi_{i,\,j+1}^{n}U_{i,\,j}^{\dagger}+U_{i,\,j-1}^{\dagger}\phi_{i,\,j-1}^{n}U_{i,\,j-1}+a_{xy}^2\rho_{i,\,j}^{n}).\end{aligned} \tag{4.53}$$

It can be shown that the equations of motion preserve Gauss' law throughout the evolution and this has been checked explicitly for the numerical simulation. A summary of the updated initial conditions, including the solution to Gauss' law and the initial gauge fields is shown in Fig. (4.8).

4.7 Evolution of Fields and Pressure

In the boost invariant formulation, Gauss' law leads to $E^i(\tau=0^+)=0$. This is due to the lack of longitudinal structure that leads to vanishing derivatives in η. Similarly, the transverse chromo-magnetic fields vanish at initial time

$$F_{i\eta}=\partial_i A_\eta-\partial_\eta A_i+ig[A_i,A_\eta]=0 \tag{4.54}$$

because $A_\eta(\tau=0^+)=0$ and the derivatives in η are vanishing. This means that the initial chromo-electric and chromo-magnetic fields are purely longitudinal in 2+1D, the so called "flux-tube" picture that constitutes the widely held picture of the early time dynamics of the chromo-electric and chromo-magnetic fields.

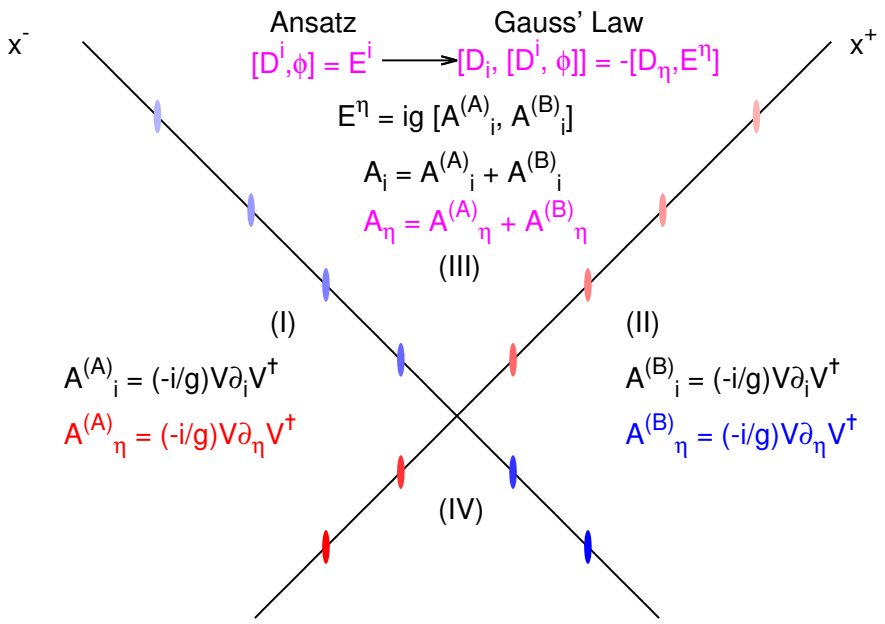

Figure 4.8: Visual summary of initial condition for gauge and electric fields in 3+1D. The colored labels represents things that differ from the 2+1D formulation. Nuclei are represented propagating with finite thickness but are still treated as δ-functions.

The picture of longitudinal flux tubes does not hold in 3+1D. Due to non-vanishing longitudinal derivatives and the changes in the initial condition described in the previous section, the fields are no longer purely longitudinal and the energy density is dominated by the transverse fields. To see why, consider the form of the energy density in the different fields,

$$\epsilon_{i=x,y} = \frac{1}{2}\frac{1}{\tau^2}\Big[(E^i)^2 + (B^i)^2\Big] \tag{4.55}$$

$$\epsilon_\eta = \frac{1}{2}\Big[(E^\eta)^2 + (B^\eta)^2\Big]. \tag{4.56}$$

The evolution of the energy density in the fields can be seen for both the 2+1D and 3+1D scenarios in Fig. (4.9). In 2+1D the transverse fields are identically zero at $\tau = 0^+$ and grow until their contribution to the energy density is comparable to the longitudinal fields. In 3+1D the transverse fields provide the majority of the energy density initially. By typical hydrodynamic initialization times of $\tau = 0.2 - 0.6\,\mathrm{fm}$, the 3+1D fields all have similar contributions to the energy, as is the case in 2+1D.

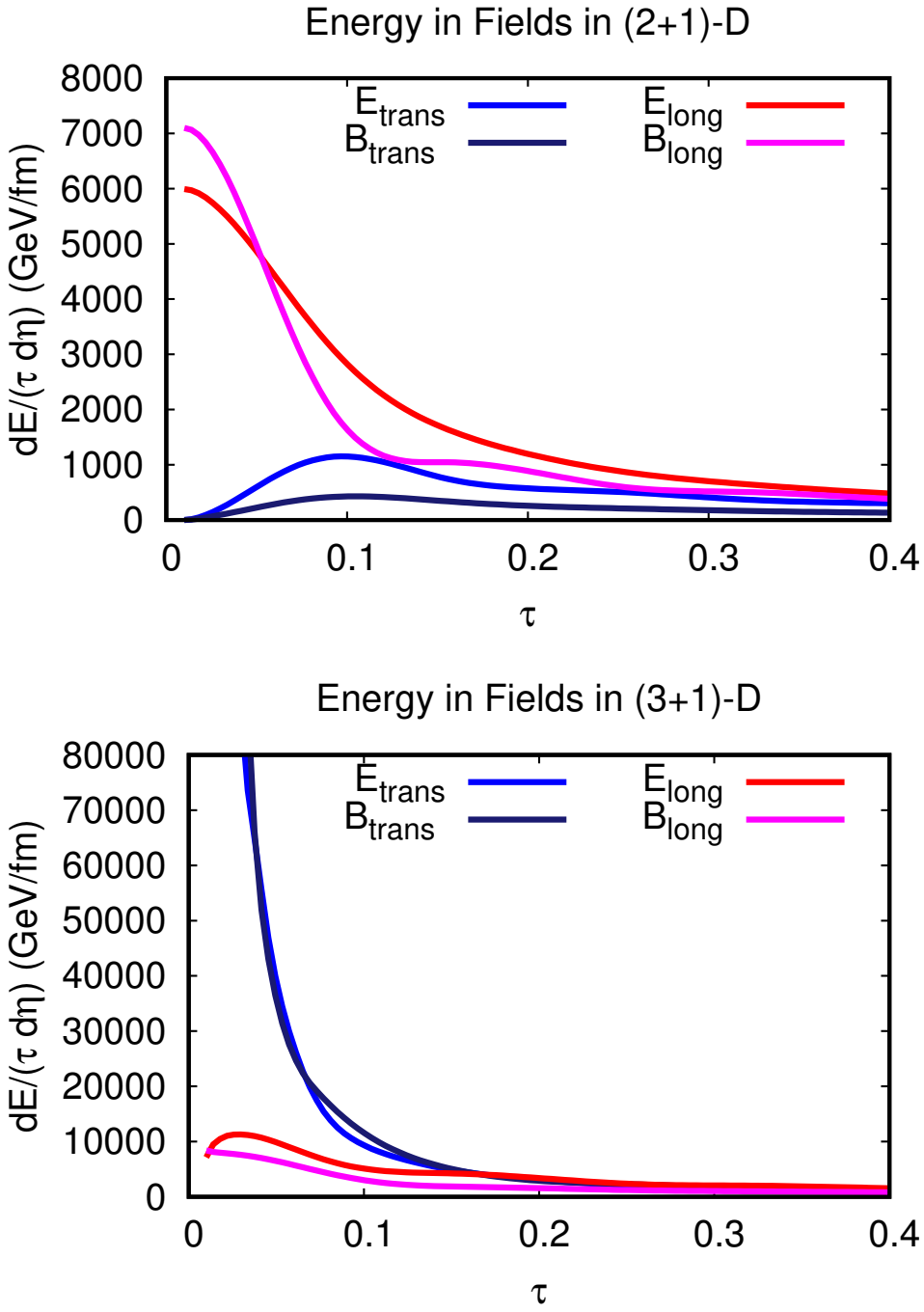

Figure 4.9: Top: The time evolution of the energy density in the different field components in 2+1D. Bottom: The same quantity as the left panel plotted for the 3+1D implementation. Both results are computed using the same 3+1D software, but with the initial 2+1D and 3+1D setups, respectively. For both plots, the x-axis, τ, is in fm.

The early time behavior of the fields in 3+1D causes the longitudinal and transverse pressures to behave radically different than in the boost invariant case. First, it is useful to express the diagonal components of the stress energy tensor in terms of the quantities defined in eq. [4.55],

$$\begin{aligned} T^{\tau\tau} &= \epsilon_x + \epsilon_y + \epsilon_\eta = \epsilon \\ T^{ii} &= -\epsilon_i + \epsilon_j + \epsilon_\eta \Big|_{\substack{i=x,y \\ j\neq i}} \\ \tau^2 T^{\eta\eta} &= \epsilon_x + \epsilon_y - \epsilon_\eta. \end{aligned} \tag{4.57}$$

The pressure to energy ratios are given by,

$$\begin{aligned} \frac{P_L}{\epsilon} &= \frac{\tau^2 T^{\eta\eta}}{T^{\tau\tau}} \\ \frac{P_\perp}{\epsilon} &= \frac{T^{xx} + T^{yy}}{2T^{\tau\tau}}. \end{aligned} \tag{4.58}$$

In the plot shown here, P_L, P_T, and ϵ are all volume integrated quantities, meaning the comparison is a global, not local, one. As can be seen in Fig. (4.10), the $\tau \to 0^+$ limit is quite different in 2+1D and 3+1D,

$$\lim_{\tau\to 0^+} \frac{P_L}{\epsilon} = \begin{cases} \frac{\epsilon_x+\epsilon_y}{\epsilon_x+\epsilon_y} = 1 & \text{in 3+1D} \\ \frac{-\epsilon_\eta}{\epsilon_\eta} = -1 & \text{in 2+1D} \end{cases} \tag{4.59}$$

$$\lim_{\tau\to 0^+} \frac{P_\perp}{\epsilon} = \begin{cases} \frac{\epsilon_\eta}{\epsilon_x+\epsilon_y} = 0 & \text{in 3+1D} \\ \frac{\epsilon_\eta}{\epsilon_\eta} = 1 & \text{in 2+1D.} \end{cases} \tag{4.60}$$

The intersection of the pressures necessarily occurs at $\epsilon/3$, the condition for pressure isotropy, due to the tracelessness of $T^{\mu\nu}$. The pressure does not remain isotropic, however, and approaches the 2+1D asymptotic behavior for large τ, as the longitudinal pressure free-streams towards zero in both cases. The 3+1D approaches the free-streaming condition of $P_\perp/\epsilon = \frac{1}{2}$ much more slowly than the 2+1D case.

The difference in pressure and field evolution affects the development of pre-equilibrium flow, and also likely affects the sensitivity to the hydrodynamic switching time, something that would be interesting to study in more detail. Figure (4.11) shows how the 3+1D implementation affects the development of pre-equilibrium flow. As can be seen, in both cases the transverse flow starts low and builds over time. The longtiudinal flow is actually

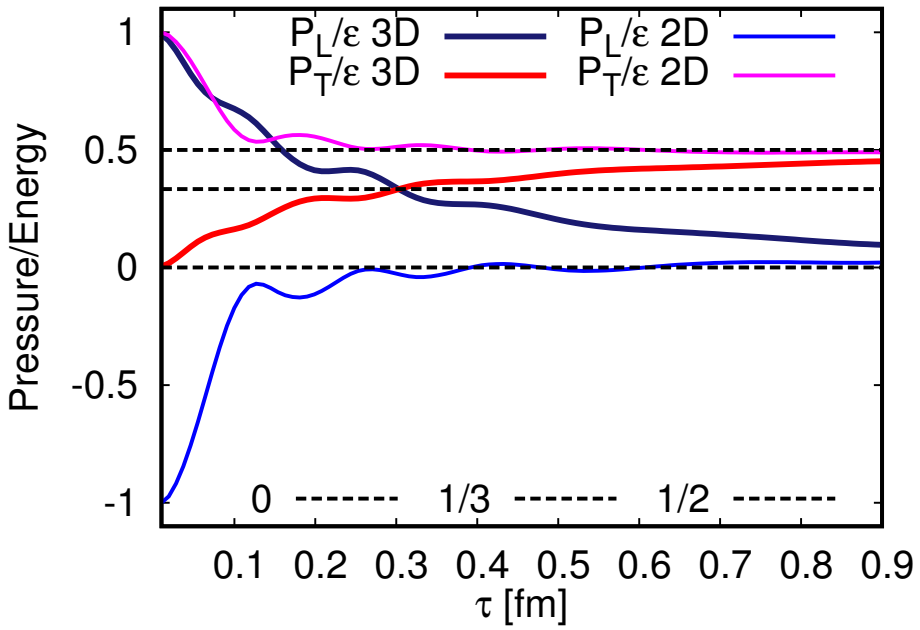

Figure 4.10: Comparison of the transverse and longitudinal pressures in the 2+1D and 3+1D IP-Glasma formulations. Both results are computed using the same 3+1D software, but with the initial 2+1D and 3+1D setups, respectively.

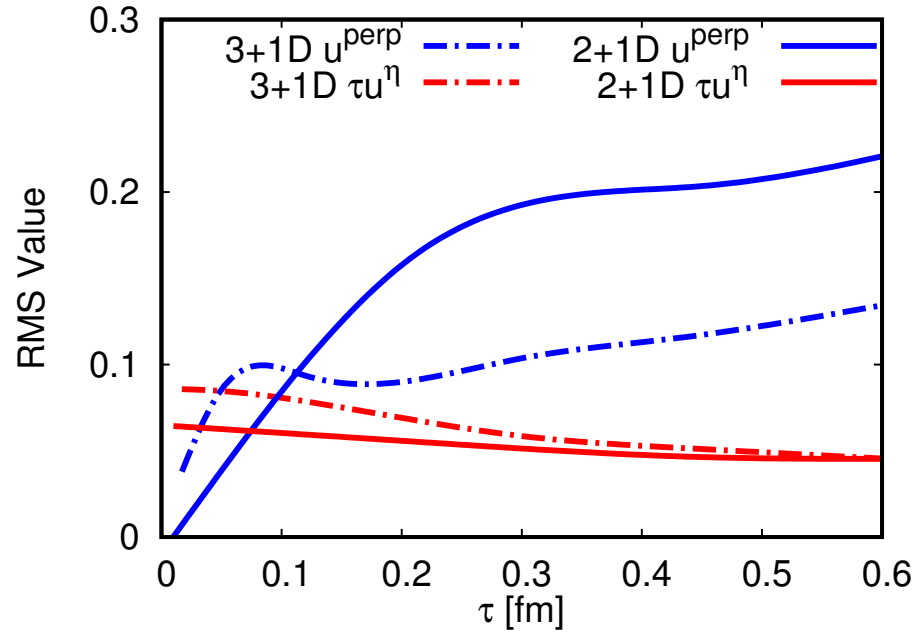

Figure 4.11: RMS flow components as a function of τ for typical events in the $0-5\%$ centrality bin in 2+1D and 3+1D. Both the 2+1D and 3+1D simulations were run using the same 3+1D software, in the appropriate modes.

rather similar in both cases. The transverse flow, on the other hand, takes much longer to build. This is likely due to the fact that the transverse pressure, relative to the energy, is smaller in 3D, compared to 2D, over the entire time interval depicted in Fig. (4.10).

4.8 Recovering the 2D Limit: A Subtle Question

The existing paradigm in the field is the 2+1D glasma picture, which differs substantially from the 3+1D picture just described. The natural question, given such differences in the fields and pressure between the 2+1D and 3+1D scenarios, is whether the 3+1D case can recover the 2+1D physics in the appropriate limit. This is a subtle question and it is not clear whether or not the 3+1D case should reduce nicely to the 2+1D case at all.

There has been a long-held understanding of the negative longitudinal pressure in the early time evolution of the glasma, often analogized by comparing the nuclei to two capacitor plates pulling away from one another. It is clear, however, that the 3+1D initialization leads to positive longitudinal pressure at early times after the collision. This corresponds to the system being pushed apart rather than held together by the longitudinal pressure at early times.

It is hard to provide physical motivation for these two scenarios simultaneously. In order to recover the 2+1D fields, the energy density in the transverse fields would have to go to zero as the energy goes to infinity. In our formulation, this will only happen if the η-derivatives goes to zero faster than τ_0 goes to zero. Taking the infinite momentum limit will eventually "turn off" the JIMWLK evolution because the running coupling will go to zero. The α_s dependence of the JIMWLK evolution can be written as

$$V_x(Y + dY) = \exp\left(i\sqrt{\alpha_s}[...]\right) V_x(Y) \exp\left(-i\sqrt{\alpha_s}[...]\right) \tag{4.61}$$

Expanding the exponential to linear order, and substituting the logarithmic beam energy dependence of α_s

$$\begin{aligned} V_x(Y + dY) &\approx (1 + i\sqrt{\alpha_s} + ...)[...]V_x(Y)(1 - i\sqrt{\alpha_s} + ...)[...] \\ &\approx (1 + i\sqrt{\frac{1}{\ln s}} + ...)[...]V_x(Y)(1 - i\sqrt{\frac{1}{\ln s}} + ...)[...] \\ &\approx V_x(Y) + \mathcal{O}(\frac{1}{\ln s}) \end{aligned} \tag{4.62}$$

This means that the JIMWLK evolution, and thus the rapidity derivatives, "turn off" as $\lim_{s\to 0}$ like $1/\ln(s)$. Simultaneously, the factor $\frac{1}{\tau_0}$ in front of the terms involving the transverse fields in the Hamiltonian will grow, because $\frac{1}{\tau_0} \propto \sqrt{s}$. It is clear that this competition is won by the $\frac{1}{\tau_0}$ term, and so the boost invariant initial energy composition will never be recovered in this setup.

This question, whether the derivatives in η or the $\frac{1}{\tau_0}$ term goes to zero quicker, is never explicitly considered in the 2D derivation. Rather, the 2D derivation implicitly assumes that the derivatives goes to zero quicker. As a reminder, in the 2D case the equations of motion are formulated as rapidity independent, and this rapidity independence is used as justification for setting the initial transverse fields to zero, without explicitly considering the $\frac{1}{\tau_0}$ factors. This is the opposite of what we find in the rapidity dependence of our 3D formulation using the physically motivated JIMWLK evolution. Thus, unless it is shown that this implicit assumption of the boost invariant derivation is correct, there is no reason to expect the 3D implementation to recover the 2D case in the infinite beam energy limit. In this case, the purely longitudinal flux tube picture is simply an artifact of the assumption made in the 2D derivation.

5

Constructing $T^{\mu\nu}$ and Matching to Hydro

5.1 Matching to Hydrodynamics

After the IP-Glasma simulation is over, it is passed to relativistic viscous hydrodynamics. In order to do so, the stress-energy tensors of the two theories, Classical Yang-Mills, and relativistic hydrodynamics, are matched. The Classical Yang-Mills stress energy tensor is given by [33]

$$T^{\mu\nu} = \mathrm{Tr}\left(-g^{\mu\alpha}g^{\nu\beta}g^{\gamma\delta}F_{\alpha\gamma}F_{\beta\delta} + \frac{1}{4}g^{\mu\nu}g^{\alpha\gamma}g^{\beta\delta}F_{\alpha\beta}F_{\gamma\delta}\right) \tag{5.1}$$

This stress energy tensor is symmetric and gauge invariant and is often referred to as the *improved* stress energy tensor. This is to distinguish it from what is usually referred to as the *canonical* stress energy tensor, which can be found from the Langrangian using Noether's Theorem. The improved stress energy tensor can be obtained by adding an anti-symmetric divergence term, sometimes called a superpotential term, to the canonical form, details on which can be found here [82].

Once the stress-energy tensor is constructed, it can be diagonalized to obtain the hydrodynamic fields ϵ and u^μ

$$T^\mu_\nu u^\nu = \epsilon u^\mu. \tag{5.2}$$

The timelike eigenvector is taken and the flow velocity is normalized to $u_\mu u^\mu = 1$. The stress energy tensor for viscous hydrodynamics can be written

$$\begin{aligned} T^{\mu\nu} &= \epsilon u^\mu u^\nu - (P+\Pi)(g^{\mu\nu} - u^\mu u^\nu) + \pi^{\mu\nu} \\ &= T^{\mu\nu}_{\mathrm{ideal}} - \Pi(g^{\mu\nu} - u^\mu u^\nu) + \pi^{\mu\nu} \end{aligned} \tag{5.3}$$

where

$$T^{\mu\nu}_{\mathrm{ideal}} = (\epsilon + P)u^\mu u^\nu - Pg^{\mu\nu} \tag{5.4}$$

and ϵ is the local energy density, u^μ is the flow velocity, P is the pressure, Π is the bulk pressure, and $\pi^{\mu\nu}$ is the viscous stress tensor. Thus, when matching to hydro, the following quantities need to be initialized:

1. Local energy density - ϵ
2. Flow velocity - u^μ
3. Pressure - P (given by EoS $P(\epsilon)$)
4. Shear stress tensor - $\pi^{\mu\nu}$
5. Bulk pressure - Π

The equation of state (EoS), which relates the energy density and the pressure $P(\epsilon)$, closes the system of equations, making it possible to reconstruct the hydrodynamic stress-energy tensor (Eq. 5.3). In this work, the lattice QCD EoS from the HotQCD Collaboration is used [17]. Historically, only the ideal part, Eq. (5.4), has been used when matching IP-Glasma to hydrodynamic simulations, neglecting the viscous components.

More recently, there have been studies that include the full IP-Glasma $T^{\mu\nu}$ [83]. By doing so, one conserves energy and momentum in switching from the CYM evolution to hydrodynamics. The shear stress tensor can be found by taking the difference between the ideal hydro stress-energy tensor and that of IP-Glasma (here called CYM),

$$\pi_0^{\mu\nu} = T^{\mu\nu}_{\mathrm{CYM}} - T^{\mu\nu}_{\mathrm{ideal}} \tag{5.5}$$

since Classical Yang-Mills is a conformal theory for which the bulk pressure vanishes ($\Pi = 0$). There is, however, a discontinuity in the equation of state between CYM and the Lattice EoS used in hydro. Due to the conformality of CYM, $\epsilon = 3P$ and $\Pi = 0$. On the other hand, when the energy density ϵ is passed to the hydrodynamic simulation, the EoS produces a pressure that is in general different from that on the CYM side. The discontinuity of the pressure during the matching gives the initial bulk pressure,

$$P_{\mathrm{CYM}} - P_{\mathrm{hydro}} = \epsilon/3 - P_{\mathrm{LatticeEoS}}(\epsilon) = \Pi_0 \tag{5.6}$$

This arises in the numerical simulations because, in switching between IP-Glasma and hydrodynamics, the equation of state abruptly transitions from a purely gluonic system to a locally equilibrated system of quarks and gluons comprising the Quark Gluon Plasma. The mechanism that brings the purely gluonic system of strong classical fields to the point of hydrodynamic applicability is not well understand but important work has been done applying QCD kinetic theory to explore this phase of the evolution [84].

5.2 Hydrodynamics

Hydrodynamics is a long wavelength effective theory that evolves average thermodynamic quantities such as temperature and pressure. The validity of hydrodynamics relies on a separation of microscopic and macroscopic scales. One way to gauge the validity of hydrodynamics is via the Knudsen number, defined as

$$K = \frac{\lambda_{mfp}}{L_{hydro}} \tag{5.7}$$

where λ_{mfp} is the mean free path of the microscopic particles, and L_{hydro} is the macroscopic length scale of the system, often taken to be the inverse of the scalar expansion rate of the system

$$L_{hydro} = \frac{1}{\Theta} = \frac{1}{\partial_\mu u^\mu}. \tag{5.8}$$

Hydrodynamics is usually considered applicable when the Knudsen number is below or comparable to one. This condition and the general applicability of hydrodynamics has been pushed in the context of Quark Gluon Plasma in recent years as experimental evidence for collective behavior in small systems has been observed and hydrodynamic modelling has found success in these systems [85] that had previously been thought to be outside the realm of applicability of hydrodynamics.

The hydro attractor framework [86, 24] argues that hydrodynamics is applicable in far from equilibrium systems because the so-called "non-hydrodynamic" modes decay exponentially and the system relaxes to a "hydro attractor" solution. The realm of applicability of hydrodynamics in heavy ion collision is contested, and remains an active area of research. In order to be conservative, this thesis only considers hydrodynamic simulations for A-A

collisions below 50% centrality which are widely accepted to be within the applicability of hydrodynamics.

The hydrodynamic equations of motion are conservation equations for the energy and momentum plus any additional conservation laws for conserved currents. In the language of the stress-energy tensor,

$$\partial_\mu T^{\mu\nu} = 0 \tag{5.9}$$

Ideal hydrodynamics, without any additional conserved currents, has 5 independent fields: the energy density in the local rest frame ϵ, the thermodynamic pressure P, and the local flow velocity u^μ, where the condition $u^\mu u_\mu = 1$ means there are only three independent flow components. Explicitly,

$$u^\mu = \frac{1}{\sqrt{1-\mathbf{v}^2}} \begin{pmatrix} 1 \\ \mathbf{v} \end{pmatrix} = \gamma \begin{pmatrix} 1 \\ \mathbf{v} \end{pmatrix} \tag{5.10}$$

and thus,

$$u^\mu u_\mu = u^\mu g_{\mu\nu} u^\nu = \gamma^2(1-\mathbf{v}^2) = 1. \tag{5.11}$$

The four equations in (5.9) along with the equation of state, close the system of equations. Here the choice of u^μ is the Landau-Lifshitz frame, whereby the flow is defined by the flow of energy. Another possible choice that is usually mentioned is the Eckart frame, in which the flow velocity is defined by the charge current.

In MUSIC [30], the relativistic hydrodynamics code used in this thesis, the viscous terms, $\pi^{\mu\nu}$ and Π, evolve according to their own relaxation-time type equations:

$$\dot{\Pi} = \frac{1}{\tau_\Pi}(-\Pi - \zeta\Theta - \delta_{\Pi\Pi}\Pi\Theta + \lambda_{\Pi\pi}\pi^{\mu\nu}\sigma_{\mu\nu}) \tag{5.12}$$

$$\dot{\pi}^{\langle\mu\nu\rangle} = \frac{1}{\tau_\pi}(-\pi^{\mu\nu} + 2\eta\sigma^{\mu\nu} - \delta_{\pi\pi}\pi^{\mu\nu}\Theta + \phi_7\pi_\alpha^{\langle\mu}\pi^{\nu\rangle\alpha} - \tau_{\pi\pi}\pi_\alpha^{\langle\mu}\sigma^{\nu\rangle\alpha} + \lambda_{\pi\Pi}\Pi\sigma^{\mu\nu}) \tag{5.13}$$

In practice, we tend to only evolve the first three terms on the right hand side of Eq. (5.12) and Eq. (5.13) because the other terms have negligible phenomenological effect. The form of the coefficients are derived in the 14-moment approximation [87], and given by

$$\begin{aligned}
\frac{\delta_{\Pi\Pi}}{\tau_\Pi} &= \frac{2}{3} + O(z^2 \ln z), \\
\frac{\lambda_{\Pi\pi}}{\tau_\Pi} &= \frac{8}{5}\left(\frac{1}{3} - c_s^2\right) + O(z^4) \\
\frac{\lambda_{\pi\Pi}}{\tau_\pi} &= \frac{6}{5} + O(z^2), \\
\delta_{\pi\pi} &= \frac{4}{3}\tau_\pi, \\
\tau_{\pi\pi} &= \frac{10}{7}\tau_\pi, \\
\phi_7 &= \frac{9}{70 P_0}
\end{aligned} \tag{5.14}$$

where $z = m/T$ is the ratio of the mass of the particle to the temperature, c_s is the speed of sound, and P_0 is the thermodynamic pressure. As the QGP evolves hydrodynamically, it expands and cools until it reaches the temperature at which the QGP will turn back into hadrons, or "hadronize." The hydrodynamical simulation evolves until it reaches a 4-dimensional constant-temperature surface, often called a "hyper-surface." From this hyper-surface, particles are sampled from a thermal distribution using the Cooper-Frye formalism [88].

The exact temperature at which to switch from a hydrodynamic description to a hadron gas description is informed by lattice QCD calculations, but it is usually taken to be a parameter phenomenologically. For the purposes of this thesis, this temperature is taken to be $T_{sw} = 145\,\text{MeV}$. Phenonemologically, the quantity that tends to be the most sensitive to the choice of T_{sw} is the proton multiplicity [89], and to a lesser degree, the proton $\langle p_T \rangle$, and the choice of T_{sw} is chosen primarily in order to find agreement with these quantities. The proton multiplicity is sensitive to the switching temperature because ones samples a thermal distribution for the particles, and if the temperature is too low, it becomes very unlikely to sample a heavy particle like a proton.

5.3 Cooper-Frye Freezeout

In the following, we will briefly describe the procedure of switching from hydrodynamics to hadronic degrees of freedom, closely following the discussion outlined in [89].

In order to transition from a hydrodynamic medium where one only has fluid cells, to a hadronic gas where the degrees of freedoms are hadrons, one must match the fluid dynamics $T^{\mu\nu}_{hydro}$ with that of a hadron gas governed by kinetic theory, $T^{\mu\nu}_{hadron\,gas}$. Using the notation of [90]

$$T^{\mu\nu}_{kinetic} = \sum_i d_i \int \frac{d^4p}{(2\pi)^3}\delta(p^\mu p_\mu - m_i^2)2\theta(p^0)p^\mu p^\nu f(p,x) = T^{\mu\nu}_{hydro} \tag{5.15}$$

where the sum is over particle species, and d_i represents the particle degeneracy. The single particle distribution function, $f(\mathbf{p},\mathbf{x})$, represents the phase space density of on-shell particles,

$$f(\mathbf{p},\mathbf{x}) \propto \frac{dN}{d^3pd^3x}. \tag{5.16}$$

The transition from hydrodynamics to hadron gas should happen when the mean free path is no longer sufficiently small compared to the macroscropic scale of the system, given by the expansion rate in the last section. By insufficient, we mean that the interactions are no longer strong enough to keep the system close to local thermal equilibrium, meaning that hydrodynamics is no longer applicable.

It can be shown that the number of particles crossing a hypersurface is given by the Cooper-Fry formula

$$\frac{dN}{d^3\mathbf{p}} = \frac{d}{(2\pi)^3}\int_\Sigma \frac{p^\mu d^3\Sigma_\mu}{E_\mathbf{p}} \times [f_0(x,\mathbf{p}) + \delta f_{shear}(x,\mathbf{p}) + \delta f_{bulk}(x,\mathbf{p})] \tag{5.17}$$

where d is a degeneracy factor, $d\Sigma_\mu$ is the normal vector to the 4-dimensional constant temperature hypersurface, δf_{shear} is a shear viscous correction [91] to the single particle distribution function, and δf_{bulk} [92, 93] is a correction due to the bulk viscosity. Assuming the momentum distribution is isotropic in the local rest frame, one can take the single particle momentum distribution at a temperature T, and with local flow velocity u^μ to be either a Bose of Fermi distribution,

$$f_0 = \frac{1}{\exp\left(p\cdot u/T\right) \mp 1}. \tag{5.18}$$

In order to sample the number of particles in each cell from the Cooper-Frye formula 5.17, a Poisson distribution with average value,

$$\bar{N}|_{1-cell} = \begin{cases} [n_0(x) + \delta n_{bulk}(x)]u^\mu\Delta\Sigma_\mu & \text{if} \quad u^\mu\Delta\Sigma_\mu \geq 0 \\ 0 \qquad \text{otherwise} \end{cases} \tag{5.19}$$

is used, where

$$\begin{aligned} n_0(x) &= d\int \frac{d^3\mathbf{k}}{(2\pi)^3} f_0(x,\mathbf{k}) \\ \delta n_{bulk}(x) &= d\int \frac{d^3\mathbf{k}}{(2\pi)^3} \delta f_{bulk}(x,\mathbf{k}). \end{aligned} \tag{5.20}$$

This has been tested to adequately reproduce the Cooper-Frye particle number for hydrodynamic calculations with 135MeV $\leq T_{sw} \leq$ 165MeV despite small error arising from the non-Poisson nature of the quantum thermal distributions [89].

Once the number of particles in a cell is determined, the momentum of each particle is sampled according to

$$\frac{dN}{d^3\mathbf{p}}|_{1-cell} = \begin{cases} \frac{d}{(2\pi)^3}[f_0 + \delta f_{shear} + \delta f_{bulk}]\frac{p^\mu \Delta\Sigma_\mu}{E_\mathbf{p}} & \text{if} \quad (f_0 + \delta f_{shear} + \delta f_{bulk}) > 0, \quad p^\mu \Delta\Sigma_\mu > 0 \\ 0 \qquad \text{otherwise} \end{cases} \tag{5.21}$$

Again, this procedure has been tested [89] to adequately reproduce the particle spectra from the Cooper-Frye procedure, particularly for particles with $p_T < 5\,\text{GeV}$.

5.4 UrQMD

Once the number of particles, and their momenta, are sampled, they are evolved using UrQMD [6]. UrQMD propagates the hadrons along classical trajectories, allowing for stochastic binary collisions between hadrons, color string formation, and resonance decays [94]. It is, in effect, a Monte-Carlo evolution of the the phase space densities $f_i(x,p)$, where i labels the particle species, via the relativistic Bolzmann equation,

$$p^\mu \partial_\mu (x^\nu, p^\nu) = \mathcal{C}_i \tag{5.22}$$

where $\mathcal{C}_i$ is the collision term. UrQMD treats cross-sections geometrically, meaning that a collision occurs if

$$d < \sqrt{\sigma_{tot}/\pi} \tag{5.23}$$

where $\sigma_{tot}(\sqrt{s}, \text{species})$ is the total cross-section that depends on the hadron species and center of mass energy $\sqrt{s}$, and d is their impact parameter. It is sometimes described as

treating the hadrons as "billiard balls," in terms of scattering. Once a collision is determined to occur by this geometric criterion, the specific outcome of the collision is sampled according to the probability of each outcome, and the angular distribution is determined by $\frac{d\sigma}{d\Omega}$. If experimental data for a given cross-section is available, that value is used. Otherwise the additive quark model and arguments using detailed balance are used. UrQMD only treats $2 \rightarrow 2$ scatterings and neglects long range two-body forces such as the Coulomb force. UrQMD also includes resonance decays.

5.5 The 3D IP-Glasma Cookbook

Now that the physics of 3D IP-Glasma has been outlined, it is useful to give a practical summary of how to construct the numerical simulation in broad strokes. Hopefully, this will orient the reader to the sequence of computation that is necessary, and serve as a useful structure to understand the details of the calculation.

1. Sample the position of nucleons from a Wood-Saxon,

$$\rho(r)dr = \frac{r^2 dr}{1 + \exp\left((r - R)/a\right)} \tag{5.24}$$

   Alternatively, use a pre-calculated configurations of nuclei that include nucleon-nucleon correlations [95].

2. Sample impact parameter from

$$P(b)db = \frac{2b}{b_{max}^2 - b_{min}^2} db \tag{5.25}$$

   and shift nucleus A by $b/2$ and nucleus B by $-b/2$ in the x-direction.

3. Construct nuclear thickness functions by summing contributions from individual nucleons

$$T_{(\text{nucleus})}(\mathbf{x}) = \sum_{i=1}^{A} \frac{1}{2\pi B_G} e^{((\mathbf{x}-\mathbf{x_i})^2/2B_G)} \tag{5.26}$$

   where $\mathbf{x_i}$ is the location of the i^{th} nucleon.

4. Compute Q_s^2 at $\pm y_{max}$ via IP-Sat

$$\frac{\pi^2}{N_c}\alpha_s(\mu^2(r^2))xg(x,\mu^2(r^2))T(b)r_s^2 = 1 \tag{5.27}$$

where $Q_s^2 = \frac{1}{r_s^2}$.

5. Sample color charge density from

$$\langle \rho^a_{A(B)}(\mathbf{x}_\perp)\rho^b_{A(B)}(\mathbf{y}_\perp)\rangle = g^2\mu^2_{A(B)}(x,\mathbf{x}_\perp)\delta^{ab}\delta^2(\mathbf{x}_\perp - \mathbf{y}_\perp) \tag{5.28}$$

where $Q_s = Cg^2\mu$. The proportionality constant is taken to be $C \approx 0.5$-0.75 in 2D but $C \approx 1.3$-1.4 in 3D.

6. Solve Poisson equation,

$$\nabla_\perp^2 A^a = -\rho^a \tag{5.29}$$

The numerical solution is given in Section 8.1.

7. Construct Wilson Lines at $\pm Y_{max}$

$$V(\mathbf{x},\pm Y_{max}) = \prod_{i=1}^{N_y}\exp\left(-ig\frac{\rho_a^i(\mathbf{x})t^a}{\nabla^2 - m^2}\right) \tag{5.30}$$

8. Evolve Wilson lines at $\pm Y_{max}$ to $\mp Y_{max}$ using JIMWLK equations

$$\begin{aligned} V_{A,B}(\mathbf{x},Y+dY) = \exp\left(-i\frac{\sqrt{\alpha_s dY}}{\pi}\int_{\mathbf{z}}\mathbf{K}_{\mathbf{x}-\mathbf{z}}\cdot V_z\xi_z V_z^\dagger\right) \\ \times V_{A,B}(\mathbf{x},Y)\times\exp\left(i\frac{\sqrt{\alpha_s dY}}{\pi}\int_{\mathbf{z}}\mathbf{K}_{\mathbf{x}-\mathbf{z}}\cdot\xi_z\right) \end{aligned} \tag{5.31}$$

9. Construct pure gauge fields for each nucleus

$$A_\mu^{A(B)} = \frac{-i}{g}V^{A(B)}\partial_\mu V^{A(B)\dagger} \tag{5.32}$$

10. Solve initial gauge field problem

$$\begin{aligned} A_\mu &= A_\mu^{(A)} + A_\mu^{(B)} \\ E^\eta &= ig[A_i^{(A)}, A_i^{(B)}] \end{aligned} \tag{5.33}$$

11. Solve Gauss' Law problem using ansatz

$$\begin{aligned} E^i &= [D^i, \phi] \\ [D_i, [D^i, \phi]] &= \rho \end{aligned} \tag{5.34}$$

12. Evolve using the sourceless CYM equations of motion, written for simplicity as,

$$[D_\mu, F^{\mu\nu}] = 0 \tag{5.35}$$

13. Construct $T^{\mu\nu}$

$$T^{\mu\nu} = -g^{\mu\alpha} g^{\nu\beta} g^{\gamma\delta} F_{\alpha\gamma} F_{\beta\delta} + \frac{1}{4} g^{\mu\nu} g^{\alpha\gamma} g^{\beta\delta} F_{\alpha\beta} F_{\gamma\delta} \tag{5.36}$$

14. Diagonalize T^μ_ν

$$T^\mu_\nu u^\nu = \epsilon u^\mu. \tag{5.37}$$

15. Construct ideal and viscous components of hydrodynamics stress tensor to initialize the hydrodynamic evolution.

6

Description of Observables and Results

6.1 Introduction

The boost invariant IP-Glasma was able to describe a wide range of transverse observables in heavy ion collisions when used to initialize relativistic hydrodynamics simulations. Before moving onto longitudinal observables, it is necessary to explore how well the 3+1D formulation is able to describe the transverse dynamics of heavy ion collisions.

To be clear, there are several parameters that can be tuned, including the hydrodynamics transport coefficients, to achieve agreement with data, and the values used here do not correspond precisely to the values typically used for the boost invariant formulation. The goal is to show that the 3+1D formulation is able to describe the transverse physics of heavy ion collisions at mid-rapidity while using parameter values that are consistent with our broader physical understanding of these parameters, but not to make a one-to-one comparison between the 2+1D and 3+1D results and parameters.

The current work did not control for all differences between the 2D and 3D simulations to isolate the features of making the model 3+1D but rather sought to implement the physics in the best possible way in this work, making several implementation improvements over the 2+1D version with which we will make a comparison [45].

For example, the momentum fraction x that is used to determine the saturation scale was taken to be constant for a given beam energy in [45]. It this work, however, x and Q_s depend on each other and are solved iteratively, according to Eq. (2.25) $x = Q_s/(\sqrt{s}/2)$. As argued elsewhere, this has the effect of flattening the multiplicity distribution because a small x value will typically lead to a large Q_s which will result in a larger x, etc.

Additionally, instead of sampling a Wood-Saxon for the nucleon position, as done in [45], the nucleon positions are taken from pre-calculated Pb nuclei that include nucleon-nucleon correlations, taken from [95]. To mention one final parameter difference, the infrared regulator used in the Poisson equation is chosen as $m_{reg} = 0.4\,\mathrm{GeV}$ to match that used in the JIMWLK kernel, but differs from what was used in [45], where $m_{reg} = 0.2\,\mathrm{GeV}$ was used. Finally, in [45], only the ideal components of $T^{\mu\nu}$ were used to initialize the hydrodynamic evolution, whereas the whole $T^{\mu\nu}$ including the viscous components were used in this thesis. With these differences in mind, it is nonetheless useful to briefly compare the initial state in 3+1D to the boost invariant implementation [45] for reference.

6.2 Comparison of 2D and 3D Initial States

6.2.1 Centrality Selection

In order to compare with experimental data, which is often categorized into centrality classes, it is important to carry out a centrality selection of our own. Centrality is generally understood to correspond to impact parameter: small impact parameter correponds to small centralities ("central collisions") and large centralities correspond to large impact parameter ("peripheral collisions"). However, experimentally the impact parameter is unknown, and centrality is determined by the multiplicity or energy in an event. Our centrality selections adheres as closely to the experimental procedure as possible, in which we bin events on charged hadron multiplicity $dN_{ch}/d\eta$. In doing so, we take two parameters: 1) the energy that constitutes a collision and 2) the overall energy normalization, fit to the 0-5% centrality bin. The result is the charge hadron multiplicity that agrees with the experimental data, as shown in Fig. (6.1).

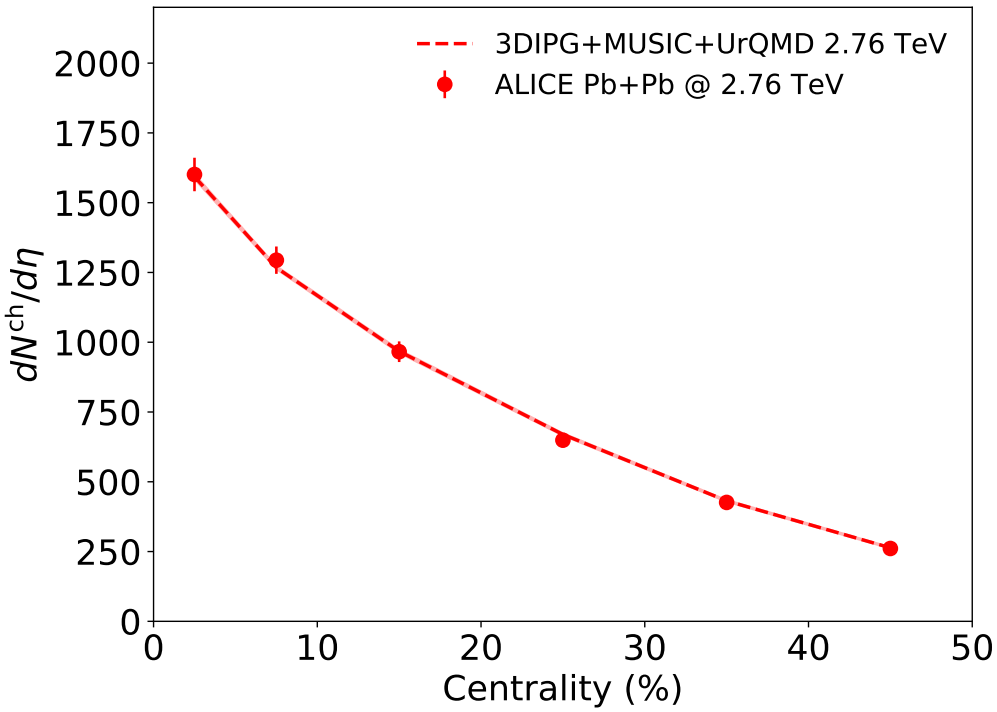

Figure 6.1: The charged hadron multiplicity as a function of centrality for $\sqrt{s} = 2.76\,\text{TeV}$. This figure validates the centrality selection process discussion in this section. ALICE data is from [96].

6.2.2 Comparison of 2D and 3D Initial State Quantities

Although the initial state is not observable experimentally, the hydrodynamic evolution is sensitive to it. Thus, by quantitatively comparing initial state models and understanding their effects on the hydrodynamic evolution and final state particle spectra, it is possible to deduce features of the initial state of heavy ion collisions.

The initial state geometry, as characterized by the position space anisotropies (ϵ_n's),

$$\epsilon_n(\eta) = \frac{\int d^2x r^n \varepsilon(\mathbf{x}_\perp, \eta) e^{in\phi}}{\int d^2x r^n \varepsilon(\mathbf{x}_\perp, \eta)}. \tag{6.1}$$

where $\varepsilon(\mathbf{x}_\perp, \eta)$ is the local energy density, is converted to momentum space anisotropies (v_n's) by the hydrodynamic evolution. Figure 6.2, panel (a) shows ϵ_n for $n = 2, 3, 4$ for both 2+1D and 3+1D IP-Glasma as a function of centrality. The ϵ_n's do not differ substantially in 3+1D from those in 2+1D, but those of 3+1D are systematically below those in 2+1D for the same

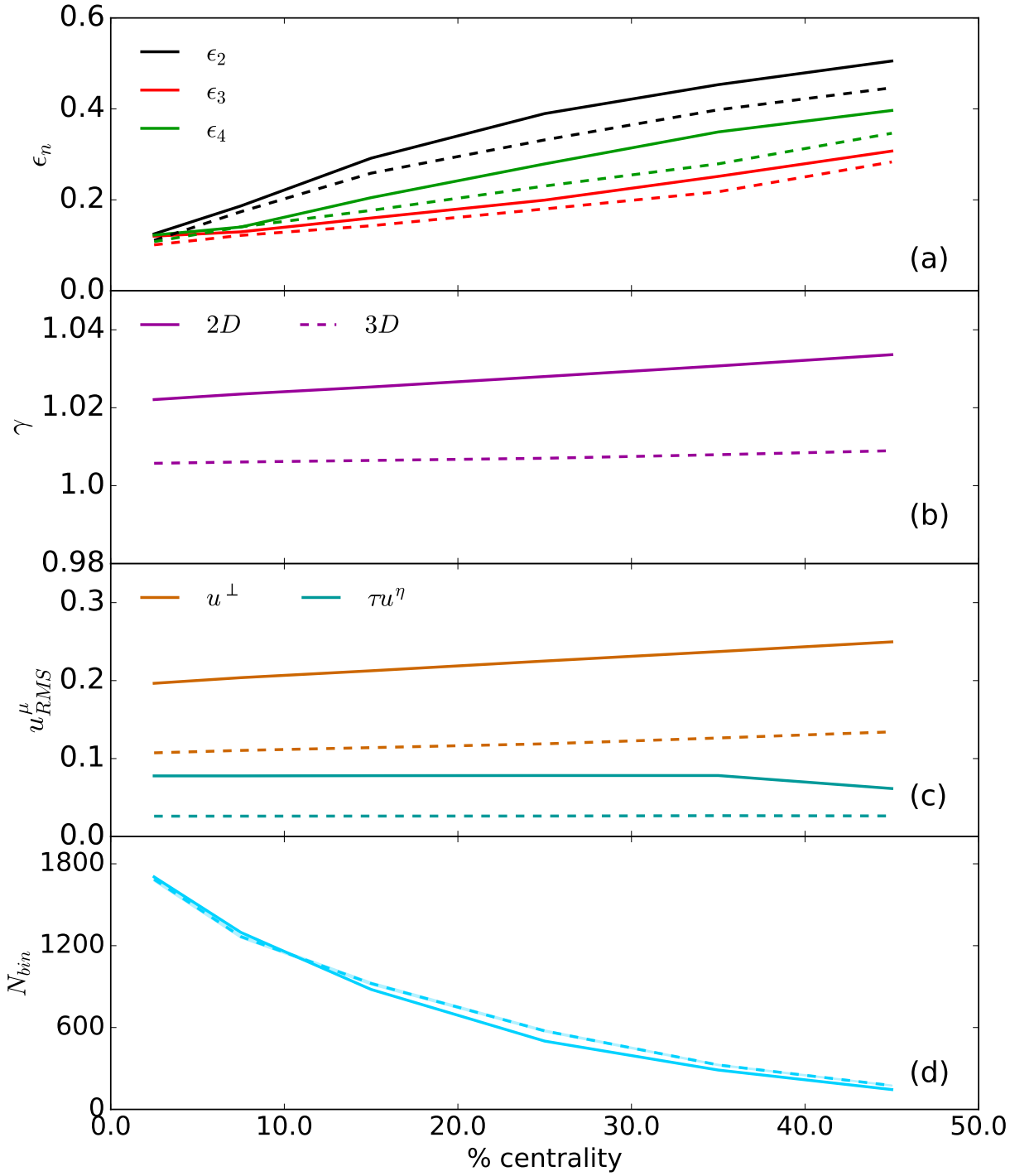

Figure 6.2: Comparison of various initial state quantities between the 3D IP-Glasma events and 2D IP-Glasma events from [45]. Note that the 3D lines are taken at $\tau = 0.6\,\mathrm{fm}$, whereas the 2D lines are taken at $\tau = 0.4\,\mathrm{fm}$, their respective matching times to hydro.

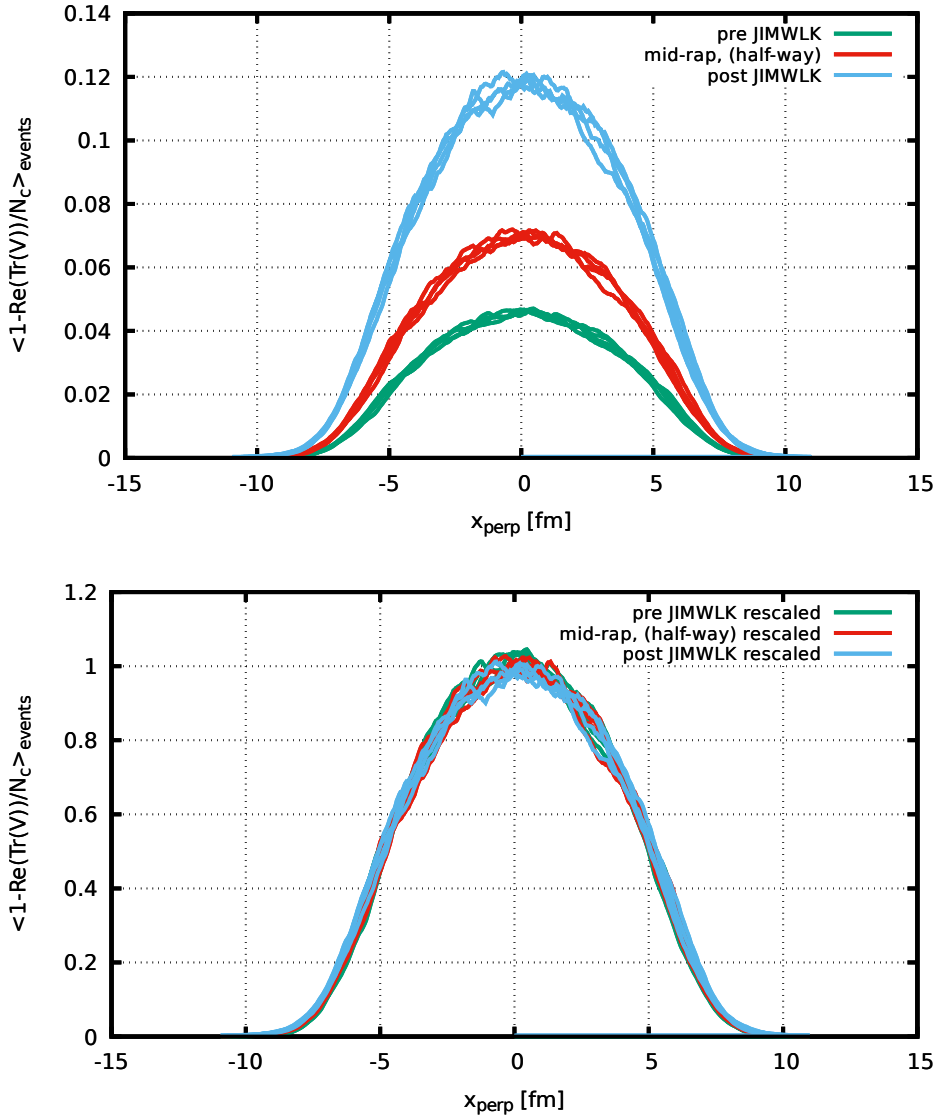

Figure 6.3: The event averaged quantity $\langle 1 - \mathrm{Re}(\mathrm{Tr}(V))/N_c \rangle_{events}$, which can be thought of as a proxy for the gluon density, vs. one of the transverse coordinates, and averaged over many events. It is plotted at three different points in the JIMWLK rapidity evolution. The four different lines for each color simply correspond to the target, projectile, and for the transverse coordinates x, and y. The JIMWLK evolution clearly increases the density of the gluon fields.The bottom panel is the same quantity, except re-scaled to have roughly the same peak height, in order to be able to compare the shapes of the curves. The JIMWLK evolution does not change the average shape or size of the nuclei, only their density.

centrality classes. In panel (d) of this figure, the number of binary collisions N_{bin} is plotted as a function of centrality, and the 2+1D and 3+1D cases differ only mildly, indicating that the centrality selection is similar in the two cases, at least in terms of geometric overlap as indicated by N_{bin}.

Outside of the differences noted in the introduction to this chapter, there are two plausible possibilities for why these quantities could differ due to the additional dimension in 3+1D. Either the JIMWLK evolution or the addition of the initial transverse chromo-electric and chromo-electric fields could alter the shape of the nuclei sufficiently to change the geometry of the overlap regions. In Fig. (6.3) the average density of the pre-collision nuclei are plotted at three different points in the JIMWLK evolution. It is clear from this figure that the JIMWLK evolution increases the density of the nuclei and leads to fluctuations in shape on an event-by-event basis, but does not alter the shape of the nucleus on average, as a function of rapidity. Thus the JIMWLK evolution itself should not alter the eccentricities computed at mid-rapidity much. Regarding the other possibility mentioned, we computed the eccentricities at mid-rapidity using one the initial longitudinal fields, to mimic the 2D case, and compared with the result computed using the full 3D energy density, and there was negligible difference. Thus neither the JIMWLK evolution nor the initial transverse fields substantially alter the geometry of the collisions at mid-rapidity relative to the 2D case. The slight differences in ϵ_n between the 2+1D and 3+1D events are likely due to centrality selection, differences in parameters, and slightly different implementations.

In panels (b) and (c), the energy density weighted root mean square values of the pre-equilibrium flow components are shown. They are defined as

$$u^{\mu}_{RMS} = \sqrt{\langle \frac{\int d^2\mathbf{x}_\perp \epsilon(\mathbf{x}_\perp)(u^\mu)^2}{\int d^2\mathbf{x}_\perp \epsilon(\mathbf{x}_\perp)} \rangle} \tag{6.2}$$

where $\gamma = u^\tau$ for panel (b). The pre-equilibrium flow can play an important role in the final state momentum anisotropy, particularly in small systems. This can affect the values of transport coefficients, such as the shear and bulk viscosities, needed to obtain agreement with experimental data [83]. The 3+1D IP-Glasma generates significantly less pre-equilibrium flow due to the difference in pressure evolution shown in Fig. (4.10). In 3+1D, the transverse pressure is small at the initial time and takes much longer to reach $\sim 0.5\epsilon$, whereas in the

2+1D the initial transverse pressure is large ($\geq 0.5\epsilon$) compared to the energy and remains large throughout the evolution. This leads to substantially more transverse flow in the IP-Glasma phase in 2+1D.

The slightly smaller values for ϵ_n in 3+1D and the significantly smaller pre-equilibrium flow require a smaller value of η/s to obtain values of v_2 that agree with experimental data. With the EOS used in this thesis, the 2D IP-Glasma implemented in [45] requires $\eta/s \approx 0.12$ for Pb-Pb at 2.76 TeV, compared to $\eta/s \approx 0.08$ used for the 3+1D events in this thesis.

6.3 Mid-Rapidity Hadronic Observables

The centrality selection procedure leads to good agreement with the charged hadron multiplicity at mid-rapidity as shown if Fig. (6.1). This is a crucial step in validating the centrality selection, and ensuring that the comparison between experimental and theoretical curves as a function of centrality is a fair one.

The charged hadron p_T-integrated v_n flow harmonics for $n = 2, 3, 4$ are shown in Fig. (6.4). As a reminder, the flow harmonics are the Fourier coefficients of the decomposition of the particle spectra in the the azimuthal angle,

$$\frac{dN}{p_T dp_T dy d\phi} = \frac{dN}{2\pi p_T dp_T dy}\left(1 + \sum_{n=1} 2v_n(y, p_T)\cos\left[n(\phi - \Psi_n)\right]\right). \tag{6.3}$$

where Ψ_n is the reaction plane angle. As suggested by this notation, the flow coefficients $v_n(y, p_T)$ are typically rapidity (y) and transverse momentum (p_T) dependent, and are thus referred to as *differential* flow harmonics. The *integrated* flow harmonics at a given rapidity are given by

$$v_n = \frac{\int_0^\infty v_n(p_T)\frac{dN}{dp_T}dp_T}{\int_0^\infty \frac{dN}{dp_T}dp_T}. \tag{6.4}$$

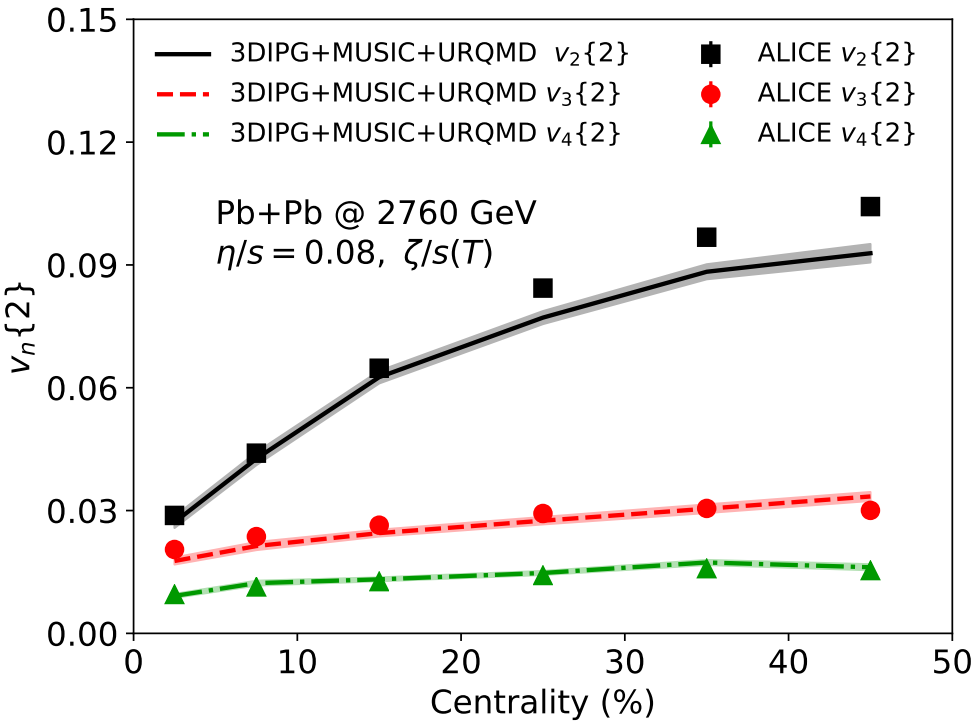

Figure 6.4: The anisotropic flow coefficients v_2, v_3, and v_4 as a function of centrality, compared to ALICE data [41].

There are different methods for computing the v_n flow coefficients. In this thesis, we compute and plot $v_n\{2\}$, following the analysis described in [45] for flow analysis for a finite number of particles. In particular, for each hydrodynamic simulation, $N^{\text{oversampled}}$ UrQMD events are run in order to be able to reduce the fluctuations arising from sampling a finite number of particles from the underlying hydrodynamic event. The flow vector is computed via,

$$\mathbf{Q}_n = \sum_{k=1}^{N^{\text{oversampled}}} \sum_{j=1}^{N^{\text{particles}}} e^{in\phi_j} \tag{6.5}$$

where j runs over all particles in an individual UrQMD event within the specified kinematic cuts, typically taken to match the experimental cuts. The index k runs over all of the UrQMD events that correspond to the same underlying hydrodynamic event, and runs to $N^{\text{oversampled}} = 100$ in this work. From the flow vector, the p_T-differential flow coefficient is

determined with the scalar product method,

$$v_n\{SP\}(p_T) = \frac{\langle\, \mathrm{Re}[\mathbf{Q}_n(p_T)\cdot(\mathbf{Q}_n^{\mathrm{ref}})^*]\rangle_{\mathrm{hydro\,ev}}}{\langle N(p_T)N^{\mathrm{ref}}\rangle_{\mathrm{hydro\,ev}} v_n\{2\}}. \tag{6.6}$$

The two particle cumulant is defined as

$$(v_n\{2\})^2 = \frac{\langle\, \mathrm{Re}[\mathbf{Q_n}\cdot(\mathbf{Q_n})^*]\rangle_{\mathrm{hydro\,ev}}}{\langle N^2\rangle_{\mathrm{hydro\,ev}}}. \tag{6.7}$$

When matching to experimental data for $v_n\{2\}(\eta)$ for which different collaborations use different kinematic cuts for their reference flow vectors,

$$(v_n\{2\}(\eta))^2 = \frac{\langle\, \mathrm{Re}[\mathbf{Q}_n(\eta)\cdot(\mathbf{Q}_n(\eta_{\mathrm{ref}}))^*]\rangle_{\mathrm{hydro\,ev}}}{\langle N(\eta)N(\eta_{\mathrm{ref}})\rangle_{\mathrm{hydro\,ev}}}. \tag{6.8}$$

The differential flow harmonics for $n = 2, 3, 4, 5$ are shown in Fig. (6.5) for the 0-5% and 30-40% centralities, along with the ratios of theoretical data to experimental data. Similar plots are shown for the particle identified spectra in Fig. (6.6). Taken together, these two figures show the key components that factor into the calculation of the integrated flow harmonics, and can be used to understand the varying agreement between experimental data and theoretical curves in terms of the applied kinematic cuts.

The higher harmonics $v_3\{2\}$ and $v_4\{2\}$ agree with the data quite well, while the $v_2\{2\}$ harmonic deviates from experimental data for larger centralities. The level of agreement, however, depends on the p_T range included in the integration, as will be seen in the next section. The comparison in Fig. (6.4) is done for $0.2 < p_T < 3.0\,\mathrm{GeV}$ to match that of the ALICE data.

In Fig. (6.7), the mean transverse momentum at mid-rapidity for protons, kaons, and pions is plotted and good agreement is found. This quantity, particularly for heavier particles such as protons, is sensitive to the bulk viscosity, freeze-out temperature, and hadronic afterburner. In fact, the phenomenological motivation for the inclusion of bulk viscosity is primarily the $\langle p_T\rangle$ of protons. Hydrodynamic models without bulk viscosity describe $\langle p_T\rangle$ of lighter particles, such as pions and kaons, relatively well but the heavier proton is almost always over predicted. This is because the $\langle p_T\rangle$ of protons is more sensitive to the radial flow velocity of the QGP, which is dampened by the bulk viscosity. To see why, consider a fluid cell which describes the flow of a small amount of QGP, with a given velocity. When

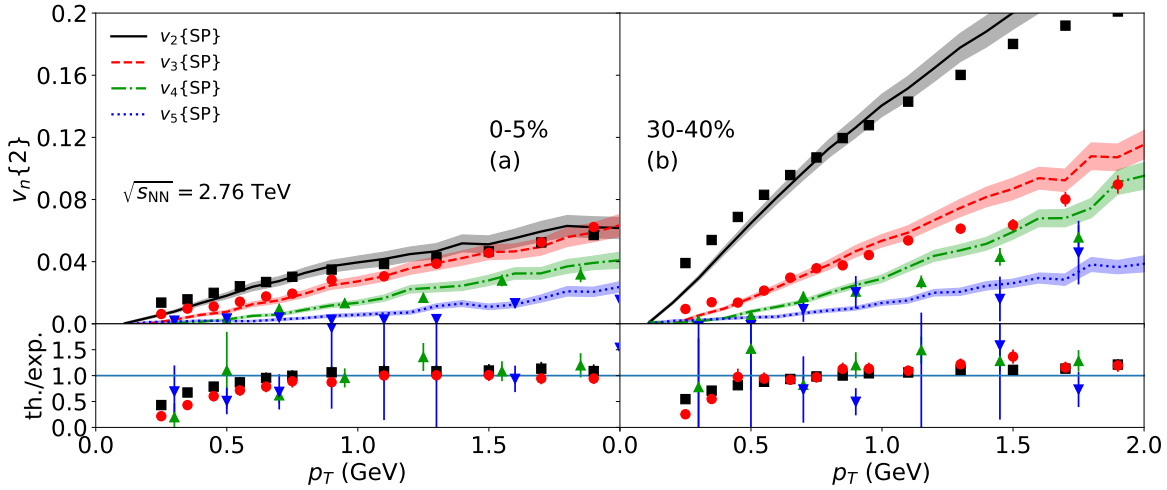

Figure 6.5: Differential flow harmonics $v_n\{2\}(p_T)$ for two centralities, compared to ALICE data. Left upper panel is for 0-5% and right upper panel is 30-40% centrality. Lower panels show the ratio of theoretical data to experimental data from the upper panels.

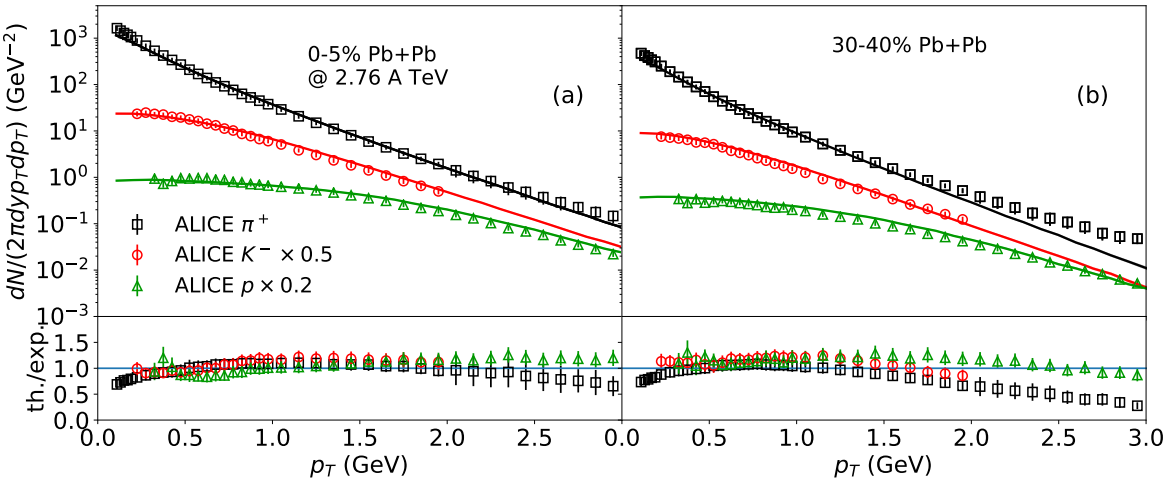

Figure 6.6: Identified particle spectrum for two centralities, compared to ALICE data [97]. The lower panels show the ratio of the theoretical data to the experimental calculation for each curve.

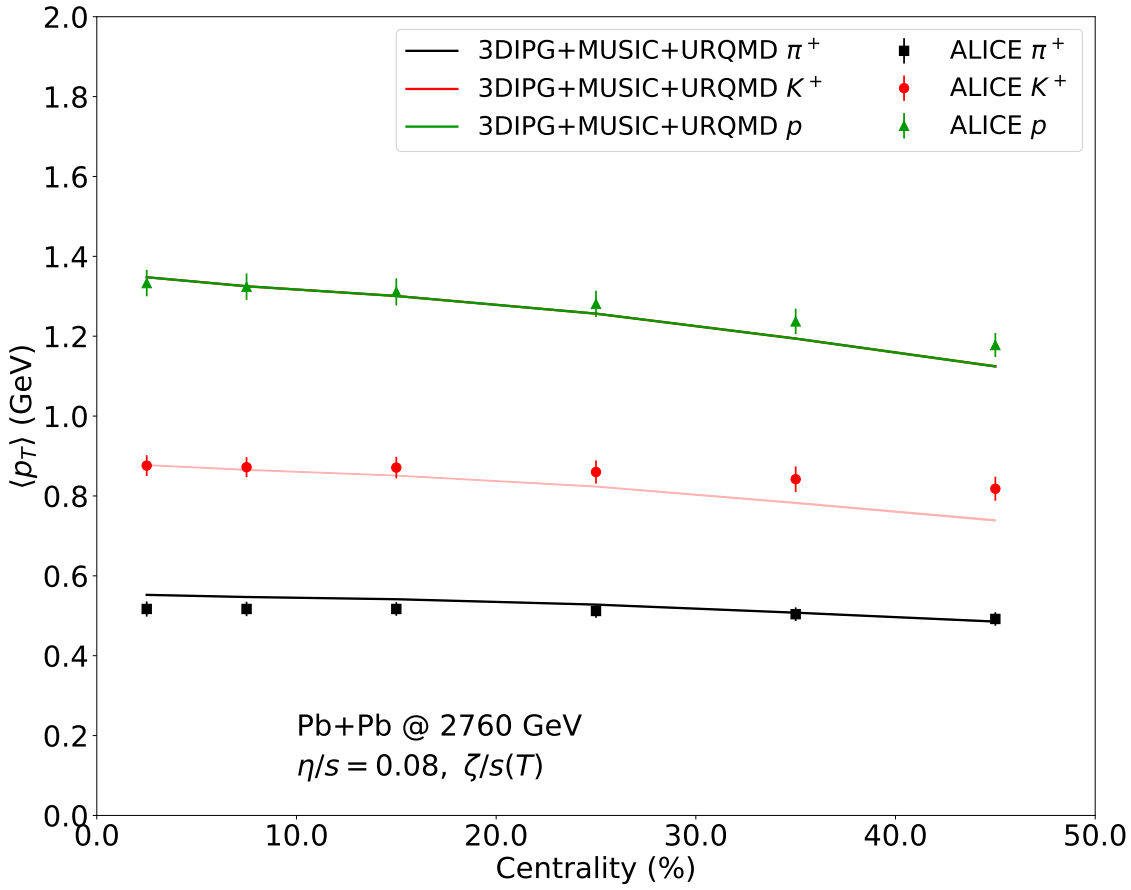

Figure 6.7: Identified particle $\langle p_T \rangle$ for protons, kaons, and pions, compared to ALICE data, [97].

this particular cell cools and turns back into hadrons, the collective flow is shared by all the particles within the cell, and thus particles with larger mass, given the same flow velocity, end up with larger momentum. The inclusion of bulk viscosity dampens the radial expansion and improves agreement with $\langle p_T \rangle$ data for protons.

Fig. (6.6) shows the spectrum for these same three hadronic species in the 0-5% and 30-40% centrality classes. The 0-5% centrality class agrees quite well, while the 30-40% bin deviates from the experimental data for $p_T > 1.5\,\text{GeV}$, where mini-jets, physics that is not included in this calculation, are expected to become more important.

6.4 Longitudinal Observables

The 2+1D formulation of IP-Glasma had no longitudinal structure, meaning that it was only able to explore transverse physics. A prime motivation for the 3+1D formulation is to explore the longitudinal dynamics of heavy ion collisions and to understand to what degree the rapidity fluctuations introduced by the JIMWLK evolution are able to describe the rapidity fluctuations that are measured experimentally in the final state particle spectra.

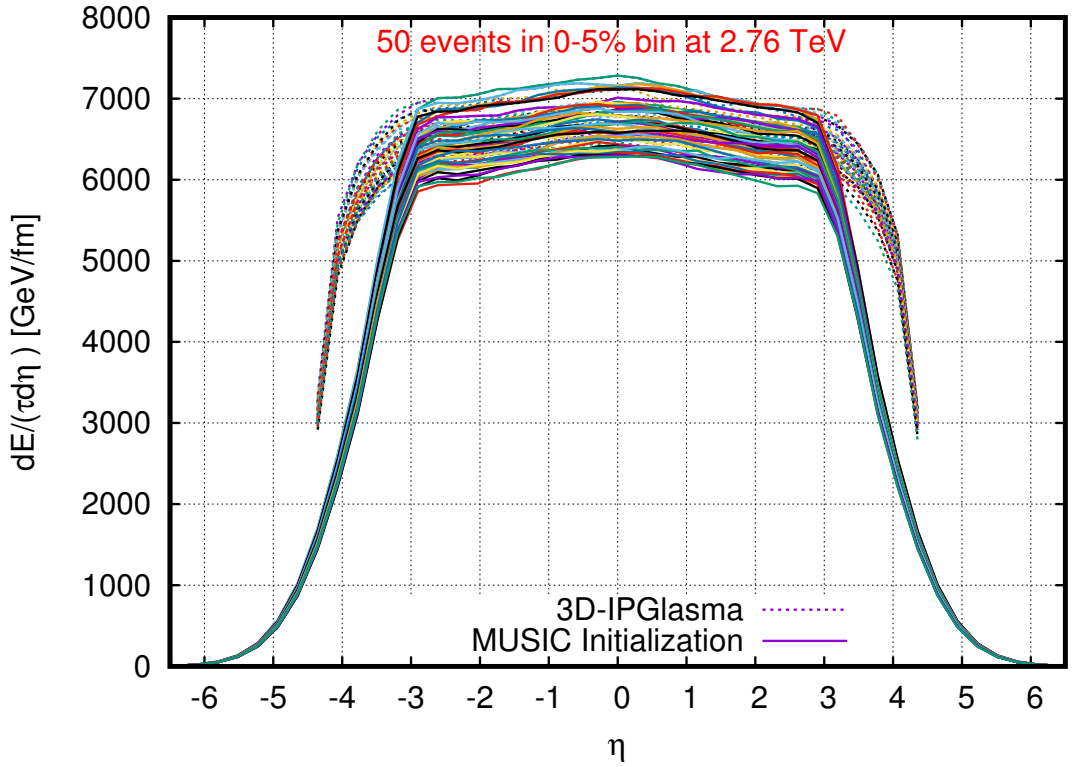

Figure 6.8: The rapidity profile of the energy density at the end of the IP-Glasma evolution for 50 events, and the corresponding profiles used to initialize MUSIC. The horizontal axis is spacetime rapidity.

Because the JIMWLK evolution is not able to begin at arbitrarily high rapidities, the initial profiles generated by the 3+1D IP-Glasma are only in the range of $-4 < \eta < 4$. When matching to the hydrodynamic evolution outside of these values, it is important numerically to take the energy density gradually to zero in order to avoid sharp gradients in the η-direction or boundary effects if the medium extends all the way to the boundary. Ad-

ditionally, in order to find agreement with the longitudinal structure of hadron multiplicity measurements, we modify the rapidity profile for $|\eta| > 2.5$. We implement the following profile

$$T^{\mu\nu}_{\text{hydro}}(\mathbf{x}_\perp, \eta, \tau_0) = T^{\mu\nu}_{\text{IP-Glasma}}(\mathbf{x}_\perp, \eta, \tau_0) \exp\left[-\theta\left(|\eta| - 2.5|\right) \frac{(|\eta| - 2.5)^2}{2}\right] \tag{6.9}$$

which leaves the stress energy unchanged in the range $|\eta| < 2.5$ and takes it gradually to zero as a half gaussian outside of this region. The result can be seen in Fig. (6.8). From this figure, one can see that the unmodified 3D IP-Glasma profile would both lead to numerical problems, and that it would not adequately describe the "shoulders" of the rapidity profile shown in Fig. (6.9).

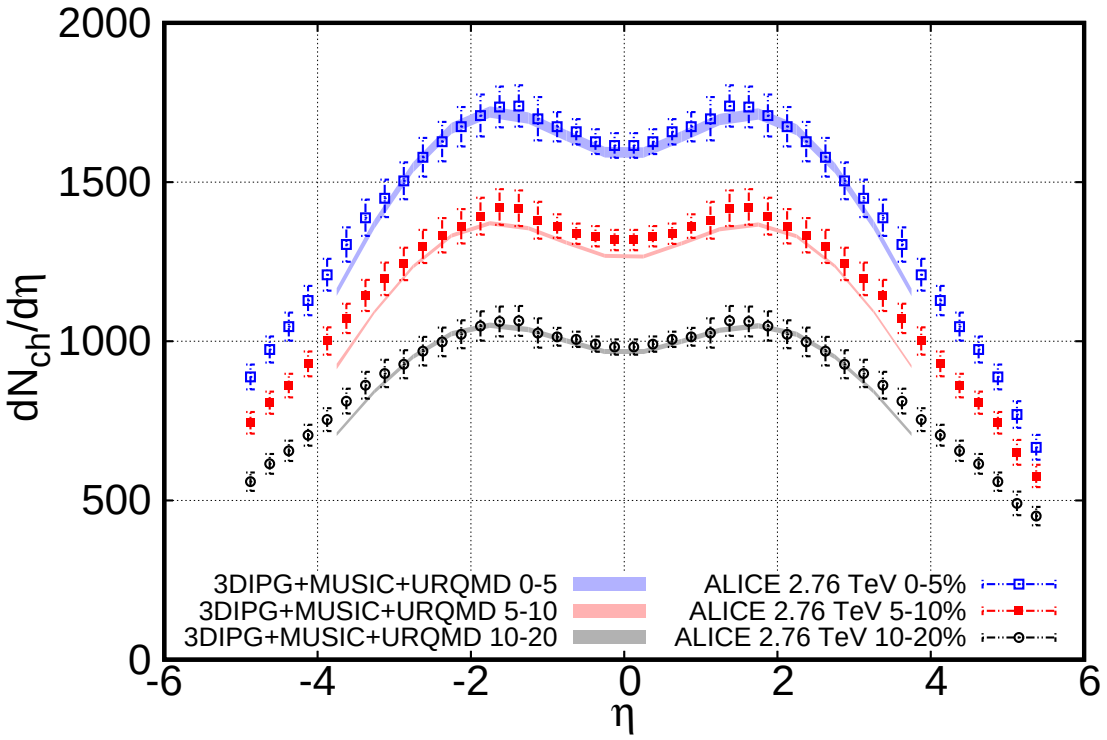

Figure 6.9: Charged hadron multiplicity vs pseudorapidity, as compared to ALICE data [98].

In Figs. (6.10) and (6.11), the rapidity dependence of the flow harmonics $v_n(\eta)$ are plotted. The kinematic cuts are made to match those of the experimental data. For CMS, the reference flow is computed using only particles in the range $|\eta| < 2.4$, and the p_T integration

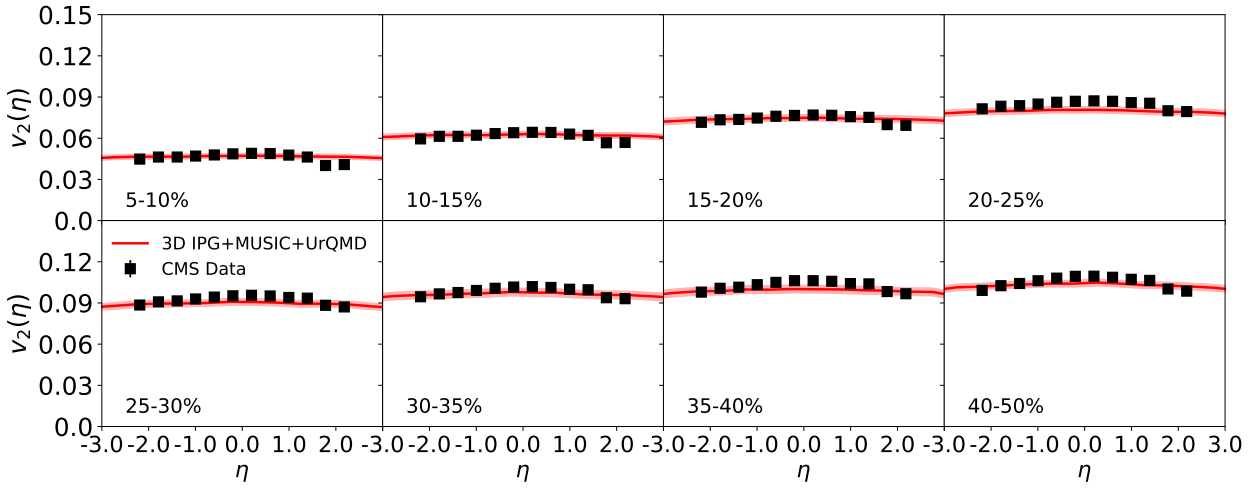

Figure 6.10: The rapidity dependence of $v_2(\eta)$ as compared to CMS data. Both data and calculation integrate over $0.3 < p_T < 3.0\,\text{GeV}$ and use reference particles in the range $|\eta| < 2.4$. Data from [26]

is for $0.3 < p_T < 3.0\,\text{GeV}$. ALICE, on the other hand, uses reference flow computed at mid-rapidity and integrates all particles, $p_T > 0$. For the theoretical calculation, the range is limited to $0 < p_T < 3.0\,\text{GeV}$ because hydrodynamic applicability becomes questionable above 3.0 GeV. Comparing the two figures, one sees a must stronger peak in the $v_n(\eta)$ curve for ALICE. This is due to the reference flow being from mid-rapidity. One can think of $v_n\{2\}$ as correlating two different flow vectors, and the maximum correlation comes from self-correlation, i.e. mid-rapidity with mid-rapidity. This peak does not show up as prominently for the CMS data because the reference flow is taken over a much larger rapidity range. Of course, in the limit of a boost invariant system, this distinction would disappear, because all rapidity slices would produce the same flow vectors. Thus, the superior agreement of the theoretical result with the rapidity dependence of the CMS data is an indication that the model is likely more correlated in rapidity than the experimental results.

It is interesting to explore the comparison of rapidity correlation in the initial state anisotropies to the final state flow correlations after hydrodynamic evolution. The final

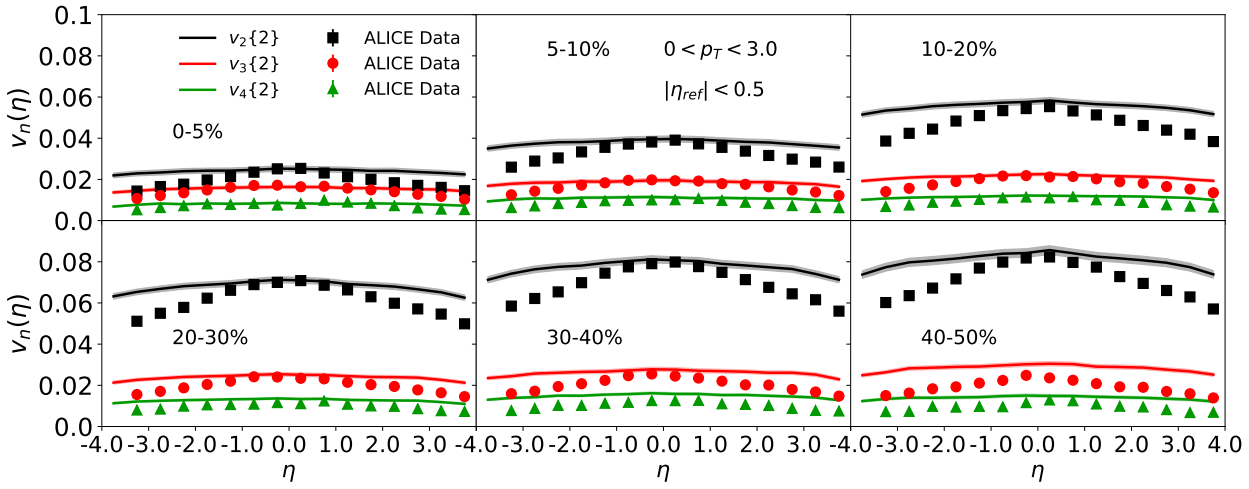

Figure 6.11: The rapidity dependence of $v_n(\eta)$ $(n = 2, 3, 4)$ as compared to ALICE data. Both data and calculation integrate over $p_T > 0\,\text{GeV}$ and use reference particles in the range $|\eta| < 0.5$. Data from [99].

state quantity is given in terms of flow coefficients,

$$r_n(\eta_a, \eta_b) = \frac{\langle v_n(-\eta_a) v_n(\eta_b) \cos(n(\phi_n(-\eta_a) - \phi(\eta_b))\rangle}{\langle v_n(\eta_a) v_n(\eta_b) \cos(n(\phi_n(\eta_a) - \phi(\eta_b))\rangle} \tag{6.10}$$

where η is the pseudo-rapidity. This should not be confused with that using initial state energy anisotropies,

$$\tilde{r}_n(\eta_s^a, \eta_s^b) = \frac{\langle \epsilon_n(-\eta_s^a) \epsilon_n(\eta_s^b) \cos(n(\psi_n(-\eta_s^a) - \psi(\eta_s^b))\rangle}{\langle \epsilon_n(\eta_s^a) \epsilon_n(\eta_s^b) \cos(n(\psi_n(\eta_s^a) - \psi(\eta_s^b))\rangle} \tag{6.11}$$

where η_s is the spacetime rapidity and ϵ_n is the n^{th} order initial state energy anisotropy. In both cases η_b is a reference, taken to be $\eta_b = 3.5$. When computing ϵ_n, it is typical to define r such that $r = 0$ at the center of energy density in the transverse plane. In order to compute $\tilde{r}_n(\eta_a, \eta_b)$, we define r as the transverse distance from the center of energy of at mid-rapidity $(\eta = 0)$. This defines an axis parallel to the beam axis and a common reference from which to measure the spatial energy anisotropies $\epsilon_n(\eta)$ for all η.

The flow factorization breaking ratios r_n quantify the ratio of the correlation between a reference η_b and a rapidity slice $-\eta_a$ on the opposite side of mid-rapidity, and one on the same side, η_a. It is clear that r_n depends on the magnitude as well as the angular correlation

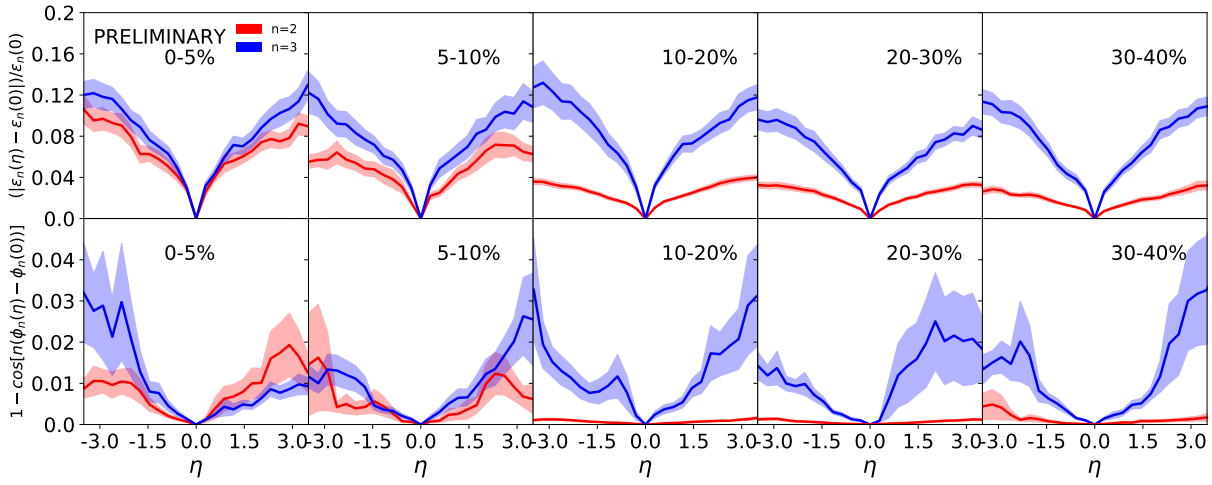

Figure 6.12: The top row shows the magnitude of the deviation of $|\epsilon_n|$ from the value at mid-rapidity, in ratio to the value at mid-rapidity. The bottom row quantifies that angular deviation from mid-rapidity.

of the ϵ_n vectors. To give an idea on how the magnitude of $|\epsilon_n|$ as well as the angle Φ_n vary over a rapidity range, they are both compared to the mid-rapidity value in Fig. (6.12). For central collisions, $\epsilon_2(\eta_s)$ and $\epsilon_3(\eta_s)$ are both fluctuation driven, and the variation in these quantities in rapidity, both magnitude and angle, are comparable. As one moves to more peripheral collisions, $\epsilon_3(\eta_s)$ continues to be fluctuation driven, and the variation in $\epsilon_3(\eta_s)$ does not change much over centralities. At these centralities ϵ_2 becomes driven primarily by the impact parameter, and the fluctuations become less important. This is evident particularly for the angular variation shown in Fig. (6.12), where $\Phi_2(\eta_s)$ and $\epsilon_2(\eta_s)$ deviate less and less from the value at mid-rapidity as the impact parameter becomes the defining feature of the geometry.

In Fig. (6.13), it is apparent that the decorrelation, meaning deviation below unity, in the initial state as quantified by $\tilde{r}_n(\eta_s^a, \eta_s^b)$, is smaller than that of the final state observable $r_n(\eta_a.\eta_b)$. For one thing, $\tilde{r}_n$ is computed using ϵ_n which only takes into account the energy density of the initial state, but not the flow. In fact, it ignores all components of $T^{\mu\nu}$ except for the energy density, while hydrodynamics evolves the full stress-energy tensor. This could certainly account for some of the difference. Furthermore, the modification of the rapidity

h

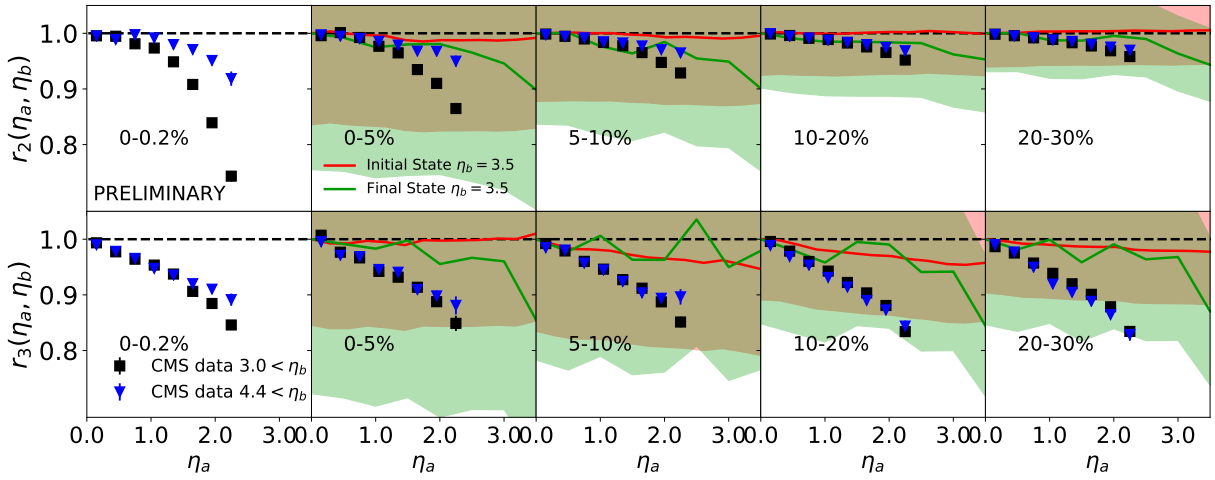

Figure 6.13: Flow factorization breaking ratios, as a function of rapidity. Data taken from [27]

profile according to Eq. (6.9) to agree with the multiplicity distribution will lead to some additional decorrelation due the reduction in the energy density, and thus the lifetime of the QGP for rapidities outside of $|\eta| < 2.5$. The reduction in lifetime will give less time for the hydrodynamic evolution to build up the momentum anisotropy and thus reduce v_n. Additionally, the sampling of particles and the hadron gas evolution can decorrelate things further. Finally, as noted, the initial state quantity, $\tilde{r}_n(\eta_s^a, \eta_s^b)$, is defined as a function of space-time rapidity, whereas $r_n(\eta_a, \eta_b)$ is defined as a function of pseudo-rapidity, making their comparison a bit more subtle than it may seem at first. Ultimately, the emphasis should be placed on the the final state r_n, which allows for direct comparison to experimental data.

In comparing to data, the decorrelation in the model calculation is clearly less than that measured in experiment. There are, however, other potential sources of decorrelation, that have been neglected here. Thermal fluctuations in the hydrodynamic evolution, and mini-jets are other potential sources of decorrelation that are not included in this or virtually any other similar calculations. Hydrodynamic fluctuations are known to exist in viscous hydrodynamics due to the fluctuation-dissipation theorem, and could in principle lead to decorrelation in the rapidity direction, although whether these fluctuations could substantially affect an

observable such as $r_n(\eta_a, \eta_b)$ would seem to depend on the length scales affected by the fluctuations. Mini-jets, or hard scatterings with energy greater than the temperature scale but less than say, 10 GeV, are also known to be present in heavy ion collisions and highly abundant. They can contribute significantly to the overall energy of the system, and do not provide long range flow correlations like those arising from hydrodynamic flow. For this reason, it is reasonable to believe that mini-jets, if included concurrently with hydrodynamic evolution could provide significant decorrelation between rapidity slices. Until the decorrelation introduced by these other sources, that are known to exist in heavy ion collisions, are studied in state-of-the-art simulations, it is hard to draw clear conclusions on whether the fluctuations arising from the JIMWLK evolution provide sufficient decorrelation to agree with data, or if there is additional unknown physics that needs to be included.

It is worth noting however that the implementation of this model, such as the parameters implemented in the running coupling constant, or the prescription for how it runs, could be fine tuned to improve agreement with data for $r_n(\eta_a, \eta_b)$. Fine-tuning of parameters to find agreement with this particular observable has not been done, and is considered future work.

7

Conclusion

Asymptotic freedom means that it is not possible to study free quarks and gluons, at least under normal laboratory conditions. Heavy ion collisions provide the ability to create a deconfined state of quarks and gluons, known as Quark Gluon Plasma, in the laboratory at extreme temperatures and pressures. The fundamental theory that could describe such dynamics is high temperature many-body QCD. While high temperature QCD, and its numerical counterpart Lattice QCD, are incredibly important and active fields, it is not feasible to adequately describe the full complexity of heavy ion collisions from these perspectives. Instead, a number of effective theories are employed, typically using Monte-Carlo techniques, to simulate the physics of heavy ion collisions. It is then possible to compare the particle spectra produced using these simulations with those measured at experimental detectors, in order to deduce properties of heavy ion collisions including the conditions for and evolution of Quark Gluon Plasma.

In only $\sim 10\,\mathrm{fm/c}$ these collisions evolve through at least three distinct phases, each of which is typically modelled by its own effective theory: an initial state that is governed by strong classical gluon fields, a relativistic viscous hydrodynamic phase, and a hadronic gas phase. This is sometimes referred to as the "standard model of heavy ion collisions," and describes the phenomenological approach taken in this thesis.

At the energies explored in most heavy ion collision experiments, particularly those at the Large Hadron Collider, there is an approximate symmetry in the direction that coincides with beam axis, known as boost invariance, that can be used to simplify the dynamics of heavy ion collisions to two spatial and one temporal dimension. While the assumption of boost invariance has long been useful in simplifying the dynamics of heavy ion collisions to

2+1D, it limits the study of heavy ion collisions to their transverse dynamics. By extending the phenomenologically successful IP-Glasma from its original boost-invariant formulation to 3+1D dimensions, it is possible to study the full 3+1D dynamics of heavy ion collisions.

In particular, the JIMWLK renormalization group equations allow for a rapidity dependent source term in the CGC Lagrangian that leads to longitudinal fluctuations that break boost invariance. Experimental data clearly indicates that heavy ion collisions are not strictly boost invariant and that longitudinal fluctuations can be quantified in observables such as the $r_n(\eta_a, \eta_b)$ flow factorization breaking ratios.

In order to evolve non-boost invariant gauge fields on a 3+1D lattice, it is necessary to adapt the CGC initial condition. Firstly, the initial gauge fields are made to be pure gauge outside of the source terms in all three spatial dimensions in order to avoid energy deposition outside of the interaction region between the nuclei. The gauge fields are still sourced by δ-function color sources that remain on the light-cone. Additionally, Gauss' law is no longer trivially satisfied and must be solved iteratively, the procedure and ansatz for which are novel to this thesis and outlined in section 4.6.

These alterations dramatically modify the evolution of the chromo-magnetic and chromo-electric fields as well as the pressure. Whereas in 2+1D, the initial chromo-electric and chromo-magnetic fields are purely longitudinal, in 3+1D the initial energy density is actually dominated by the transverse fields. As argued in section 4.7, this feature of the 3+1D calculation challenge the 2+1D understanding of purely longitudinal initial fields as flux tubes that lead to negative longitudinal pressure. In fact, the formulation presented in this thesis seems to suggest that the 2+1D picture will not be recovered in the infinite moment limit.

Evolving the system in 3+1D dimensions means that it can be matched to 3+1D hydrodynamics, and is thus phenomenologically applicable. Fully 3+1D simulations using 3+1D IP-Glasma+MUSIC+UrQMD, were run for the first time and the phenomenological consequences of the rapidity fluctuations from the initial state JIMWLK evolution were studied on hadronic observables.

The phenomenological results of the 3+1D IP-Glasma are able to describe mid-rapidity

observables, although with slightly different parameters than those typically used in the boost invariant case. Longitudinal observables such as multiplicity and elliptic flow are well described, although they show only a slight rapidity dependence over a large range of rapidities. Decorrelation of different rapidities are quantified by the $r_n(\eta_a, \eta_b)$ flow factorization breaking ratio. The model results shown clearly break boost invariance and show the correct trends. The magnitude of the decorrelation is less that of the experimental data, leaving room for other sources of decorrelation such as mini-jets, thermal fluctuations, etc, or possibly for slight modifications to the model, such as the parameters and implementation of the running coupling.

Heavy ion collisions can only be understood completely through their full 3+1D dynamics. The 3+1D IP-Glasma initial condition, coupled to 3+1D hydrodynamic and hadron gas evolutions, gives a 3+1D dimensional understanding of the formation and evolution of Quark Gluon Plasma (QGP) in heavy ion collisions. This thesis moves closer to fully 3+1D simulations of the heavy ion collisions and, with it, a more complete understanding.

8

Numerical Details

8.1 Poisson Equation

In this section, we will outline the numerical details of how the Poisson equation is solved, as done in chapter 19 of Numerical Recipes for C [100]. This will provide a good starting place from which to discuss the numerical solution to the JIMWLK evolution equation discussed in section 4.3. The Poisson equation is

$$\nabla^2 A = \rho \tag{8.1}$$

This can be solved more easily in momentum space. Fourier transforming A,

$$A(\mathbf{x}) = \int \frac{d^2\mathbf{k}}{(2\pi)^2} A(\mathbf{k}) e^{i\mathbf{k}\cdot\mathbf{x}} \tag{8.2}$$

and applying the derivatives gives,

$$\nabla^2 A(\mathbf{x}) = \int \frac{d^2\mathbf{k}}{(2\pi)^2} A(\mathbf{k}) \nabla^2 e^{i\mathbf{k}\cdot\mathbf{x}} = \int \frac{d^2\mathbf{x}}{(2\pi)^2} (-k^2) A(\mathbf{k}) e^{i\mathbf{k}\cdot\mathbf{x}}. \tag{8.3}$$

Comparing this to the Fourier transform of ρ,

$$\rho(\mathbf{x}) = \int \frac{d^2\mathbf{k}}{(2\pi)^2} \rho(\mathbf{k}) e^{i\mathbf{k}\cdot\mathbf{x}} \tag{8.4}$$

it is plain to see that $-k^2 A(\mathbf{x}) = \rho(\mathbf{x})$. In this section, we will outline a discretized solution to this equation, first by discretizing the Poisson equation,

$$\begin{aligned} \nabla^2 A &= \left(\frac{\partial^2}{\partial x^2} + \frac{\partial^2}{\partial y^2}\right) A = \rho \\ &= \frac{1}{{\Delta_x}^2}(A_{j+1,l} - A_{j,l} - A_{j,l} + A_{j-1,l} + A_{j,l+1} - A_{j,l} - A_{j,l} + A_{j,l-1}) = \rho_{j,l} \\ &= \frac{1}{{\Delta_x}^2}(A_{j+1,l} - 4A_{j,l} + A_{j-1,l} + A_{j,l+1} - A_{j,l-1}) = \rho_{j,l} \end{aligned} \tag{8.5}$$

where Δ_x is the transverse grid size, or discretization resolution. Fourier transforming the field and the charge density,

$$A_{j,l} = \frac{1}{JL}\sum_{m=0}^{J-1}\sum_{n=0}^{L-1}\tilde{A}_{m,n}e^{-2\pi ijm/J}e^{-2\pi iln/L} \tag{8.6}$$

$$\rho_{j,l} = \frac{1}{JL}\sum_{m=0}^{J-1}\sum_{n=0}^{L-1}\tilde{\rho}_{m,n}e^{-2\pi ijm/J}e^{-2\pi iln/L} \tag{8.7}$$

Plugging equations 8.6 and 8.7 into 8.5, one gets,

$$\begin{aligned}\frac{1}{{\Delta_x}^2}\Big(&\frac{1}{JL}\sum_{m=0}^{J-1}\sum_{n=0}^{L-1}\tilde{A}_{m,n}e^{-2\pi i(j+1)m/J}e^{-2\pi iln/L} - 4\frac{1}{JL}\sum_{m=0}^{J-1}\sum_{n=0}^{L-1}\tilde{A}_{m,n}e^{-2\pi ijm/J}e^{-2\pi iln/L}\\ &+\frac{1}{JL}\sum_{m=0}^{J-1}\sum_{n=0}^{L-1}\tilde{A}_{m,n}e^{-2\pi i(j-1)m/J}e^{-2\pi iln/L} + \frac{1}{JL}\sum_{m=0}^{J-1}\sum_{n=0}^{L-1}\tilde{A}_{m,n}e^{-2\pi ijm/J}e^{-2\pi i(l+1)n/L}\\ &+\frac{1}{JL}\sum_{m=0}^{J-1}\sum_{n=0}^{L-1}\tilde{A}_{m,n}e^{-2\pi ijm/J}e^{-2\pi i(l-1)n/L}\Big) = \frac{1}{JL}\sum_{m=0}^{J-1}\sum_{n=0}^{L-1}\tilde{\rho}_{m,n}e^{-2\pi ijm/J}e^{-2\pi iln/L}.\end{aligned} \tag{8.8}$$

It is possible to pull out the common terms,

$$\begin{aligned}\frac{1}{{\Delta_x}^2}\Bigg(\frac{1}{JL}\sum_{m=0}^{J-1}\sum_{n=0}^{L-1}\tilde{A}_{m,n}e^{-2\pi ijm/J}e^{-2\pi iln/L}\Big(e^{-2\pi im/J} - 4 + e^{2\pi im/J} + e^{-2\pi in/L} + e^{+2\pi in/L}\Big)\Bigg)\\ = \frac{1}{JL}\sum_{m=0}^{J-1}\sum_{n=0}^{L-1}\tilde{\rho}_{m,n}e^{-2\pi ijm/J}e^{-2\pi iln/L}.\end{aligned} \tag{8.9}$$

Equating coefficients on both sides of equation 8.9,

$$\frac{1}{{\Delta_x}^2}\tilde{A}_{m,n}(e^{-2\pi im/J} - 4 + e^{2\pi im/J} + e^{-2\pi in/L} + e^{+2\pi in/L}) = \tilde{\rho}_{m,n} \tag{8.10}$$

This can be written in terms of cosine functions,

$$\begin{aligned}\tilde{A}_{m,n}(2\cos\frac{2\pi m}{J} + 2\cos\frac{2\pi n}{L} - 4) &= \tilde{\rho}_{m,n}{\Delta_x}^2\\ \tilde{A}_{m,n} &= \frac{\tilde{\rho}_{m,n}{\Delta_x}^2}{2(\cos\frac{2\pi m}{J} + \cos\frac{2\pi n}{L} - 2)}\end{aligned} \tag{8.11}$$

Thus the Poisson equation can be solved by Fourier transforming the charge density $\rho(x)$ into momentum space, constructing the Fourier modes that appear in the denominator of

Eq. (8.12), before finally computing $\tilde{A}_{m,n}$ and inverse Fourier transforming back into position space. In our particular case, an infrared regulator, $m_{\rm reg}$ is used in the solution to the Poisson equation. The regulator models color confinement and cuts off Coulomb tails in the gauge fields. Including this factor, makes the solution,

$$\tilde{A}_{m,n} = \frac{\tilde{\rho}_{m,n}{\Delta_x}^2}{-m_{\rm reg}^2 + 2(\cos\frac{2\pi m}{J} + \cos\frac{2\pi n}{L} - 2)} \tag{8.12}$$

Eq. (8.12) works for periodic boundary conditions. If one wants to impose boundary conditions such that the gauge fields vanishes at the boundary, one can carry out the same analysis as done above for the complex Fourier transform using the sine transform. The result is,

$$\begin{aligned} \tilde{A}_{m,n}(2\cos\frac{2\pi m}{J} + 2\cos\frac{2\pi n}{L} - 4) &= \rho_{m,n}{\Delta_x}^2 \\ \tilde{A}_{m,n} &= \frac{\tilde{\rho}_{m,n}{\Delta_x}^2}{2(\cos\frac{\pi m}{J} + \cos\frac{\pi n}{L} - 2)} \end{aligned} \tag{8.13}$$

In this thesis, we employ the periodic boundary condition (8.12) for the solution to the JIMWLK equation and (8.13) for the solution to the Poisson equation in solving for the initial gauge fields.

8.2 JIMWLK in Momentum Space

This previous discussion, based on the numerical solution to the Poisson equation in [100] is useful because it lays the foundation for how we solve the JIMWLK equation numerically. For the JIMWLK equation, what we actually want to compute is

$$\nabla^2\beta = 2\pi\nabla\cdot\xi \tag{8.14}$$

because, in momentum space, this gives the Fourier transform of the JIMWLK kernel dotted with the noise term ξ,

$$-k^2\beta = 2i\pi\mathbf{k}\cdot\xi \tag{8.15}$$

so

$$\beta = \frac{-2\pi i\mathbf{k}\cdot\xi}{k^2} = -2\pi i\frac{k_x\xi_x + k_y\xi_y}{k^2} \tag{8.16}$$

Following a similar procedure as the previous section, we find a result similar to Eq. (8.9), except we need to discretize the divergence of the source term on the right hand side,

$$\frac{1}{{\Delta_x}^2}\left(\frac{1}{JL}\sum_{m=0}^{J-1}\sum_{n=0}^{L-1}\tilde{\beta}_{m,n}e^{-2\pi ijm/J}e^{-2\pi iln/L}\left(e^{-2\pi im/J}-4+e^{2\pi im/J}+e^{-2\pi in/L}+e^{+2\pi in/L}\right)\right)$$
$$=2\pi\frac{1}{2\Delta_x}\frac{1}{JL}\sum_{m=0}^{J-1}\sum_{n=0}^{L-1}\tilde{\xi}^x_{m,n}e^{-2\pi ijm/J}e^{-2\pi iln/L}(e^{-2\pi im/J}-e^{+2\pi im/J})$$
$$+\tilde{\xi}^y_{m,n}e^{-2\pi ijm/J}e^{-2\pi iln/L}(e^{-2\pi in/L}-e^{+2\pi in/L}) \tag{8.17}$$

where the term $\frac{1}{2\Delta_x}$ is because the derivative on the right hand side is taken using a central difference derivative (over 2 cells). This becomes,

$$\tilde{\beta}_{m,n}=\frac{-2\pi i(\sin\frac{2\pi m}{J}\tilde{\xi}^x_{m,n}+\sin\frac{2\pi n}{L}\tilde{\xi}^y_{m,n})\Delta_x}{-m^2_{\text{reg}}+2(\cos\frac{2\pi m}{J}+\cos\frac{2\pi n}{L}-2)} \tag{8.18}$$

8.3 Lattice Gauge Theory

Conisder a complex valued Dirac field, $\psi(x)$, that is invariant under local gauge transformation of the form [53],

$$\psi(x)\to e^{i\alpha(x)}\psi(x) \tag{8.19}$$

where $\alpha(x)$ is a phase rotation. This phase rotation can vary locally, which means that in order to take derivatives that are gauge invariant, it is necessary to define a covariant derivative that takes this possible variation into account. Looking at the derivative of the field $\psi(x)$,

$$n^\mu\partial_\mu\psi=\lim_{\epsilon\to0}\frac{1}{\epsilon}[\psi(x+\epsilon n)-\psi(x)] \tag{8.20}$$

the terms $\psi(x+\epsilon n)$ and $\psi(x)$ have different transformations under Eq. (8.19), meaning that in order to take their difference in a gauge invariant way that makes sense, it is necessary to introduce the gauge link, or connection, which has the transformation property

$$U(y,x)\to e^{i\alpha(y)}U(y,x)e^{-i\alpha(x)} \tag{8.21}$$

where $U(x,x)=1$. This makes it so that $\psi(y)$ and $U(y,x)\phi(x)$ transform the same way under gauge transformations. This can be used to define the covariant derivative,

$$n^\mu D_\mu\psi=\lim_{\epsilon\to0}\frac{1}{\epsilon}[\psi(x+\epsilon n)-U(x+\epsilon n,x)\psi(x)] \tag{8.22}$$

Here, both of the terms on the right hand side transform the same way, so that it is possible to take the difference in a meaningful way.

In QCD, the gauge link is

$$U_\mu(x) = \mathcal{P}\exp\left(ig\int_0^1 ds \frac{dx^\mu}{ds} A^a_\mu(x(s))t^a\right) \approx \exp\{igaA^a_\mu(x)t^a\} \tag{8.23}$$

which can be expanded for small lattice spacing, a, as

$$U_\mu = 1 + igaA^a_\mu t^a - \frac{1}{2}g^2a^2A^a_\mu A^b_\mu t^a t^b + O(a^3) \tag{8.24}$$

With this definition, it is possible to build plaquettes, which are a string of consecutive gauge links that form a closed loop,

$$U_{xy} = U_x(x + a_x/2)U_y(x + a_x + a_y/2)U^\dagger_x(x + a_x/2 + a_y)U^\dagger_y(x + a_y/2) \tag{8.25}$$

To linear order in the lattice spacing this becomes (dropping color indices),

$$\begin{aligned} U^{(1)}_{xy} &\approx 1 + ig\{a_xA_x(x + a_x/2) + a_yA_y(x + a_x + a_y/2) - a_xA_x(x + a_x/2 + a_y) - a_yA_y(x + a_y/2)\} \\ U^{(1)}_{xy} &\approx 1 + igaa_y\{\partial_xA_y - \partial_yA_x\} \end{aligned} \tag{8.26}$$

Going to second order in the lattice spacing, one gets the non-abelian term of the field strength.

$$U^{(2)}_{xy} \approx 1 + iga^2(\partial_xA_y - \partial_xA_y) - g^2a^2[A_x, A_y] = 1 + iga^2F^a_{xy}t^a \approx \exp\{+iga^2F_{xy}\}. \tag{8.27}$$

This is the plaquette. Its conjugate is found by traversing the square in the reverse direction,

$$U^\dagger_{\mu\nu} \approx 1 - iga^2F^a_{\mu\nu}t^a + \frac{g^2}{2}a^4F^a_{\mu\nu}F^b_{\mu\nu}t^at^b + ... \approx \exp\{-iga^2F_{\mu\nu}\}. \tag{8.28}$$

Taking the trace gives us a gauge invariant way of computing the field strength on the lattice. We can take different combinations of plaquettes in order to compute quantities that are relevant for the action or stress-energy tensor, to varying orders of the lattice spacing. For example, to compute the field strength tensor squared, a quantity that will appear in the energy-momentum tensor, we can take

$$\mathrm{Tr}[4 - 2U_{\mu\nu} - 2U^\dagger_{\mu\nu}] = g^2a^4F^a_{\mu\nu}F^a_{\mu\nu} + O(a^6) \tag{8.29}$$

(we have used $\mathrm{Tr}[t^a t^b] = \frac{1}{2}\delta^{ab}$).

In order to improve numerical accuracy, the quantities that are used to do the computations are as follows,

$$DU_i = U_i - 1 = \exp\left(iga_\perp A_i^a t^a\right) - 1 \approx iga_\perp A_i^a t^a - g^2 a_\perp^2 A_i^a t^a A_i^b t^b + \ldots \tag{8.30}$$

and similarly, the plaquette

$$DU_{ij} = U_{ij} - 1. \tag{8.31}$$

8.4 Construction on the Lattice

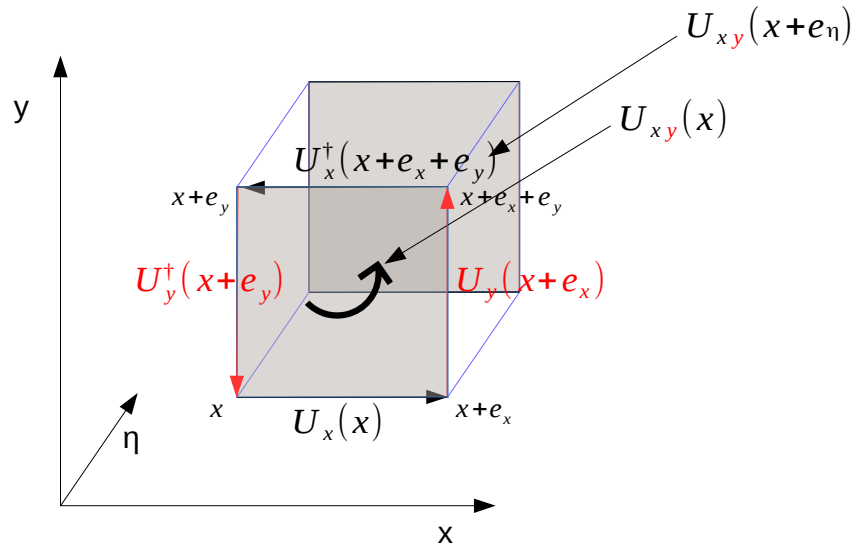

$$U_{xy}(x) = U_x(x)\,U_y(x+e_x)\,U_x^\dagger(x+e_x+e_y)\,U_y^\dagger(x+e_y)$$
$$\widetilde{F}_{xy}^2(x_{cell}) = -4\,\Re\left[Tr\left(U_{xy}(x)-1\right)+Tr\left(U_{xy}(x+e_\eta)-1\right)\right]/2$$

Figure 8.1: The greyed faces of the cell represent the faces whose normal vectors are parallel or anti-parallel to the η-direction. The plaquettes that traverse the boundary of the grey faces construct the plaquette, U_{xy} which is used to construct field strength components, F_{xy}.

The gauge links connect vertices and thus the gauge fields "live" on these links, along with the electric fields. This can be seen in Fig. (8.2). The plaquettes, which construct the magnetic fields, "live" in the center of a face of a cube of gauge links, as shown in Fig.

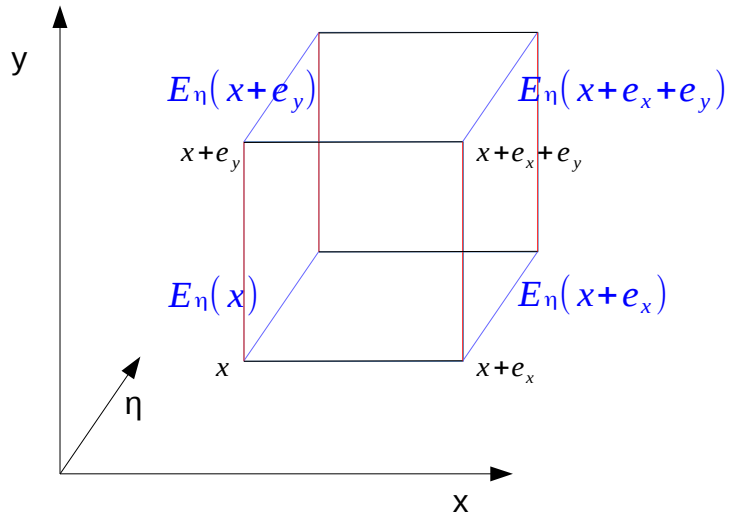

$$E^2_\eta(x_{cell}) = \frac{1}{4}\left[E^2_\eta(x) + E^2_\eta(x+e_x) + E^2_\eta(x+e_y) + E^2_\eta(x+e_x+e_y)\right]$$

Figure 8.2: A diagram of one lattice cell, and the 12 links that border it. Of those 12 links, the four in the η direction contribute to the the electric field in the η direction. To compute E^2_η for this cell, one must average the contribution from these four links. The same applies to the other components (not shown).

(8.1). The stress-energy tensor, $T^{\mu\nu}$ lives in the center of a cell. In order to construct the components of $T^{\mu\nu}$ in the center of the cell, one much average the electric field component E_i over the four links in the i-direction that border a given cube, or cell. For the magnetic field, there are two faces of the cube that correspond to a given magnetic field component. This is because, for a given cell there are two plaquettes whose normal vector point in the i-direction, and thus this component of the field strength F_{jk} would be constructed by averaging the two plaquettes associated with these faces. For example, the x component of the magnetic fields is the average of the two plaquettes whose faces have a normal vector parallel or anti-parallel to the x-direction.

Bibliography

[1] B. Schenke, P. Tribedy, and R. Venugopalan, "Event-by-event gluon multiplicity, energy density, and eccentricities in ultrarelativistic heavy-ion collisions," *Phys. Rev.*, vol. C86, p. 034908, 2012.

[2] B. Schenke, P. Tribedy, and R. Venugopalan, "Fluctuating Glasma initial conditions and flow in heavy ion collisions," *Phys. Rev. Lett.*, vol. 108, p. 252301, 2012.

[3] T. Lappi and H. Mäntysaari, "On the running coupling in the JIMWLK equation," *Eur. Phys. J.*, vol. C73, no. 2, p. 2307, 2013.

[4] B. Schenke and S. Schlichting, "3D glasma initial state for relativistic heavy ion collisions," *Phys. Rev.*, vol. C94, no. 4, p. 044907, 2016.

[5] B. Schenke, S. Jeon, and C. Gale, "Elliptic and triangular flow in event-by-event (3+1)D viscous hydrodynamics," *Phys. Rev. Lett.*, vol. 106, p. 042301, 2011.

[6] S. A. Bass *et al.*, "Microscopic models for ultrarelativistic heavy ion collisions," *Prog. Part. Nucl. Phys.*, vol. 41, pp. 255–369, 1998. [Prog. Part. Nucl. Phys.41,225(1998)].

[7] M. Gell-Mann, "A Schematic Model of Baryons and Mesons," *Phys. Lett.*, vol. 8, pp. 214–215, 1964.

[8] G. Zweig, "An SU(3) model for strong interaction symmetry and its breaking. Version 2," in *DEVELOPMENTS IN THE QUARK THEORY OF HADRONS. VOL. 1. 1964 - 1978* (D. Lichtenberg and S. P. Rosen, eds.), pp. 22–101, 1964.

[9] J. I. Friedman and H. W. Kendall, "Deep inelastic electron scattering," *Ann. Rev. Nucl. Part. Sci.*, vol. 22, pp. 203–254, 1972.

[10] A. Bodek, D. L. Dubin, J. E. Elias, J. I. Friedman, H. W. Kendall, J. S. Poucher, E. M. Riordan, M. R. Sogard, D. H. Coward, and D. Sherden, "The Ratio of Deep - Inelastic e-n to e-p Cross-Sections in the Threshold Region," *Phys. Lett.*, vol. 51B, pp. 417–420, 1974.

[11] W. A. Bardeen, H. Fritzsch, and M. Gell-Mann, "Light cone current algebra, π^0 decay, and e^+e^- annihilation," in *Topical Meeting on the Outlook for Broken Conformal Symmetry in Elementary Particle Physics Frascati, Italy, May 4-5, 1972*, 1972.

[12] D. J. Gross and F. Wilczek, "Ultraviolet behavior of non-abelian gauge theories," *Phys. Rev. Lett.*, vol. 30, pp. 1343–1346, Jun 1973.

[13] H. D. Politzer, "Reliable perturbative results for strong interactions?," *Phys. Rev. Lett.*, vol. 30, pp. 1346–1349, Jun 1973.

[14] A. Deur, S. J. Brodsky, and G. F. de Teramond, "The QCD Running Coupling," *Prog. Part. Nucl. Phys.*, vol. 90, pp. 1–74, 2016.

[15] S. Bethke, "Experimental tests of asymptotic freedom," *Prog. Part. Nucl. Phys.*, vol. 58, pp. 351–386, 2007.

[16] P. Bicudo, "QCD confinement and chiral crossovers, two critical points?," *PoS*, vol. FACESQCD, p. 015, 2010.

[17] A. Bazavov *et al.*, "Equation of state in (2+1)-flavor QCD," *Phys. Rev.*, vol. D90, p. 094503, 2014.

[18] J. C. Collins and M. J. Perry, "Superdense Matter: Neutrons Or Asymptotically Free Quarks?," *Phys. Rev. Lett.*, vol. 34, p. 1353, 1975.

[19] G. Baym, T. Hatsuda, T. Kojo, P. D. Powell, Y. Song, and T. Takatsuka, "From hadrons to quarks in neutron stars: a review," *Reports on Progress in Physics*, vol. 81, p. 056902, mar 2018.

[20] S. Chatrchyan *et al.*, "Multiplicity and Transverse Momentum Dependence of Two- and Four-Particle Correlations in pPb and PbPb Collisions," *Phys. Lett.*, vol. B724, pp. 213–240, 2013.

[21] S. Voloshin and Y. Zhang, "Flow study in relativistic nuclear collisions by Fourier expansion of Azimuthal particle distributions," *Z. Phys. C*, vol. 70, pp. 665–672, 1996.

[22] A. M. Poskanzer and S. Voloshin, "Methods for analyzing anisotropic flow in relativistic nuclear collisions," *Phys. Rev. C*, vol. 58, pp. 1671–1678, 1998.

[23] B. Alver and G. Roland, "Collision geometry fluctuations and triangular flow in heavy-ion collisions," *Phys. Rev.*, vol. C81, p. 054905, 2010. [Erratum: Phys. Rev.C82,039903(2010)].

[24] P. Romatschke, "Relativistic Fluid Dynamics Far From Local Equilibrium," *Phys. Rev. Lett.*, vol. 120, no. 1, p. 012301, 2018.

[25] S. McDonald, "The initial state of heavy ion collisions in the ip-glasma framework," 2017.

[26] S. Chatrchyan *et al.*, "Measurement of the elliptic anisotropy of charged particles produced in PbPb collisions at $\sqrt{s}_{NN}$=2.76 TeV," *Phys. Rev.*, vol. C87, no. 1, p. 014902, 2013.

[27] V. Khachatryan *et al.*, "Evidence for transverse momentum and pseudorapidity dependent event plane fluctuations in PbPb and pPb collisions," *Phys. Rev.*, vol. C92, no. 3, p. 034911, 2015.

[28] A. Milov, "Particle production and long-range correlations in p+Pb collisions with the ATLAS detector," *Nucl. Phys.*, vol. A932, pp. 357–364, 2014.

[29] A. Kovner, L. D. McLerran, and H. Weigert, "Gluon production from nonAbelian Weizsacker-Williams fields in nucleus-nucleus collisions," *Phys. Rev.*, vol. D52, pp. 6231–6237, 1995.

[30] B. Schenke, S. Jeon, and C. Gale, "(3+1)D hydrodynamic simulation of relativistic heavy-ion collisions," *Phys. Rev.*, vol. C82, p. 014903, 2010.

[31] J. Weil *et al.*, "Particle production and equilibrium properties within a new hadron transport approach for heavy-ion collisions," *Phys. Rev.*, vol. C94, no. 5, p. 054905, 2016.

[32] A. Accardi *et al.*, "Electron Ion Collider: The Next QCD Frontier," *Eur. Phys. J.*, vol. A52, no. 9, p. 268, 2016.

[33] P. Romatschke and R. Venugopalan, "The Unstable Glasma," *Phys. Rev.*, vol. D74, p. 045011, 2006.

[34] T. Epelbaum and F. Gelis, "Pressure isotropization in high energy heavy ion collisions," *Phys. Rev. Lett.*, vol. 111, p. 232301, 2013.

[35] J. I. Kapusta, G. Chen, R. J. Fries, and Y. Li, "Early Time Dynamics of Gluon Fields in High Energy Nuclear Collisions," *Nucl. Phys.*, vol. A956, pp. 553–556, 2016.

[36] D. Gelfand, A. Ipp, and D. Mller, "Simulating collisions of thick nuclei in the color glass condensate framework," *Phys. Rev.*, vol. D94, no. 1, p. 014020, 2016.

[37] C. Shen and B. Schenke, "Dynamical initial state model for relativistic heavy-ion collisions," *Phys. Rev.*, vol. C97, no. 2, p. 024907, 2018.

[38] C. Gale, S. Jeon, and B. Schenke, "Hydrodynamic Modeling of Heavy-Ion Collisions," *Int.J.Mod.Phys.*, vol. A28, p. 1340011, 2013.

[39] H. De Vries, C. W. De Jager, and C. De Vries, "Nuclear charge and magnetization density distribution parameters from elastic electron scattering," *Atom. Data Nucl. Data Tabl.*, vol. 36, pp. 495–536, 1987.

[40] M. L. Miller, K. Reygers, S. J. Sanders, and P. Steinberg, "Glauber modeling in high energy nuclear collisions," *Ann. Rev. Nucl. Part. Sci.*, vol. 57, pp. 205–243, 2007.

[41] K. Aamodt *et al.*, "Higher harmonic anisotropic flow measurements of charged particles in Pb-Pb collisions at $\sqrt{s_{NN}}$=2.76 TeV," *Phys. Rev. Lett.*, vol. 107, p. 032301, 2011.

[42] C. Gale, S. Jeon, B. Schenke, P. Tribedy, and R. Venugopalan, "Event-by-event anisotropic flow in heavy-ion collisions from combined Yang-Mills and viscous fluid dynamics," *Phys.Rev.Lett.*, vol. 110, no. 1, p. 012302, 2013.

[43] W. Zhao, H.-j. Xu, and H. Song, "Collective flow in 2.76 A TeV and 5.02 A TeV Pb+Pb collisions," *Eur. Phys. J.*, vol. C77, no. 9, p. 645, 2017.

[44] H. Kowalski and D. Teaney, "An Impact parameter dipole saturation model," *Phys. Rev.*, vol. D68, p. 114005, 2003.

[45] S. McDonald, C. Shen, F. Fillion-Gourdeau, S. Jeon, and C. Gale, "Hydrodynamic predictions for Pb+Pb collisions at 5.02 TeV," *Phys. Rev.*, vol. C95, no. 6, p. 064913, 2017.

[46] P. Tribedy and R. Venugopalan, "QCD saturation at the LHC: Comparisons of models to p + p and A + A data and predictions for p + Pb collisions," *Phys. Lett.*, vol. B710, pp. 125–133, 2012. [Erratum: Phys. Lett.B718,1154(2013)].

[47] S. McDonald, C. Shen, F. Fillion-Gourdeau, S. Jeon, and C. Gale, "A Detailed Study and Synthesis of Flow Observables in the IP-Glasma+MUSIC+UrQMD Framework," *Nucl. Phys.*, vol. A967, pp. 393–396, 2017.

[48] H. Mntysaari and B. Schenke, "Evidence of strong proton shape fluctuations from incoherent diffraction," *Phys. Rev. Lett.*, vol. 117, no. 5, p. 052301, 2016.

[49] H. Mntysaari, B. Schenke, C. Shen, and P. Tribedy, "Imprints of fluctuating proton shapes on flow in proton-lead collisions at the LHC," *Phys. Lett.*, vol. B772, pp. 681–686, 2017.

[50] B. Schenke, P. Tribedy, and R. Venugopalan, "Initial-state geometry and fluctuations in Au + Au, Cu + Au, and U + U collisions at energies available at the BNL Relativistic Heavy Ion Collider," *Phys. Rev.*, vol. C89, no. 6, p. 064908, 2014.

[51] J. E. Bernhard, J. S. Moreland, S. A. Bass, J. Liu, and U. Heinz, "Applying bayesian parameter estimation to relativistic heavy-ion collisions: Simultaneous characterization of the initial state and quark-gluon plasma medium," *Physical Review C*, vol. 94, Aug 2016.

[52] H. Niemi, K. J. Eskola, and R. Paatelainen, "Event-by-event fluctuations in a perturbative qcd + saturation + hydrodynamics model: Determining qcd matter shear viscosity in ultrarelativistic heavy-ion collisions," *Physical Review C*, vol. 93, Feb 2016.

[53] M. E. Peskin and D. V. Schroeder, *An Introduction to quantum field theory*. Reading, USA: Addison-Wesley, 1995.

[54] A. M. Cooper-Sarkar, "PDF Fits at HERA," *PoS*, vol. EPS-HEP2011, p. 320, 2011.

[55] V. Khachatryan *et al.*, "Transverse-momentum and pseudorapidity distributions of charged hadrons in pp collisions at $\sqrt{s} = 7$ TeV," *Phys. Rev. Lett.*, vol. 105, p. 022002, 2010.

[56] F. Gelis, "Initial state and thermalization in the Color Glass Condensate framework," *Int. J. Mod. Phys.*, vol. E24, no. 10, p. 1530008, 2015.

[57] A. H. Rezaeian, M. Siddikov, M. Van de Klundert, and R. Venugopalan, "Analysis of combined HERA data in the Impact-Parameter dependent Saturation model," *Phys. Rev.*, vol. D87, no. 3, p. 034002, 2013.

[58] G. Altarelli and G. Parisi, "Asymptotic Freedom in Parton Language," *Nucl. Phys.*, vol. B126, pp. 298–318, 1977.

[59] Y. L. Dokshitzer, "Calculation of the Structure Functions for Deep Inelastic Scattering and e+ e- Annihilation by Perturbation Theory in Quantum Chromodynamics.," *Sov. Phys. JETP*, vol. 46, pp. 641–653, 1977. [Zh. Eksp. Teor. Fiz.73,1216(1977)].

[60] V. N. Gribov and L. N. Lipatov, "Deep inelastic e p scattering in perturbation theory," *Sov. J. Nucl. Phys.*, vol. 15, pp. 438–450, 1972. [Yad. Fiz.15,781(1972)].

[61] L. D. McLerran and R. Venugopalan, "Gluon distribution functions for very large nuclei at small transverse momentum," *Phys. Rev.*, vol. D49, pp. 3352–3355, 1994.

[62] F. Gelis and A. Peshier, "Probing colored glass via q anti-q photoproduction," *Nucl. Phys.*, vol. A697, pp. 879–901, 2002.

[63] S. Jeon, "Color Glass Condensate in Schwinger-Keldysh QCD," *Annals Phys.*, vol. 340, pp. 119–170, 2014.

[64] L. D. McLerran and R. Venugopalan, "Computing quark and gluon distribution functions for very large nuclei," *Phys. Rev.*, vol. D49, pp. 2233–2241, 1994.

[65] L. D. McLerran and R. Venugopalan, "Green's functions in the color field of a large nucleus," *Phys. Rev.*, vol. D50, pp. 2225–2233, 1994.

[66] T. Lappi, "Wilson line correlator in the MV model: Relating the glasma to deep inelastic scattering," *Eur. Phys. J.*, vol. C55, pp. 285–292, 2008.

[67] T. Lappi, "Production of gluons in the classical field model for heavy ion collisions," *Phys. Rev.*, vol. C67, p. 054903, 2003.

[68] V. Nanne, "Photon production in the Color Glass Condensate formalism," Master's thesis, McGill University, Montreal, QC Canada, 2009.

[69] S. Jeon and U. Heinz, "Introduction to Hydrodynamics," *Int. J. Mod. Phys.*, vol. E24, no. 10, p. 1530010, 2015.

[70] A. Krasnitz and R. Venugopalan, "Nonperturbative computation of gluon minijet production in nuclear collisions at very high-energies," *Nucl. Phys.*, vol. B557, p. 237, 1999.

[71] L. D. Faddeev and A. A. Slavnov, *Gauge fields: introduction to quantum theory*. Benjamin/Cummings, 1980.

[72] K. Okamoto, Y. Akamatsu, and C. Nonaka, "A new relativistic hydrodynamics code for high-energy heavy-ion collisions," *Eur. Phys. J.*, vol. C76, no. 10, p. 579, 2016.

[73] C.-Y. Wong, *Introduction to High-Energy Heavy-Ion Collisions*. WSPC, sep 1994.

[74] J. Jalilian-Marian, A. Kovner, L. D. McLerran, and H. Weigert, "The Intrinsic glue distribution at very small x," *Phys. Rev.*, vol. D55, pp. 5414–5428, 1997.

[75] F. Gelis, T. Lappi, and R. Venugopalan, "High energy factorization in nucleus-nucleus collisions," *Phys. Rev. D*, vol. 78, p. 054019, 2008.

[76] P. Taels, *Quantum Chromodynamics at small Bjorken-x*. PhD thesis, Antwerp U., 2017.

[77] S. Schlichting and B. Schenke, "The shape of the proton at high energies," *Phys. Lett.*, vol. B739, pp. 313–319, 2014.

[78] K. Rummukainen and H. Weigert, "Universal features of JIMWLK and BK evolution at small x," *Nucl. Phys.*, vol. A739, pp. 183–226, 2004.

[79] T. Lappi, "Gluon spectrum in the glasma from JIMWLK evolution," *Phys. Lett.*, vol. B703, pp. 325–330, 2011.

[80] K. J. Golec-Biernat and M. Wusthoff, "Saturation effects in deep inelastic scattering at low Q**2 and its implications on diffraction," *Phys. Rev.*, vol. D59, p. 014017, 1998.

[81] P. Romatschke and U. Romatschke, *Relativistic Fluid Dynamics In and Out of Equilibrium*. Cambridge Monographs on Mathematical Physics, Cambridge University Press, 2019.

[82] D. N. Blaschke, F. Gieres, M. Reboud, and M. Schweda, "The energymomentum tensor(s) in classical gauge theories," *Nucl. Phys.*, vol. B912, pp. 192–223, 2016.

[83] B. Schenke, C. Shen, and P. Tribedy, "Features of the IP-Glasma," *Nucl. Phys.*, vol. A982, pp. 435–438, 2019.

[84] A. Kurkela, A. Mazeliauskas, J.-F. Paquet, S. Schlichting, and D. Teaney, "Effective kinetic description of event-by-event pre-equilibrium dynamics in high-energy heavy-ion collisions," *Phys. Rev.*, vol. C99, no. 3, p. 034910, 2019.

[85] R. D. Weller and P. Romatschke, "One fluid to rule them all: viscous hydrodynamic description of event-by-event central p+p, p+Pb and Pb+Pb collisions at $\sqrt{s} = 5.02$ TeV," *Phys. Lett.*, vol. B774, pp. 351–356, 2017.

[86] M. P. Heller and M. Spalinski, "Hydrodynamics Beyond the Gradient Expansion: Resurgence and Resummation," *Phys. Rev. Lett.*, vol. 115, no. 7, p. 072501, 2015.

[87] G. S. Denicol, S. Jeon, and C. Gale, "Transport Coefficients of Bulk Viscous Pressure in the 14-moment approximation," *Phys. Rev.*, vol. C90, no. 2, p. 024912, 2014.

[88] F. Cooper and G. Frye, "Comment on the Single Particle Distribution in the Hydrodynamic and Statistical Thermodynamic Models of Multiparticle Production," *Phys. Rev.*, vol. D10, p. 186, 1974.

[89] S. Ryu, J.-F. Paquet, C. Shen, G. Denicol, B. Schenke, S. Jeon, and C. Gale, "Effects of bulk viscosity and hadronic rescattering in heavy ion collisions at energies available at the BNL Relativistic Heavy Ion Collider and at the CERN Large Hadron Collider," *Phys. Rev.*, vol. C97, no. 3, p. 034910, 2018.

[90] P. Romatschke, "New Developments in Relativistic Viscous Hydrodynamics," *Int. J. Mod. Phys.*, vol. E19, pp. 1–53, 2010.

[91] K. Dusling, G. D. Moore, and D. Teaney, "Radiative energy loss and v(2) spectra for viscous hydrodynamics," *Phys. Rev.*, vol. C81, p. 034907, 2010.

[92] P. Bozek, "Bulk and shear viscosities of matter created in relativistic heavy-ion collisions," *Phys. Rev.*, vol. C81, p. 034909, 2010.

[93] J.-F. Paquet, C. Shen, G. S. Denicol, M. Luzum, B. Schenke, S. Jeon, and C. Gale, "Production of photons in relativistic heavy-ion collisions," *Phys. Rev.*, vol. C93, no. 4, p. 044906, 2016.

[94] M. Bleicher *et al.*, "Relativistic hadron hadron collisions in the ultrarelativistic quantum molecular dynamics model," *J. Phys.*, vol. G25, pp. 1859–1896, 1999.

[95] M. Alvioli, H. J. Drescher, and M. Strikman, "A Monte Carlo generator of nucleon configurations in complex nuclei including Nucleon-Nucleon correlations," *Phys. Lett.*, vol. B680, pp. 225–230, 2009.

[96] K. Aamodt *et al.*, "Centrality dependence of the charged-particle multiplicity density at mid-rapidity in Pb-Pb collisions at $\sqrt{s_{NN}} = 2.76$ TeV," *Phys. Rev. Lett.*, vol. 106, p. 032301, 2011.

[97] B. Abelev *et al.*, "Centrality dependence of π, K, p production in Pb-Pb collisions at $\sqrt{s_{NN}} = 2.76$ TeV," *Phys. Rev.*, vol. C88, p. 044910, 2013.

[98] E. Abbas *et al.*, "Centrality dependence of the pseudorapidity density distribution for charged particles in Pb-Pb collisions at $\sqrt{s_{\rm NN}} = 2.76$ TeV," *Phys. Lett.*, vol. B726, pp. 610–622, 2013.

[99] J. Adam *et al.*, "Pseudorapidity dependence of the anisotropic flow of charged particles in Pb-Pb collisions at $\sqrt{s_{\rm NN}} = 2.76$ TeV," *Phys. Lett.*, vol. B762, pp. 376–388, 2016.

[100] W. H. Press, S. A. Teukolsky, W. T. Vetterling, and B. P. Flannery, *Numerical Recipes in C (2Nd Ed.): The Art of Scientific Computing*. New York, NY, USA: Cambridge University Press, 1992.